Proton Dynamics and Water Wires from First-Principles Calculations

Im Fachbereich Physik der Freien Universität Berlin
eingereichte Dissertation von

Gül Bekçioğlu-Neff

Berlin, 2016

Erstgutachter/Betreuer

Prof. Dr. Daniel Sebastiani
MLU Halle-Wittenberg
Institut für Physikalische Chemie
Von-Dankelmann-Platz 4
D-06120 Halle (Saale)

Zweitgutachterin

Prof. Dr. Petra Imhof
FU Berlin
Fachbereich Physik
Arnimallee 14
D-14195 Berlin

Tag der Disputation: November 28, 2016

Die hier vorgestellten Arbeiten wurden in der Arbeitsgruppe von Daniel Sebastiani am Institut für Theoretische Physik an der Freien Universität Berlin angefertigt.

Das Projekt wurde im Rahmen des Forschungsprojekts SE 1008/11-1, von der Deutschen Forschungsgemeinschaft gefördert.

Hiermit versichere ich, die vorliegende Arbeit selbst und ohne weitere Hilfsmittel, außer den angegebenen, angefertigt zu haben. Diese Arbeit wurde nicht schon einmal in einem früheren Promotionsverfahren angenommen oder als ungenügend beurteilt.

Berlin, den _____

Table of contents

1 Introduction

The prospects for understanding structure and dynamics of (aqueous) solutions at a molecular level have increased dramatically with improvements in computational methods.[1–5] In this regard, one of the principal computational techniques is molecular dynamics simulations. The use of molecular dynamics simulations allows for the prediction of the time evolution of a set of interacting atoms by solving the classical equations of motions numerically. The output of these simulations is a set of configurations of the system, which can be tuned to sample a specific statistical mechanics ensemble. The main idea underlying every molecular dynamics simulation is to extract dynamical and structural properties of (multicomponent) systems in the condensed phase directly from the resulting trajectories. Therefore, information about the multicomponent systems *e.g.* solute/solvent interactions can be explored from these computer simulations at atomistic resolution. The ensemble average allows for direct comparison with the experimental measurements under realistic conditions.

One of the key ingredients to carry out atomistic molecular dynamics simulations is the accurate description of the interatomic interactions (potentials) of the atoms composing the system. The classical approach provides empirical potentials with a specific functional form in advance. These empirical potentials are defined with adjustable parameters, which can be obtained from quantum mechanical electronic structure calculations or from experiments. This classical approach is practical for investigating biomolecular systems, which can contain hundreds of thousands to many millions of atoms. In reality, such a treatment of interatomic potentials implies drawbacks for reproducing chemical reactions involving breaking and formation of bonds (*e.g.* proton transfer reactions). The description of chemical reactions requires a sophisticated approach with an explicit consideration of the electronic structure.[6,7] Developments of a variety of new numerical algorithms in the electronic structure theory and overall hardware progresses have enabled for the prediction of previously inaccessible properties of relatively large systems and deduce *e.g.* their spectroscopic properties from quantum mechanical calculations.[8,9] In particular, the use of quantum chemical calculations for all atomic forces acting on the nuclei allows for the automatic incorporation of all relevant interatomic and intermolecular interactions without any atom-specific parameters.[10–14] These quantum mechanical experiments, the so-called *ab initio* molecular dynamics simulations, yield an accurate modeling of the motion of atoms, and the evolution of electronic structure with a time resolution of femtoseconds over a total duration of hundreds of picoseconds. Because of their accuracy in describing electronic interactions, *ab initio* molecular dynamics simulations have been used widely to study dynamics of liquids, proton transfer reactions, and hydrogen bond interactions, which are typically very sensitive to the level of theory.[15–20]

Liquid water is the most common solvent in nature.[21] Due to its strong hydrogen bond network and its large molecular dipole moment, water molecules can stabilize polar reaction intermediates.[22,23] The image below shows a typical hydrogen bonding network between water molecules at room temperature. This complex network undergoes a very fast dynamics, and rearranges itself by breaking and forming hydrogen bonds continuously.[24,25] In liquid water at ambient temperature, the hydrogen bond network has

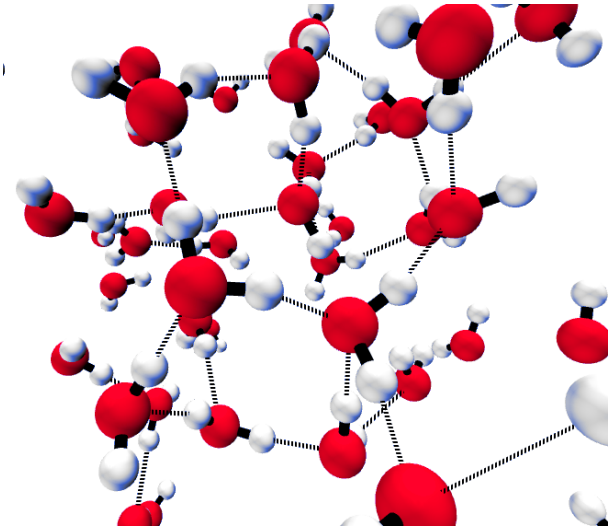

Figure 1: Hydrogen bonding between water molecules.

only a very short lifetime, its autocorrelation function is typically relaxed within a few picoseconds.[26,27] Upon perturbations such that as introduced by ions or even charge redistribution of solute molecules *e.g.* after photoexcitation, the hydrogen bond network responds on a typical timescale of femtoseconds to a few picoseconds, respectively.[28,29] These structural rearrangements of hydrogen bonds are a hallmark of the aqueous solvation, and often determine whether a chemical reaction can occur or not. In fact, hydrogen bonding rearrangements are found to play a crucial functional role in enzymatic reactions by lowering the reaction barrier.[30] Therefore, it is not surprising that the molecular details of aqueous solvation remain an important and very active area of research in the *ab initio* molecular dynamics community.[31–33]

This thesis covers a series of theoretical investigations in the framework of aqueous solvation. Methodologically, *ab initio* molecular dynamics simulations are used to enhance the understanding of dynamical and structural properties of hydrogen bonded systems. In particular, the following questions and challenges are addressed in this thesis:

- the aqueous solvation structure around photosensitive bifunctional chromophores
- the role of solvating water molecules in the proton dissociation mechanisms
- the characterization of kosmotropic and chaotropic effects of divalent ions on the hydrogen bonded network

As a first step, the hydrogen bonding network around a solvated photosensitive probe molecule, a photoacid, is addressed.[34,35] Photoacids undergo a significant enhancement in their acidity after photoexcitation by a pump laser pulse, thus, are utilized as a means of triggering a proton transfer event.[36] These molecules are natural candidates for investigating proton dissociation reactions, and can be used to probe the environments around complex biomolecular systems. The chosen model systems for this

purpose are a specific set of hydroxyquinoline (HQ) derivatives (heteroaromatic fluorescent dyes, see Figure 2). The HQ derivatives are functionalized such that both proton donating (hydroxyl group) and the proton accepting (nitrogen atom) sites are localized at well-defined distances. This functionality allows for the discrimination of different topologies of solvation, for example "short" and "long" water wires between acid/base groups. Water molecules can be aligned as wires, that are essentially relatively stable hydrogen bonded chains, temporarily connecting acid and base sites. Within the lifetime of these water wires, the proton is supposed to propagate concertedly or sequentially from acid to base over large distances.[37,38] These specific hydrogen bond topologies are postulated in a number of studies dealing with proton transport in biological systems, including the proton pump membrane proteins in the framework of signal conversion[39], green fluorescent protein[40], carbonic anhydrase[41], and gramicidin A[42]. Moreover, the time-resolved infrared and fluorescence experiments showed that once an appropriate water wire configuration is formed, the proton transfer is ultrafast *i.e.* in the femtosecond time scale.[37,38] These experimental measurements suggest a correlation between microscopic solvation configurations and spectroscopic parameters. By means of *ab initio* molecular dynamics simulations, the microscopic details of structural and dynamical properties of water wires in relation to the spectroscopic features can be extracted from the trajectories at ambient conditions.

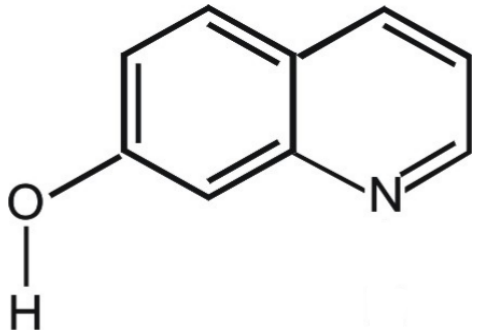

Figure 2: A bifunctional chromophore: 7-Hydroxyquinoline

Additionally, the individual processes in proton dissociation to the solvent can be also studied by use of photoacids.[43] The question of the proton motion in a complex hydrogen bonded network is one of the most fundamental chemical reaction, and of enormous relevance to a wide array of investigations.[39,44] The basic concept of the proton hopping mechanism from one water molecule to a neighbouring water molecule is the so-called von-Grotthuss mechanism.[45,46] Today, the actual proton transfer mechanisms have been discussed to be either concerted or sequential in the bulk solution.[47–49] The concerted mechanism occurs in an assembly of several water molecules linked by hydrogen bonds on a femtosecond time scale. The sequential mechanism is facilitated by rearranging solvation shell water molecules on relatively slower time scales.

A further topic of this thesis is the influence of solvated ions on the (local) structure of liquid water.[50] The functional role of ions is vital, given the numerous aspects that ions have in biomolecular and technological systems. Examples include the aggregation of proteins and nucleic acids, enzyme catalysis, and numerous cellular signaling processes.[51–54] The impact of an ion depends on its charge and size, and is historically quantified by a measure of precipitation and dissolution of egg protein as the so-called Hofmeister effect.[55,56] The underlying ion specific effects are often discussed in terms of stabilization/destabilization of the hydrogen bonding network around an ion. Chaotropic ions are referred to as water structure breakers as they are considered to destabilize

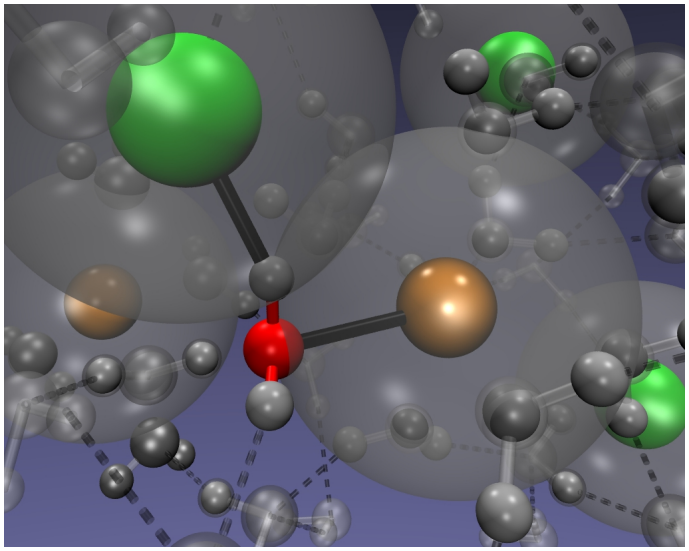

Figure 3: Overlap of the first hydration shells of anions and cations.[50]

the local hydrogen bonded network. On the other hand, kosmotropic ions can interact strongly with water molecules by increasing the stability of the local hydrogen bonded network (water structure maker). The description of the hydration phenomena of the solvated ions is complicated, and requires to include the polarization interactions explicitly. By means of *ab initio* molecular dynamics simulations, the inherently quantum character of these interactions between ions and solvating water molecules can be described without any adjustable parameters. From a computational perspective, it was particularly compelling to study a series of divalent ions in order to characterize to what extent the hydrogen bonding network around ions is modified. A wide array of *ab initio* quantum mechanical calculations has been employed in order to investigate the changes of the (local) structural hydrogen bonding around ions. Such local changes are accessible by ^{1}H NMR chemical shifts measurements.[57,58] A strong relation between ^{1}H NMR chemical shifts and the hydrogen bond length exists, so the trends in chemical shifts can be seen as an indicator for the degree of ordering of the hydrogen bonded network.[59] The availability of the electronic structure allow us to compute the instantaneous ^{1}H NMR chemical shifts from snapshots of the trajectories which are then used to relate the experimental ^{1}H NMR chemical shift spectrum to the underlying solvent structure. Thus, the combination of *ab initio* molecular dynamics simulations with averaged ^{1}H NMR chemical shifts yields a good agreement with experiments in terms of quantifying the kosmotropic/chaotropic nature of ions at a molecular level.

This thesis is organized as follows: in Section 2, a brief discussion of the theoretical background of the methods used in this work is presented. Section 3 gives an overview of the individual studies that are addressed in this thesis, proceeds with a review of the major findings. Finally, Section 4 contains a conclusion of this cumulative dissertation.*

*A full reproduction of the published articles is listed in Appendix B.

2 Theoretical framework

2.1 Introduction to molecular dynamics simulations

Molecular dynamics (MD) simulation is a technique that allows one to predict the time evolution of a system of interacting particles by solving the classical equations of motions numerically.[60,61] As the technique is applicable to a range of various problems, it has become a powerful research tool for studying the structural and dynamical properties of various systems from crystalline and amorphous solids to liquids and solutions, as well as prediction of their spectroscopic properties. There are two main families of MD methods, which can be distinguished by picturing interatomic potentials: classical and *ab initio* approaches. While the classical approach uses the empirical potential energy functions to represent these interatomic interactions, the *ab initio* approach employs a particular electronic structure method to compute the forces acting on the nuclei without atom-specific parameters. It should be noted here that all equations are written in atomic units in this thesis, except where denoted otherwise.

Given the potential energy function of the system, the time evolution is described deterministically by Newton's equations of motions. The trajectory can be obtained by solving Newton's second law

$$\mathbf{F}_I(t) = -\nabla_I V(\mathbf{R}_I(t)) \tag{1}$$

where the equation of motions relate the derivative of the potential energy V to the changes in position $\mathbf{R}$ as a function of time. These equations are normally solved numerically as will be discussed in the following sections.

2.2 Integrating the classical equations of motion

2.2.1 The Verlet algorithm

By far the simplest and most employed integration scheme is the Verlet algorithm[62], which uses positions and accelerations at time t, as well as positions at the previous step $t-\Delta t$, to calculate the new positions at $t+\Delta t$. From a Taylor series expansion up to second order for the position of a particle at time $t+\Delta t$, it follows

$$\begin{aligned}\mathbf{r}_i(t+\Delta t) &\approx \mathbf{r}_i(t) + \Delta t\dot{\mathbf{r}}_i(t) + \frac{1}{2}\Delta t^2\ddot{\mathbf{r}}_i(t) \\ &\approx \mathbf{r}_i(t) + \Delta t\mathbf{v}_i(t) + \frac{\Delta t^2}{2m_i}\mathbf{F}_i(t).\end{aligned} \tag{2}$$

The velocity term disappears in the integration scheme in Eq. 2 by writing a similar expansion for $\mathbf{r}_i(t-\Delta t)$:

$$\mathbf{r}_i(t-\Delta t) \approx \mathbf{r}_i(t) - \Delta t\mathbf{v}_i(t) + \frac{\Delta t^2}{2m_i}\mathbf{F}_i(t). \tag{3}$$

Adding Eq. 2 and Eq. 3 gives:

$$\mathbf{r}_i(t+\Delta t) \approx 2\mathbf{r}_i(t) - \mathbf{r}_i(t-\Delta t) + \frac{\Delta t^2}{2m_i}\mathbf{F}_i(t). \tag{4}$$

Finally, Eq. 4 is the well-known numerical solver known as the Verlet algorithm.[62] Here, one can propagate a trajectory forward in time by a time step Δt with a given starting point in the phase space. The Verlet algorithm does not use the velocity to determine the positions. One can compute the velocities at any point in the trajectory as a centered difference:

$$\mathbf{v}_i(t) = \frac{\mathbf{r}_i(t+\Delta t) - \mathbf{r}_i(t-\Delta t)}{2\Delta t}. \tag{5}$$

2.2.2 The velocity Verlet algorithm

One disadvantage of the Verlet algorithm is that two sets of positions $\mathbf{r}(t)$ and $\mathbf{r}(t-\Delta t)$ have to be stored in memory to compute the velocities. An alternative is the velocity Verlet algorithm[63] that explicitly evolves both positions and velocities from the fact the Newton's equations of motion are time-reversible. So, one can start from $\mathbf{r}_i(t+\Delta t)$ and move by a time step of $-\Delta t$ as

$$\mathbf{r}_i(t) \approx \mathbf{r}_i(t+\Delta t) - \Delta t \mathbf{v}_i(t+\Delta t) + \frac{\Delta t^2}{2m_i}\mathbf{F}_i(t+\Delta t). \tag{6}$$

The velocities $\mathbf{v}_i(t+\Delta t)$ are then propagated as

$$\mathbf{v}_i(t+\Delta t) \approx \mathbf{v}_i(t) + \frac{\Delta t}{2m_i}\left[\mathbf{F}_i + \mathbf{F}_i(t+\Delta t)\right]. \tag{7}$$

Both the Verlet and the velocity Verlet integrators fulfill important properties that are crucial for the numerical stability. They both satisfy time-reversibility, that is propagating the equations backward in time will produce the (back) same trajectory, and share the symplectic property. Therefore, the stability is directly related to the ability of conserving energy and momentum throughout the propagated trajectory. A detailed discussion of these issues associated with numerical integrators can be found on pp. 100-113 of Tuckerman's book.[61]

2.3 Temperature coupling: The Nosé-Hoover thermostat

In the standard MD methodologies, the Newton's equations of motion of the particles N in a fixed volume V are solved numerically. If the total energy E is also conserved, the time evolution of the system belongs to the microcanonical ensemble (constant NVE). According to the ergodicity hypothesis, one can replace the average quantities computed along the trajectory (*i.e.* time averages) by ensemble averages in the microcanonical ensemble.[61] In practice, there is usually a need for performing MD simulations under the experimental conditions. Therefore, it is important to introduce ensembles with different sets of constant thermodynamical variables. In the canonical ensemble (constant NVT), a thermostat is introduced to modulate the temperature of a system. On the other hand, the isothermal-isobaric ensemble (constant NPT) allows for controlling of the temperature and pressure.

In order to constrain the average temperature of the system with a heat bath during the simulation, the extended-ensemble approach has proposed firstly by Nosé,[64,65] and

later modified by Hoover.[66] The Nosé-Hoover thermostat introduces an additional degree of freedom s and its conjugate momentum p_s to the Hamiltonian of a system. This gives the Hamiltonian of the extended system of the N particles and parameter s in terms of the virtual variables as

$$\mathscr{H}_{\text{Nosé}} = \sum_{i=1}^{N} \frac{\mathbf{p}_i^2}{2m_i s^2} + V(\mathbf{r}_1, \ldots, \mathbf{r}_N) + \frac{p_s^2}{2Q} + gkT \ln s, \tag{8}$$

where $g = 3N + 1$ is the number of independent momentum degrees of freedom of the system, $V(\mathbf{r}_1, \ldots, \mathbf{r}_N)$ is the potential energy, k and T are the Boltzmann constant and the target temperature, respectively. The variable s is introduced here as a time-scaling parameter to scale the velocities in order to shift the instantaneous kinetic energy towards the target level. Q is an imaginary mass, associated with the parameter s.

The equations of motions obtained from the extended Hamiltonian $\mathscr{H}_{\text{Nosé}}$ are:

$$\begin{aligned}
\dot{\mathbf{r}}_i &= \frac{\partial \mathscr{H}_{\text{Nosé}}}{\partial \mathbf{p}_i} = \frac{\mathbf{p}_i}{m_i s^2} \\
\dot{\mathbf{p}}_i &= -\frac{\partial \mathscr{H}_{\text{Nosé}}}{\partial \mathbf{r}_i} = \mathbf{F}_i \\
\dot{s} &= \frac{\partial \mathscr{H}_{\text{Nosé}}}{\partial p_s} = \frac{p_s}{Q} \\
\dot{p}_s &= -\frac{\partial \mathscr{H}_{\text{Nosé}}}{\partial s} = \sum_{i=1}^{N} \frac{\mathbf{p}_i^2}{m_i s^3} - \frac{gkT}{s} = \frac{1}{s}\left[\sum_{i=1}^{N} \frac{\mathbf{p}_i^2}{m_i s^2} - gkT\right].
\end{aligned} \tag{9}$$

The $\dot{\mathbf{r}}_i$ and $\dot{p}_s$ equations show that the thermostatting scheme works on an unconventional kinetic energy $\sum_{i=1}^{N} \frac{\mathbf{p}_i^2}{m_i s^2}$. One can transform these equations back into a more convenient form by introducing the following change of variables:

$$\mathbf{p}_i' = \frac{\mathbf{p}_i}{s}, \quad \mathrm{d}t' = \frac{\mathrm{d}t}{s}, \quad \frac{1}{s}\frac{\mathrm{d}s}{\mathrm{d}t'} = \frac{\mathrm{d}\eta}{\mathrm{d}t'}, \quad p_s = p_\eta. \tag{10}$$

Then, the equations of motions are re-defined as:

$$\begin{aligned}
\dot{\mathbf{r}}_i &= \frac{\mathbf{p}_i}{m_i}, \\
\dot{\mathbf{p}}_i &= \mathbf{F}_i - \frac{p_\eta}{Q}\mathbf{p}_i, \\
\dot{\eta} &= \frac{p_\eta}{Q}, \\
\dot{p}_\eta &= \sum_{i=1}^{N} \frac{\mathbf{p}_i^2}{m_i} - gkT.
\end{aligned} \tag{11}$$

Here, we can see that the conjugate momentum p_s is proportional to the friction coefficient η which responds to how closely the kinetic of the system follows the target temperature. Therefore, the evolution of the p_η term is driven by the difference between the instantaneous kinetic energy and its canonical average gkt. It is important to note here that the Nosé-Hoover system lacks the ergodicity, therefore does not yield the canonical distribution. This problem is discussed extensively in literature, and details can be

found in the Ref.[61] Nevertheless, this problem can be recovered with the Nosé-Hoover *chain* of thermostats. The idea consists of coupling the physical variable p_η with itself to a Nosé-Hoover thermostat using a new set of variables $\tilde{\eta}$ and $\tilde{p_\eta}$ and to then couple this thermostat with a second one, which can be coupled to a third one, and so on.[67] In practice, a chain length is truncated at some point giving a Nosé-Hoover chain of length N.

2.4 Molecular dynamics simulations with force fields

Force fields use simplified (empirical) potential functions to mimic the interactions between atoms. Each atom in this classical framework is represented by a sphere (point-like particle) at position $\mathbf{r}$. Thus, the total potential is defined as

$$U(\mathbf{r}) = U_{bonded}(\mathbf{r}) + U_{non-bonded}(\mathbf{r}). \tag{12}$$

Eq. 12 consists of two components. The first component represents the valance terms, which are the bonding interactions including bond stretch, bond angle bending, dihedral angle torsion terms. The last component describes the non-bonded interactions: van der Waals and Coulomb electrostatic potential. Therefore, the total potential energy can be written as

$$\begin{aligned} U(\mathbf{r}_1,...,\mathbf{r}_N) = &\sum_{bonds} K_b(b-b_0)^2 + \sum_{angles} K_\theta(\theta-\theta_0)^2 + \sum_{dihedrals} K_\phi(1+\cos n\phi - \delta) \\ &+ \sum_{improper} K_\psi(\psi-\psi_0)^2 + \sum_{i,j>i} \frac{1}{4\pi\epsilon}\frac{q_i q_j}{|r_{ij}|} + 4\epsilon_{ij}\left[\left(\frac{\sigma_{ij}}{r_{ij}}\right)^{12} - \left(\frac{\sigma_{ij}}{r_{ij}}\right)^{6}\right], \end{aligned} \tag{13}$$

where b, θ, ϕ, and ψ are the bond lengths, bond angles, torsional dihedral angles, and improper dihedral angles. The variables with a 0 as subscript are the equilibrium values. The label K corresponds to force constants. Normally, all bonded interactions are represented by harmonic functionals, except for the torsional dihedral angle term, which has a trigonometric form. On the other hand, the last two terms (non-bonded interactions) are accounted for a Coulomb-type pairwise interaction based on their charges (q_i), and the van der Waals term computed by the Lennard-Jones potential,[68] in which ϵ_{ij} is the well-depth parameter and σ_{ij} is the distance at which the two terms in the potential exactly balance.

Generally, classical simulations are performed efficiently on large scale systems, mostly on biomolecular systems.[69,70] As a result of using periodic boundary conditions, the system size becomes quasi infinite. Consequently, the number of interacting particle pairs increases enormously on the expense of evaluation of the interactions. For the short range interactions, this problem can be overcome by using a potential with a finite range (neighbor list), and then evaluate the term up to a certain distance (cutoff distance $\mathbf{R}_{cut}$) and neglect the rest. For the long range Coulomb interaction, the slow decay of this potential prevents using of such a cutoff criterion. Therefore, this long range Coulomb term is calculated normally in Fourier space with Ewald summation-related approaches to increase computational speed.[71]

Summarizing, such an empirical treatment of interactions of many particle system naturally cannot account for the quantum nature of electrons, thus any chemical reactions involving bond breaking/-forming is beyond the scope of this classical representation.

2.5 *Ab initio* molecular dynamics

Accounting for the properties of chemical reactions, or for chemically complex systems that are not possible to treat with empirical potentials requires a more realistic description of electronic structure. In order to do this, the many particle potential has to be calculated by solving the Schrödinger equation of the complex molecular system with a quantum mechanical treatment without any empirical parameter. This technique is the so-called *ab initio* molecular dynamics simulations.[72–75] The main idea in *ab initio* methods relies on computation of forces acting on the nuclei ön-the-flyäs the molecular dynamics trajectory is propagated. Special focus in this thesis is given to the Born-Oppenheimer molecular dynamics simulations, in which the forces are calculated in terms of the electronic ground state density according to the Hellmann-Feynman theorem:[76,77]

$$\mathbf{F}_I(t) = -\nabla_I \langle \Psi_0 | \hat{H}_e | \Psi_0 \rangle. \tag{14}$$

The dynamics of the system is propagated by a set of Newton's equations of motion within the Born-Oppenheimer approach. *Ab initio* molecular dynamics can be understood as a unification of molecular dynamics and electronic structure theory. In the following Section, we will give a brief theoretical background to the approximations that are used in electronic structure calculations starting with the Born-Oppenheimer approximation.

2.6 Electronic structure methods

2.6.1 Many electron system

Describing the properties of the many electron system is a very complicated task due to the highly complex quantum character of electrons.[78] Therefore, the main strategy here is to provide approximate solutions to the Schrödinger equation:[79]

$$\hat{H}|\Psi\rangle = E|\Psi\rangle, \tag{15}$$

where $\hat{H}$ is the Hamiltonian for a system of nuclei and electrons described by $\mathbf{R}_\alpha$ and $\mathbf{r}_i$, respectively. The Hamiltonian operator of a system of N interacting non-relativistic electrons, and M nuclei can be written as

$$\hat{H} = -\frac{1}{2}\sum_{i=1}^{N}\nabla_i^2 - \frac{1}{2}\sum_{\alpha=1}^{M}\nabla_\alpha^2 - \sum_{i=1}^{N}\sum_{\alpha=1}^{M}\frac{-Z_\alpha}{|\,\mathbf{r}_i - \mathbf{R}_\alpha\,|} + \frac{1}{2}\sum_{i=1}^{N}\sum_{j>i}^{N}\frac{1}{|\,\mathbf{r}_i - \mathbf{r}_j\,|} + \frac{1}{2}\sum_{\alpha=1}^{M}\sum_{\beta>\alpha}^{M}\frac{Z_\alpha Z_\beta}{|\,\mathbf{R}_\alpha - \mathbf{R}_\beta\,|}. \tag{16}$$

In Eq. 16, the first two terms are the kinetic energy operator of the electrons and nuclei, the third term describes the electron-nuclei interactions, and the last terms represent

the interactions between electrons and between nuclei, respectively. For $N >> 1$, a highly accurate solution of the Schrödinger equation is almost impossible, which makes it necessary to deal this problem with reasonable approximations.

2.6.2 The Born-Oppenheimer approximation

In a molecule, the nuclei are much heavier and move slowly compared to electrons, and thus they can be treated as classical particles. This allows us to consider the electrons to only feel the effect of slowly moving nuclei.[80] Correspondingly, a quasi-separable ansatz to solve the many particle Schrödinger equation is introduced as

$$\Psi(\mathbf{r}_i;\mathbf{R}_\alpha) = \Psi_e(\mathbf{r}_i;\mathbf{R}_\alpha)\Psi_n(\mathbf{R}_\alpha), \tag{17}$$

where $\Psi_n(\mathbf{R}_\alpha)$ is the nuclear wave function and $\Psi_e(\mathbf{r}_i;\mathbf{R}_\alpha)$ is the electronic wave function that depends parametrically on the nuclear positions. Within the Born-Oppenheimer approximation, the kinetic energy of nuclei is neglected, and the nuclei-nuclei interaction is defined to be constant. The remaining terms in Eq. 17 therefore represent the motion of electrons, the so-called the electronic Hamiltonian:

$$\hat{H}_e = -\frac{1}{2}\sum_{i=1}^{N}\nabla_i^2 - \sum_{i=1}^{N}\sum_{\alpha=1}^{M}\frac{-Z_\alpha}{\mid \mathbf{r}_i - \mathbf{R}_\alpha \mid} + \frac{1}{2}\sum_{i=1}^{N}\sum_{j>i}^{N}\frac{1}{\mid \mathbf{r}_i - \mathbf{r}_j \mid}. \tag{18}$$

The solution of the Schrödinger equation, which involves only the electronic degrees of freedom can be written as follows:

$$\hat{H}_e|\Phi_e\rangle = \mathscr{E}_e|\Phi_e(\mathbf{R}_\alpha)\rangle, \tag{19}$$

where $\mathscr{E}_e$ is the total electronic energy. Eq. 19 is the main outcome of the Born-Oppenheimer approximation by allowing for computing the electronic structure of a many electron system without providing anything about the quantum mechanics of the nuclei. Therefore, the total energy for fixed nuclei coordinates can be written down by simply adding back the constant nuclei-nuclei interaction:

$$\mathscr{E}_{tot} = \mathscr{E}_e(\mathbf{R}_\alpha) + \frac{1}{2}\sum_{\alpha=1}^{M}\sum_{\beta>\alpha}^{M}\frac{Z_\alpha Z_\beta}{\mid \mathbf{R}_\alpha - \mathbf{R}_\beta \mid}. \tag{20}$$

Similarly, the nuclear Hamiltonian can be defined in the average field generated by fast moving electrons:

$$\hat{H}_n = -\frac{1}{2}\sum_{\alpha=1}^{M}\nabla_\alpha^2 + \mathscr{E}_{tot}(\mathbf{R}_\alpha). \tag{21}$$

Here, the total energy $\mathscr{E}_{tot}(\mathbf{R}_\alpha)$ gives us the so-called Born-Oppenheimer surface as a function of the nuclear coordinates. Ultimately, we can now concern to solve only the purely electronic problem for fixed nuclei and subsequently, with the obtained surfaces, the purely the nuclear problem.

Summarizing, the Born-Oppenheimer picture assumes that the electrons respond instantaneously to the nuclear motion, therefore, it is sufficient to obtain only one set of instantaneous electronic eigenvalues and eigenfunctions at each nuclear configuration.

However, this representation is shown to fail when two (or more) electronic solutions to the electronic Schrödinger equation come close energetically, due to non-adiabatic effects, contained in the terms that have not been considered in the above derivation. These effects do not play a role in the field of research in this work. Thus, they are considered as not falling within the scope of this discussion so that from now on only the electronic Hamiltonian and electronic wave functions will be represented which obey the Schrödinger equation.

2.6.3 Hartree-Fock theory

The Hartree-Fock method is wave function based approach together with the variational principle.[81,82] This method constructs the many electron wave function Ψ by satisfying the desired antisymmetry condition, as the so-called Slater determinant from a single-electron orbital:[83–85]

$$\Psi = \frac{1}{\sqrt{N!}} \begin{vmatrix} \psi_1(\mathbf{r}_1,\sigma_1) & \psi_2(\mathbf{r}_1,\sigma_1) & \cdots & \psi_N(\mathbf{r}_1,\sigma_1) \\ \psi_1(\mathbf{r}_2,\sigma_2) & \psi_2(\mathbf{r}_2,\sigma_2) & \cdots & \psi_N(\mathbf{r}_2,\sigma_2) \\ \vdots & \vdots & & \vdots \\ \psi_1(\mathbf{r}_N,\sigma_N) & \psi_2(\mathbf{r}_N,\sigma_N) & \cdots & \psi_N(\mathbf{r}_N,\sigma_N) \end{vmatrix}, \tag{22}$$

where $\psi_i(\mathbf{r}_i,\sigma_i)$ are the single-electron wave functions. The essence of the Hartree-Fock approximation relies on replacing the many electron problem by a single electron case in which electron-electron interaction is represented in an average way *i.e.* a mean-field potential. According to the variational principle, these single-electron wave functions are then the "bestßet of those spin orbitals, which minimize the electronic energy. To perform this minimization scheme, it is therefore convenient to split the electronic Hamiltonian into a sum of single electron terms $\hat{h}(\mathbf{r}_i)$, which describes the motion of the $i^t h$ electron under the influence of the mean-field potential:

$$\hat{f} = \sum_i \hat{h}(\mathbf{r}_i) + \frac{1}{2}\sum_{i=1}^{N}\sum_{i>j}^{N} \frac{1}{|\,\mathbf{r}-\mathbf{r}'\,|}, \tag{23}$$

where $\hat{f}$ is the Fock operator, and the $\hat{h}_i$ term is defined as

$$\hat{h}_i = -\frac{1}{2}\nabla_i^2 - \sum_{\alpha=1}^{M} \frac{Z_\alpha}{|\,\mathbf{r}_i-\mathbf{R}_\alpha\,|}. \tag{24}$$

It is important to note here that, we discuss here only the closed shell equations, which are distinguished by an even number of electrons *i.e.* two electrons with opposite spin occupy one spatial orbital. This allows the elimination of the spin component in the wave function representation. Solving the Fock equation under an orthonormality constraint for the different $\psi_i(\mathbf{r})$, therefore, will give us the spatial wave function and the single-electron energy associated with either of the electrons:

$$\hat{f}\psi_i(\mathbf{r}) = \hat{h}\psi_i(\mathbf{r}) + \underbrace{2\sum_j^{N/2}\int \frac{\psi_j^*(\mathbf{r}')\psi_j(\mathbf{r}')}{|\mathbf{r}-\mathbf{r}'|}\psi_i(\mathbf{r})\,d\mathbf{r}'}_{\hat{\mathbf{J}}\psi_i(\mathbf{r})} - \underbrace{\sum_j^{N/2}\int \frac{\psi_j^*(\mathbf{r}')\psi_i(\mathbf{r}')}{|\mathbf{r}-\mathbf{r}'|}\psi_j(\mathbf{r})\,d\mathbf{r}'}_{\hat{\mathbf{K}}\psi_i(\mathbf{r})}. \tag{25}$$

Here, the operators $\hat{\mathbf{J}}$ and $\hat{\mathbf{K}}$ result from the electron-electron interaction term in the total Hamiltonian of the many electron system, can be examined by means of operating on a wave function $\psi_i(\mathbf{r})$, which represents the electron 1:

$$\hat{\mathbf{J}}_j \psi_i(1) = \left[\int \psi_j^*(\mathbf{r}') \frac{1}{|\mathbf{r}-\mathbf{r}'|} \psi_j(\mathbf{r}') d\mathbf{r}' \right] \psi_i(1), \tag{26}$$

and

$$\hat{\mathbf{K}}_j \psi_i(1) = \left[\int \psi_j^*(\mathbf{r}') \frac{1}{|\mathbf{r}-\mathbf{r}'|} \psi_i(\mathbf{r}') d\mathbf{r}' \right] \psi_j(1). \tag{27}$$

The operator $\hat{\mathbf{J}}$ describes the classical interaction of the electron densities the so-called Coulomb term. It can easily be seen that the quantity $\psi_j^*(\mathbf{r}')\psi_j(\mathbf{r}')$ represents the charge distribution due to an electron in orbital j. Therefore, the evaluation of this integral with a sum over all $i \neq j$ gives the total (local) potential energy (Hartree potential) at $\mathbf{r}$ due to the average charge density produced by all the other electrons. On the other hand, the exchange potential, $\hat{\mathbf{K}}$, has no classical analogue, and is a direct result of the antisymmetric nature of the Slater determinant. Unlike the Coulomb term, the exchange operator has a non-local character.

Having made these assumptions, one can introduce the Hartree-Fock equations, which describe electrons under the influence of the mean-field potential:

$$\hat{f}(i)\psi_i(\mathbf{r}) = \varepsilon \psi_i(\mathbf{r}). \tag{28}$$

Eq. 28 depends on the spatial orbitals of other electrons, and thus, must be solved iteratively. The scheme for solving the Hartree-Fock equation is the so-called the self-consistent field (SCF) method. By introducing an initial guess for the orbitals, one can compute the average field felt by each electron, and then solve the Hartree-Fock equation for a new set of orbitals. This procedure is repeated until the fields no longer change. The solution of the Hartree-Fock equation leads a set of orthonormal orbitals, the so-called Fock orbitals.

The total energy of the many electron system can be written as:

$$E_{HF} = 2 \sum_{i=1}^{N/2} \hat{h}_i - \sum_{i,j=1}^{N/2} (2\hat{\mathbf{J}}_{ij} - \hat{\mathbf{K}}_{ij}). \tag{29}$$

Although the Hartree-Fock approximation yields reasonable optimized geometries and molecular properties, it is found to fail in certain cases such as calculation of dissociation energies. This is due to the assumptions of Hartree-Fock method, which ignores any correlation in the motion of electrons with parallel spin (closed shell case). Thus, the difference of the Hartree-Fock energy to the true energy is defined as the correlation energy. There are a various of methods, which have been developed in order to introduce the correlation effects.[86–88] In practice, all these theories rely on a linear combination of the total wave function in several determinants of the form. Due to the high computational cost of such methods, it is not feasible to perform calculations of realistic models of systems with these methods.

2.6.4 Density functional theory

Density functional theory (DFT) reformulates the many electron problem in terms of the electron density alone.[89–94] This approach simplifies the many electron problem significantly, since the electron density is a function with three variables, namely the x, y, and z position of the electrons. DFT is presently the most successful approach to compute a various non-degenerate ground state molecular properties, *e.g.* molecular structures, spectroscopic features, dipole moments. However, the reliability of DFT depends on the exchange-correlation energy functional. This section will give a short introduction to DFT and its fundamentals.

2.6.5 Hohenberg-Kohn theorems

The Hohenberg-Kohn (HK) theorems[89,90] describe the system of interacting electrons moving under the external potential $V_{ext}(\mathbf{r})$. The HK theorems are stated as follows:[89,90]

Theorem 1: The external potential $V_{ext}(\mathbf{r})$ up to an arbitrary constant is a unique function of the ground state density $\rho(\mathbf{r})$.

Proof: The first HK theorem can be proven in a simple and extremely elegant manner using the principle of *reductio ad absurdum* for a non-degenerate system. Suppose there exist two potentials $V_1(\mathbf{r})$ and $V_2(\mathbf{r})$ differing by more than a constant, and giving rise to the same ground-state density $\rho(\mathbf{r})$. These potentials belong to distinct Hamiltonians, which give rise to distinct wave functions Ψ_1 and Ψ_2. Then we have

$$\begin{aligned} E_1 &= \langle \Psi_1 \mid \hat{H}_1 \mid \Psi_1 \rangle \\ &= \langle \Psi_1 \mid \hat{T} + \hat{V}_{ee} \mid \Psi_1 \rangle + \int V_1(\mathbf{r})\rho(\mathbf{r})d\mathbf{r}, \end{aligned} \tag{30}$$

and

$$\begin{aligned} E_2 &= \langle \Psi_2 \mid \hat{H}_2 \mid \Psi_2 \rangle \\ &= \langle \Psi_2 \mid \hat{T} + \hat{V}_{ee} \mid \Psi_2 \rangle + \int V_2(\mathbf{r})\rho(\mathbf{r})d\mathbf{r}. \end{aligned} \tag{31}$$

Here, the operators $\hat{T}$ and $\hat{V}_{ee}$ are the electron kinetic energy and electron interaction energy, respectively. Since the ground-state energy of the system is non-degenerate, the variational principle gives two inequalities:

$$\begin{aligned} E_1 &< \langle \Psi_2 \mid \hat{H}_1 \mid \Psi_2 \rangle \\ &= \langle \Psi_2 \mid \hat{T} + \hat{V}_{ee} \mid \Psi_2 \rangle + \int V_1(\mathbf{r})\rho(\mathbf{r})d\mathbf{r} \\ &= E_2 + \int [V_1(\mathbf{r}) - V_2(\mathbf{r})]\rho(\mathbf{r})d\mathbf{r} \end{aligned} \tag{32}$$

and

$$\begin{aligned} E_2 &< \langle \Psi_1 \mid \hat{H}_2 \mid \Psi_1 \rangle \\ &= E_1 + \int [V_2(\mathbf{r}) - V_1(\mathbf{r})]\rho(\mathbf{r})d\mathbf{r}. \end{aligned} \tag{33}$$

Adding Eq. (32) and Eq. (33), we obtain

$$E_1 + E_2 < E_2 + E_1, \tag{34}$$

which is clearly a contradiction. So, there are no two different external potentials that can give the same electron density $\rho(\mathbf{r})$. Thus, $\rho(\mathbf{r})$ uniquely determines $V_{ext}(\mathbf{r})$, and all other ground state electronic properties can be obtained from it.

Theorem 2: The ground state energy can be obtained variationally according to the electron density that minimizes the total energy functional $E[\rho]$ being the exact ground state density. Then, we can write the total energy functional as a function of the electronic density as

$$E[\rho] := \langle \Psi[\rho] \mid \hat{T} + \hat{V}_{ee} + V_{ext}(\mathbf{r}) \mid \Psi[\rho] \rangle = F_{HK}[\rho] + \int V_{ext}(r)\rho(\mathbf{r})d\mathbf{r}, \tag{35}$$

where $F_{HK}[\rho] = \langle \Psi[\rho] \mid (\hat{T} + \hat{V}_{ee}) \mid \Psi[\rho] \rangle$. $F_{HK}[\rho]$ requires no explicit knowledge of $V_{ext}(\mathbf{r})$; therefore it is same for all systems and called a *universal* functional.

Proof: The ground state the energy can be defined by the unique ground state density, $\rho(\mathbf{r})$ as

$$E[\rho(\mathbf{r})] = \int V_{ext}(\mathbf{r})\rho(\mathbf{r})d\mathbf{r} + F[\rho(\mathbf{r})], \tag{36}$$

and the variational principle states that a different density, $\rho'(\mathbf{r})$ will necessarily give a higher energy

$$F[\rho'(\mathbf{r})] + \int V_{ext}(\mathbf{r})\rho'(\mathbf{r})d\mathbf{r} \geq F[\rho(\mathbf{r})] + \int V_{ext}(\mathbf{r})\rho(\mathbf{r})d\mathbf{r}, E[\rho'(\mathbf{r})] > E[\rho(\mathbf{r})]. \tag{37}$$

So the total electronic energy will reach the minimum only, when the electron density is the non-degenerate ground state electron density.

It is now important to note that the electron density, which minimizes the energy over densities associated with the existing potential of non-interacting systems, is the so-called *v-representable*. However, it is not clear whether an arbitrary density could be represented by an antisymmetric many electron wave function (*N-representable*). It has been shown that any "reasonableëlectron density fulfills the *N-representable* condition. The solution to the *v-representable* problem, on the other hand, introduced by the Levy-Lieb constrained search formalism[95,96] shows that there is no formal problem with the HK theorems.

2.6.6 The Kohn-Sham method

The idea of the Kohn-Sham method[91] is to rewrite the system of many interacting electrons as a system of *non-interacting* Kohn-Sham particles in a local (effective) potential $v_s(\mathbf{r})$. In such a *non-interacting* electron treatment, the wave function can always be written as an antisymmetric product of orthonormal single electron orbitals ($\psi_i(\mathbf{r})$) *i.e.* Kohn-Sham orbitals, which satisfy the equations:

$$\left(\frac{1}{2}\nabla^2 + v_s(\mathbf{r})\right)\psi_i(\mathbf{r}) = \epsilon_i\psi_i(\mathbf{r}) \tag{38}$$

and yields

$$\rho(\mathbf{r}) = \sum_i |\psi_i(\mathbf{r})|^2. \tag{39}$$

With the direct consequence of the second Hohenberg-Kohn theorem (simply the variational principle), we can show that there is only one effective potential $v_s(\mathbf{r})$, which produces the ground state electron density $\rho(\mathbf{r})$ of the interacting system. Therefore, for a given ground state density alone, all properties of the many interacting electron system can be determined. The total electronic energy of Kohn-Sham system is given by

$$E[\rho(\mathbf{r})] = T_s[\rho(\mathbf{r})] + E_{ext}[\rho(\mathbf{r})] + E_H[\rho(\mathbf{r})] + E_{XC}[\rho(\mathbf{r})], \tag{40}$$

where $T_s[\rho(\mathbf{r})]$ is the non-interacting kinetic energy, $E_{ext}[\rho(\mathbf{r})]$ the interaction energy with the external potential provided by the nuclei, $E_H[\rho(\mathbf{r})]$ the classical electrostatic interaction energy, and $E_{XC}[\rho(\mathbf{r})]$ the exchange-correlation energy.

The functional $v_s(\mathbf{r}$ is implicitly defined by the Kohn-Sham equations, is split into the following contributions:

$$v_s[\rho(\mathbf{r})] = v_{ext}[\rho(\mathbf{r})] + v_H[\rho(\mathbf{r})] + v_{XC}[\rho(\mathbf{r})], \tag{41}$$

where the first term $v_{ext}[\rho(\mathbf{r})]$ is the external potential introduced by the nuclei-electron interaction, the second term is the Hartree potential, and the $v_{XC}[\rho(\mathbf{r})]$ term is the exchange-correlation potential, which contains all non-classical electron interactions, and a correction to the non-interacting kinetic energy.[97] The exchange-correlation potential can be defined as a functional derivative of $E_{XC}[\rho(\mathbf{r})]$:

$$v_{XC}[\rho(\mathbf{r})] = \frac{\delta E_{XC}[\rho(\mathbf{r})]}{\delta \rho(\mathbf{r})}. \tag{42}$$

The form of $v_{XC}[\rho(\mathbf{r})]$ is unknown. So, given an approximation to the exchange-correlation functional, the Kohn-Sham equations can be solved self-consistently, which yields the electron density $\rho(r)$. By inserting this into the energy functional, the total electronic energy of the interacting system can be obtained. In the Kohn-Sham framework, the difficult task that involves in finding a good approximation for the exchange-correlation functional.

2.6.7 Approximations to exchange-correlation energy

The calculation of the Kohn-Sham equations starts with an initial guess for the orbitals, and thus for the electron density. The accuracy of DFT strongly depends on finding a good approximation the exchange-correlation energy functional. A number of different approximations have been developed, ranging from simple local approximations based on the homogeneous electron gas to rather sophisticated functionals incorporating *e.g.* sums over the unoccupied orbitals. Below, we discuss some of the most popular approximations for the exchange-correlation energy.[98]

Local density approximation

The simplest approximation for the exchange-correlation energy E_{XC} is the local-density approximation (LDA).[99,100] In this approach, it is assumed that the exchange-correlation energy density at every position of space for the many electron system is the same as it would be for the homogeneous electron gas (HEG) having the same electron density. By knowing this fact, the exchange-correlation energy can be defined as

$$E_{XC}^{LDA} = \int \epsilon_{XC}^{HEG}(\rho(\mathbf{r}))\rho(\mathbf{r})d\mathbf{r}, \tag{43}$$

where $\epsilon_{XC}^{HEG}(\rho)$ is the exchange-correlation energy per electron in the homogeneous electron gas with the density ρ. Thus, the exchange-correlation potential v_{XC} takes the form

$$v_{XC}^{LDA}(\mathbf{r}) = \frac{\delta E_{XC}[\rho]}{\delta\rho(\mathbf{r})} = \epsilon_{XC}^{HEG}(\rho(\mathbf{r})) + \rho(\mathbf{r})\frac{\delta\epsilon_{XC}^{HEG}}{\delta\rho}|_{\rho=\rho(\mathbf{r})}. \tag{44}$$

In practice, the exchange-correlation energy ϵ_{XC} can be divided into the exchange energy ϵ_X and the correlation energy ϵ_C:

$$\epsilon_{XC}(\rho(\mathbf{r})) = \epsilon_X(\rho(\mathbf{r})) + \epsilon_C(\rho(\mathbf{r})). \tag{45}$$

The analytical expression for the exchange energy is known exactly:[92,99]

$$E_X(\rho(\mathbf{r})) = \int \epsilon_X^{HEG}(\rho(\mathbf{r}))\rho(\mathbf{r})d\mathbf{r} = -\frac{3}{4}\left(\frac{3}{\pi}\right)^{1/3}\int \rho(\mathbf{r})^{4/3}d\mathbf{r}. \tag{46}$$

Unlike the exchange term, the exact analytic form of correlation term is known only for two limiting cases.[101–103] Generally, the ε_C term is parameterized based on quantum Monte Carlo calculations[104] of homogeneous electron gases at various densities.

Obviously, the LDA functionals can be expected to work well for a system with slowly varying electron density. But, there are various, typically weakly bonded systems such as hydrogen bonded systems which cannot be described by LDA sufficiently. Therefore, more sophisticated approximations are needed for representing the unknown exchange-correlation potential.

Generalized-gradient approximation

An improvement to the LDA was made by accounting for the local variations of the electron density, which is the so-called generalized-gradient approximation (GGA).[105] In this case, the exchange-correlation functional depends not only on the electron density, but also on the gradient of the density as well. Symbolically, such a form of functional can be defined as:

$$E_{XC}^{GGA}[\rho] = \int f^{GGA}(\rho(\mathbf{r}), \nabla\rho(\mathbf{r}))d\mathbf{r}. \tag{47}$$

The flexibility in the choice of f^{GGA} ensures the improvements of the GGA exchange-correlation functional to the LDA exchange-correlation. In the GGA approximation, the

exchange term takes the form

$$E_X^{GGA}[\rho] = \int \epsilon_X^{HEG}(\rho(\mathbf{r}))\rho(\mathbf{r})F_X^{GGA}(s)d\mathbf{r}, \tag{48}$$

where $F_x^{GGA}(s)$ is the enhancement factor with a dimensionless gradient s

$$s = \frac{|\nabla\rho(\mathbf{r})|}{2(3\pi^2)^{1/3}\rho(\mathbf{r})^{4/3}}. \tag{49}$$

Within the GGA family, the exchange-correlation functionals differ only in the choice of the enhancement function. The most popular GGAs are the so-called PBE (Perdew, Burke, and Ernzerhof) functional,[106] and BLYP (denoting the combination of Becke's 1988 exchange functional[107] with the 1988 correlation functional of Lee, Yang and Parr[108]). Generally, the GGA functionals describe all main types of chemical bonds sufficiently, and provide an accurate prediction of electronic and structural properties. However, they are found to fail to describe dispersion interactions. A further problem is that these local functionals exhibit an exponential decay, whereas the exact behaviour should decay as $1/\mathbf{r}$.

Hybrid functionals

As shown in the discussions above, the exchange functionals within the LDA and GGA families do not consider the non-local dependence on the electron density. The main idea behind the hybrid theory is to combine a local or a semi-local exchange-correlation functional with the non-local Hartree-Fock exchange term.[109] This approach was formalized by Becke[110] to correct the Hartree-Fock scheme in order to account for correlation effects, and to incorporate the exact exchange into DFT calculations. Such a hybrid functional, for example B3LYP,[108,110,111] has the following form:

$$E_{XC}^{B3LYP} = E_X^{LDA} + a_0(E_X^{HF} - E_X^{LDA}) + a_X(E_X^{GGA} - E_X^{LDA}) + E_C^{LDA} + a_C(E_C^{GGA} - E_C^{LDA}), \tag{50}$$

where a, a_X, and a_C are mixing coefficients that can be fitted empirically or estimated via perturbation theory.[109,112] Such hybrid functionals have been shown to offer noticeably improved performance over local functionals, especially for the treatment of dispersion forces.

2.7 Matrix form of the Kohn-Sham equations

The Kohn-Sham (also Hartree-Fock) equations represent a complicated system of coupled differential equations.[113] Because the Kohn-Sham Hamiltonian is a function of $\rho(\mathbf{r})$, which is in turn a function of $\psi_i(\mathbf{r})$, the set of equations results in solving a non-linear problem. Optimizing the electronic energy requires an iterative scheme until Kohn-Sham (or Fock) orbitals do not change the background potential any further. This iterative scheme is called a self-consistent field (SCF) procedure.[114] The only difference between the SCF scheme of Kohn-Sham and Hartree-Fock results from the evaluation of the exchange-correlation potential.

Here, we introduce a constraint for the Kohn-Sham or Fock molecular orbitals $\psi_i(\mathbf{r})$ that can be written as linear combinations of the spatial basis functions χ_μ with expansion coefficients $C_{\mu i}$:[115,116]

$$\psi_i(\mathbf{r}) = \sum_\mu = C_{\mu i}\chi_\mu(\mathbf{r}). \tag{51}$$

From Eq. 51, evaluation of the Kohn-Sham molecular orbitals reduces to the problem of obtaining a set of expansion coefficients. In order to calculate these coefficients, one must reformulate the one electron eigenvalue problem as:

$$\sum_\mu C_{\mu i}\hat{f}(\mathbf{r})\chi_\mu(\mathbf{r}) = \epsilon_i \sum_\mu C_{\mu i}\chi_\mu, \tag{52}$$

where $\hat{f}$ is the Kohn-Sham or Fock operator in any single basis. Multiplying with $\chi^*_\nu(\mathbf{r})$ on the left side, and integrating over space, we obtain a matrix equation for determining $C_{\mu i}$:

$$\sum_\mu C_{\mu i}\int \chi^*_\nu(\mathbf{r})\hat{f}\chi_\mu(\mathbf{r})d\mathbf{r} = \epsilon_i \sum_\mu C_{\mu i}\int \chi^*_\nu(\mathbf{r})\chi_\mu(\mathbf{r}). \tag{53}$$

In Eq. 53, we define two Hermitian matrices, the first being the overlap matrix $\mathbf{S}$

$$\mathbf{S}_{\mu\nu} = \int \chi^*_\nu(\mathbf{r})\chi_\mu(\mathbf{r})d\mathbf{r}. \tag{54}$$

The second is the Kohn-Sham matrix $\mathbf{F}$ with elements

$$\mathbf{F}_{\mu\nu} = \int \chi^*_\nu(\mathbf{r})\hat{f}(\mathbf{r})\chi_\mu(\mathbf{r})d\mathbf{r}. \tag{55}$$

With these representations of $\mathbf{S}$ and $\mathbf{F}$, we can rewrite the Kohn-Sham equation as:

$$\sum_\nu \mathbf{F}_{\mu\nu}\mathbf{C}_{\nu i} = \epsilon_i \sum_\nu \mathbf{S}_{\mu\nu}C_{\mu i}. \tag{56}$$

Finally, one can reformulate entire problem in all i in compact matrix form, the so-called Roothaan-Hall equation:[117,118]

$$\mathbf{FC} = \mathbf{SC}\epsilon, \tag{57}$$

where $\mathbf{C}$ is a square matrix of the expansion coefficients and ϵ is a diagonal matrix of the orbital energies. Obviously, the overlap matrix reduces to the unity matrix ($\mathbf{S} = \mathbf{1}$) if we choose an orthogonal set of basis functions:

$$\mathbf{FC} = \mathbf{C}\epsilon. \tag{58}$$

This eigenvalue problem in turn can be solved by diagonalizing $\mathbf{F}$. Therefore, one has to orthogonalize the (non-orthogonal) basis functions first. It is important to realize here that the Kohn-Sham or Fock matrix $\mathbf{F}$ depends on the expansion coefficients $\mathbf{C}$ in terms of the density matrix:

$$\rho(\mathbf{r}) = \sum_{\mu\nu} P_{\mu\nu}\psi_\mu(\mathbf{r})\psi^*_\mu(\mathbf{r}), \quad P_{\mu\nu} = 2\sum_i^{N/2} C_{\mu i}C^*_{\nu i}. \tag{59}$$

The Roothaan-Hall equations represent a generalized non-linear eigenvalue problem, and can be solved with the self-consistent field procedure. In order to do this, we first guess a density matrix describing the positions of the electrons to calculate the effective one-electron potential. Then, the one-electron equations are solved to obtain a new set of molecular orbitals. With this new molecular orbitals, the new electron density can be obtained. This iterative cycle is then repeated until the density matrix no longer changes, *i.e.* self-consistency is achieved.

2.8 Basis sets

An inherent approximation that is used in essentially all *ab initio* methods is the introduction of a basis set. A basis set is a set of M specially adapted functions $\chi_{ij}(\mathbf{r})$, used to create the molecular orbitals $\psi_i(\mathbf{r})$, which are expanded as a linear combination with coefficients C_{ij} to be determined.

$$\psi_i(\mathbf{r}) = \sum_{j=1}^{M} C_{ij}\chi_j(\mathbf{r}). \tag{60}$$

Usually, these basis functions are centered on atoms, and not the exact atomic orbitals, even for the corresponding hydrogen-like atoms due to simplifications of their analytic formulas. Slater type orbitals (STOs) were used as basis functions due to their similarity with the eigenfunctions of the hydrogen atom. Their general definition is

$$\chi(\mathbf{r},\theta,\psi) = Nr^{n-1}e^{-\xi r}Y^{lm}(\theta,\psi), \tag{61}$$

with N being a normalization factor and Y^{lm} being the spherical harmonics. STOs have an advantage as they have a direct physical interpretation, and thus are naturally good basis for molecular orbitals. From a computational point of view, the STOs have the severe shortcoming that most of the required integrals needed in the course of the SCF procedure must be calculated numerically, which drastically decreases the speed of a computation.

2.8.1 Gaussian-type orbitals

The construction of basis sets from Gaussian-type orbitals (GTOs) is motivated by computational efficiency. They are defined as

$$G_{ijk} = Nx^i y^j z^k e^{-\alpha r^2}, \tag{62}$$

where N is the prefactor, and α is a positive orbital exponent. Here, each orbital is centered at a nucleus, *i.e.* the nucleus at the origin. With a proper choice of parameters, a set of GTOs can be used to describe any function, such as STOs. This allows for having efficient molecular integral evaluations with an acceptable description of the electronic structure. On the other hand, the GTOs have two major disadvantages due to the r^2 dependence in the exponential function. At the nucleus, the GTOs have zero slope compared to the the STO which has a "cusp"(discontinous derivative). Besides that, they fall off too rapidly for large $\mathbf{r}$, and the tail of the wave function is consequently represented

poorly. Nevertheless, a linear combination of several Gaussian functions can represent an atomic orbital in an approximate manner. As a result, a much faster computation of the two-electron integrals can be achieved with using the GTOs than STOs.

2.8.2 Plane waves

Plane waves are the most popular basis functions in the *ab initio* community, because their application to periodic systems is straightforward.[119] For periodic systems, the electronic wave function can be written as:

$$f(\mathbf{r}) = \frac{1}{\Omega} e^{i\mathbf{G}\cdot\mathbf{r}}, \tag{63}$$

where Ω and the vectors $\mathbf{G}$ are the volume of the unit cell and the reciprocal lattice vectors of the system, respectively. Applying the Bloch's theorem[119], the wave function of an electron in a periodic potential can be written as a product of a plane wave envelope function and a periodic function

$$\psi_{n\mathbf{k}}(\mathbf{r}) = e^{i\mathbf{k}\cdot\mathbf{r}} u_{n\mathbf{k}}(\mathbf{r}). \tag{64}$$

Due to the periodicity, $u_{n\mathbf{k}}(\mathbf{r})$ can be expanded in terms of a discrete plane-wave basis set

$$u_{n\mathbf{k}}(\mathbf{r}) = \sum_{\mathbf{G}} C_{n\mathbf{k}}(\mathbf{G}) e^{i\mathbf{G}.\mathbf{r}}. \tag{65}$$

Thus, the electron wave function can now be expressed as a linear combination of plane waves

$$\psi_{n\mathbf{k}}(\mathbf{r}) = \sum_{G} C_{n\mathbf{k}}(\mathbf{G}) e^{i(\mathbf{k}+\mathbf{G})\cdot\mathbf{r}}. \tag{66}$$

In principle, the set of plane waves $e^{i\mathbf{G}\cdot\mathbf{r}}$ should be infinite. However, the expansion must be truncated after a finite number of plane waves, due to the tremendous increase in the computational costs. The basis set truncation is controlled by a single parameter the so-called the plane wave cutoff E_{cut}, which has a dimension of energy. This kinetic cutoff energy is defined as:

$$\frac{1}{2}|k+G|^2 \leq E_{cut}. \tag{67}$$

Summarizing, a complete basis set of plane waves is independent from the positions of the nuclei, allowing for the calculations of forces acting on atoms via the Hellmann-Feynman theorem.[76,77] However, the electronic wave function shows rapid oscillations in the regions near to nuclei, so the related density gradients are not well described by plane waves, unless one uses a large number of them. Corresponding calculations, therefore, would be costly. In practice, the plane wave basis sets are often used in combination with pseudopotentials to describe the core electrons. The pseudopotential approach is used in almost all plane wave DFT calculations, which is described in detail in the next section. Further computational reduction can be achieved by transforming some other terms, *e.g.* the kinetic energy and the matrix elements of the Coulomb operator, from

real space to reciprocal space by means of fast Fourier transforms (details are given in Section 2.10).

2.9 Pseudopotentials

The computational cost of many electron problem increases dramatically with increasing system size (number of electrons) and level of accuracy. One way of reducing computational complexity is introduced by replacing the strong electron-nuclei potential and core electrons by an effective pseudopotential, the so-called a pseudopotential.[120] The essence of the pseudopotential is to describe only the valence electrons explicitly, including relativistic effects. In this approach, the true potential and valance wave functions outside a chosen core region r_c are reproduced by remaining much weaker and smoother inside. The valance electrons are represented by modified smooth pseudo wave functions in the core region, which must reproduce the original valence wave functions accurately.[121]

Most importantly, a pseudopotential should be transferable *i.e.* the same pseudopotential should be applicable for an atom in all possible environments. Furthermore, the pseudopotential needs to be norm conserving *i.e.* outside the core region the real and pseudo wave functions are identical, so that both wave functions generate identical charge densities

$$\int_0^{r_{c,l}} d\mathbf{r}\,|P^{PP}_{nloc}(\mathbf{r})|^2 = \int_0^{r_{c,l}} d\mathbf{r}\,|P^{AE}_{nloc}(\mathbf{r})|^2, \tag{68}$$

where $P^{AE}_{nloc}(\mathbf{r})$ is the all electron wave function and $P^{PP}_{nloc}(\mathbf{r})$ is the pseudo wave function, guarantying the equality of the all electron and pseudo wave functions outside the core region. Such a pseudopotential in general has the following non-local form for an atom, which uses a different potential for each angular momentum component of the pseudopotential

$$\hat{V}^{PP}(\mathbf{r},\mathbf{r}') = \hat{V}_{loc}\delta(\mathbf{r}-\mathbf{r}') + \sum_{l}^{l_{max}} \sum_{m=-l}^{m=l} (Y^{lm}(\theta,\phi))^* \hat{V}^{l}_{nloc}(\mathbf{r}) \frac{\delta(\mathbf{r}-\mathbf{r}')}{r^2} Y^{lm}(\theta',\phi'). \tag{69}$$

Pseudopotentials of this type are known as non-local, norm-conserving pseudopotentials[122], since they are capable of describing the scattering properties of an atom in a variety of environments. In our calculations, the pseudopotentials of Goedecker, Teter, and Hutter (GTH)[123,124] are used, which consist of a local part as

$$\hat{V}^{PP}_{loc}(\mathbf{r}) = -\frac{Z}{\mathbf{r}} erf(\frac{r}{\sqrt{2}r_{loc}}) \sum_{i=1}^{4} C^{PP}_i (\frac{\mathbf{r}}{\mathbf{r}_{loc}})^{2i-2} e^{(-\frac{1}{2}\frac{\mathbf{r}}{\mathbf{r}_{loc}})^2}, \tag{70}$$

and, the non-local part as:

$$\hat{V}^{PP}_{nloc}(\mathbf{r},\mathbf{r}') = \sum_{lm}\sum_{ij} \langle \mathbf{r}|p^{lm}_i\rangle h^l_{ij} \langle p^{lm}_j|\mathbf{r}',\rangle \tag{71}$$

The Gaussian-type projectors in Eq. 71 are defined

$$\langle \mathbf{r}|p^{lm}_i\rangle = N^l_i Y^{lm} r^{l+2i-2} e^{(-\frac{1}{2}\frac{\mathbf{r}}{\mathbf{r}_{loc}})^2}, \tag{72}$$

where N_i^l are normalization constants, Y^{lm} spherical harmonics, and $\mathbf{r}_{loc}$, $\mathbf{r}_l$ are the localization radius of the local pseudopotential term and of each projector, respectively. These free parameters can be computed by an optimized scheme in order to obtain a good compromise for the calculation of desired molecular properties.

Summarizing, the use of pseudopotentials provides an opportunity for the considerable reduction of the basis set size, which results in faster treatment of the large electronic systems.

2.10 The Gaussian plane wave method

Central in the Gaussian and plane wave (GPW) approach is to use a dual representation of the electron density.[125] The method represents Kohn-Sham orbitals with an atom-centered Gaussian-type basis, but uses an auxiliary plane wave basis to represent the electron density. This compact representation provides an efficient treatment of the electrostatic interactions, and thus leads to a scheme for the calculation of the total energy and construct the Kohn-Sham matrix that scales linearly with the system size. This scheme has been implemented in many software packages for example in Cp2k[14], which is used for performing atomistic simulations in this thesis. The formulation of GPW method closely follows the Ref.[125].

The expansion of the electron density in the Gaussian basis $\psi_\mu(\mathbf{r})$ can be written as

$$\rho(\mathbf{r}) = \sum_{\mu\nu} \mathbf{P}^{\mu\nu} \psi_\mu(\mathbf{r}) \psi_\nu(\mathbf{r}), \tag{73}$$

where $\mathbf{P}^{\mu\nu}$ is the density matrix. In the plane wave basis, the density can be also expanded as

$$\tilde{\rho}(\mathbf{r}) = \frac{1}{\Omega} \sum_{|\mathbf{G}|<G_C} \tilde{\rho}(\mathbf{G}) \mathrm{e}^{i\mathbf{G}\cdot\mathbf{r}}, \tag{74}$$

where Ω is the volume of the unit cell. The selection of plane waves is determined by a kinetic energy cutoff $E_C = \frac{1}{2}G_C^2$, which accounts for the number of plane wave vectors in the reciprocal grid. The difference $|\rho(\mathbf{r}) - \tilde{\rho}(\mathbf{r})|$ goes to zero on a regular (*i.e.* real space) grid as the cutoff energy E_C goes to infinity. This in turn allows a rapid conversion between $\tilde{\rho}(\mathbf{r})$, $\rho(\mathbf{r})$ and $\tilde{\rho}(\mathbf{G})$ using fast Fourier transforms (FFT).[126,127]

This dual representation of the electron density can be used to re-define the Kohn-Sham DFT energy expression within the GPW framework as:

$$\begin{aligned} E[\rho] &= E^T[\rho] + E^V[\rho] + E^H[\rho] + E^{XC}[\rho] + E^{II}[\rho] \\ &= \sum_{\mu\nu} \mathbf{P}^{\mu\nu} \langle \psi_\mu(\mathbf{r}) | -\frac{1}{2}\nabla^2 | \psi_\nu(\mathbf{r}) \rangle \\ &+ \sum_{\mu\nu} \mathbf{P}^{\mu\nu} \langle \psi_\mu(\mathbf{r}) | V_{loc}^{PP}(\mathbf{r}) | \psi_\nu(\mathbf{r}) \rangle + \sum_{\mu\nu} \mathbf{P}^{\mu\nu} \langle \psi_\mu(\mathbf{r}) | V_{nloc}^{PP}(\mathbf{r}, \mathbf{r}') | \psi_\nu(\mathbf{r}') \rangle \\ &+ 2\pi\Omega \sum_{|\mathbf{G}|<G_C} \frac{\tilde{\rho}^*(\mathbf{G})\tilde{\rho}(\mathbf{G})}{\mathbf{G}^2} + \int \epsilon_{XC}(\mathbf{r})\, \mathrm{d}\mathbf{r} + \sum_{A<B} \frac{Z_A Z_B}{|R_A - R_B|} \end{aligned} \tag{75}$$

where $E^T[\rho]$ is the electronic kinetic energy, $E^V[\rho]$ the electronic interaction with the ionic cores, $E^H[\rho]$ the Hartree energy, $E_{XC}[\rho]$ the exchange correlation energy, and $E^{II}[\rho]$

the electrostatic interaction of the ionic cores. Note that $E^V[\rho]$ is described by norm-conserving pseudo potentials which are split into a local and a non-local part. Here, the kinetic energy is computed analytically with a Gaussian basis set in real space. The second and third term in Eq. 75 arises from replacement of electrons in core orbitals by pseudopotentials in order to avoid the costly auxiliary expansion of these orbitals. On the other hand, all terms of the electrostatic energy (the Hartree energy, local pseudopotential term, and the interactions between the ionic cores), are treated using the Ewald sum method.[71]

The major advantage of employing the GPW scheme becomes clear, when the real space grids are associated with a plane wave basis set to compute the Hartree and exchange-correlation terms.[126,127] Even though, the core electrons are described by pseudopotentials, the computational advantage of the GPW method is lost in the calculation of the wave function based (exact) exchange functional.[128] Therefore, the use of hybrid functionals is not yet common in condensed phase calculations.

Summarizing, once the total energy is calculated, the forces acting on each nuclei is computed by the gradient of the energy with respect to the nuclei positions.

2.11 Time-dependent density functional theory

Time-dependent density functional theory (TD-DFT) extends the basic ideas of ground-state DFT for the treatment of the excited electronic states. In particular, it describes the interaction of an arbitrary system with a time-dependent external potential. A generalized formalism for such time-dependent systems is introduced by Runge and Gross by recalling the Hohenberg-Kohn theorems.[129,130] The Runge-Gross theorem proves that a one-to-one map exists between the time-dependent external potential $v(\mathbf{r},t)$, and the time-dependent electron density $\rho(\mathbf{r},t)$, as well as the time-dependent total electronic wave function: $v(\mathbf{r},t) \leftrightarrow \rho(\mathbf{r},t) \leftrightarrow \Psi(\mathbf{r},\mathbf{t})$.

Just like in the ground state, we can consider a system of non-interacting electrons with the same density as the fully interacting system under the influence of the local potential $v_s(\mathbf{r},t)$. Then, we can write down the time-dependent analog of the Kohn-Sham equations,

$$\left(\frac{1}{2}\nabla^2 + v_s(\mathbf{r},t)\right)\psi_i(\mathbf{r},t) = i\frac{\partial}{\partial t}\psi_i(\mathbf{r},t), \tag{76}$$

and yield

$$\rho(\mathbf{r},t) = \sum_i |\psi_i(\mathbf{r},t)|^2. \tag{77}$$

The time-dependent single particle Kohn-Sham potential is then written as

$$v_s(\mathbf{r},t) = v_{ext}(\mathbf{r},t) + \int \frac{\rho(\mathbf{r}',t)}{|\mathbf{r}-\mathbf{r}'|}d\mathbf{r}' + v_{XC}(\mathbf{r},t), \tag{78}$$

where the leading term is the external time-dependent field, the second term is the Hartree potential, and the last term is the unknown exchange-correlation potential. Since $v_s(\mathbf{r},t)$ depends on $\rho(\mathbf{r},t)$, a self-consistent procedure needs to be used to solve the time-dependent Kohn-Sham equations. In many cases, the effect of time-dependent external

field on the system is sufficiently small in the sense that it does not disrupt completely the ground state system's structure. This allows for determination of the properties like excitation energies and polarizabilities of the system from the framework of linear response theory, rather than explicitly solving iteratively the time-dependent Kohn-Sham equations. In the next section, we will derive the basic equations of the linear-response TD-DFT method, which is employed for benchmark calculations in this thesis.

2.11.1 Linear response time-dependent density functional theory

Here, we assume that the time-dependent external potential acting on a system is small, and induces a time-dependent change in the electron density of the system.[131] At $t \leq t_0$, the system is subject to the potential $v_0(\mathbf{r})$ imposed by the nuclei in the ground state, and the corresponding electron density is $\rho_0(\mathbf{r})$. Then, the time-dependent perturbation potential $v_1(\mathbf{r}, t)$ to the system is introduced at $t > t_0$, leading to a total external potential $v_{ext}(\mathbf{r}, t) = v_0(\mathbf{r}) + v_1(\mathbf{r}, t)$. Clearly, $v_1(\mathbf{r}, t)$ will induce a change in the electron density.

We can expand the electron density in a perturbative series via Taylor expansion as

$$\rho(\mathbf{r}, t) = \rho_0(\mathbf{r}) + \rho_1(\mathbf{r}, t) + \rho_2(\mathbf{r}, t) + ..., \tag{79}$$

where $\rho_1(\mathbf{r}, t)$ is the first order component of $\rho(\mathbf{r}, t)$ that depends linearly on $v_1(\mathbf{r}, t)$, $\rho_2(\mathbf{r}, t)$ is the second order term that depends quadratically, etc. In linear response regime, only the first order term in the density perturbation is considered, which has a form as

$$\rho_1(\mathbf{r}, t) = \int dt' \int \chi(\mathbf{r}t, \mathbf{r}'t') v_1(\mathbf{r}, t') d\mathbf{r}'. \tag{80}$$

In Eq. 80, $\chi(\mathbf{r}t, \mathbf{r}'t')$ is the so-called the density response function defined as

$$\chi(\mathbf{r}t, \mathbf{r}'t')\delta v_1(\mathbf{r}', \mathbf{t}) d\mathbf{r}' = \frac{\delta\rho(\mathbf{r}, t)}{\delta v_1(\mathbf{r}', t')}. \tag{81}$$

By recalling the time-dependent Kohn-Sham framework, the density of interacting electrons can be derived from a fictitious system of non-interacting electrons. Consequently, the linear change in electron density reads

$$\rho_1(\mathbf{r}, t) = \int dt' \int \chi_s(\mathbf{r}t, \mathbf{r}'t')\delta v_{s,1}(\mathbf{r}, t') d\mathbf{r}', \tag{82}$$

where $\chi_s(\mathbf{r}t, \mathbf{r}'t')$ is the density response function of a system of non-interacting electrons, $v_{s,1}(\mathbf{r}, t')$ is the linearized effective time-dependent potential acting on the fictitious system. Consequently, in terms of the frequency dependent, unperturbed stationary Kohn-Sham orbitals, the response density is written as

$$\chi_s(\mathbf{r}, \mathbf{r}'; w) = \lim_{\eta \to 0^+} \sum_{i,k=1}^{\infty} (f_k - f_i) \frac{\psi_i(\mathbf{r})\psi_k^*(\mathbf{r})\psi_i^*(\mathbf{r}')\psi_k(\mathbf{r}')}{w - (\epsilon_i - \epsilon_k) + i\eta}, \tag{83}$$

where f_i and f_k are the occupation factors (1 for occupied and 0 for the unoccupied orbitals) of the Kohn-Sham ground state orbitals $\psi_{i,k}(\mathbf{r})$, $\epsilon_{i,k}$ are the energies, η is a positive infinitesimal, and w is the frequency of the external perturbation field.

Obviously, to compute the response density (Eq. 82), the first order variation of the time-dependent Kohn-Sham potential is given as

$$v_s(\mathbf{r},t) = v_1(\mathbf{r},t) + v_{H,1}(\mathbf{r},t) + v_{XC,1}(\mathbf{r},t). \tag{84}$$

The variation of the external potential is simply v_1, while the change in the Hartree potential is

$$v_{H,1}(\mathbf{r},t) = \int \frac{\rho_1(\mathbf{r}',t)}{|\mathbf{r}-\mathbf{r}'|} d\mathbf{r}'. \tag{85}$$

Finally, the variation of the exchange-correlation functional is defined as the functional derivative of the $v_{XC}[\rho]$ with respect to the ground state density as

$$v_{XC,1}(\mathbf{r},t) = \int dt' \int \frac{\delta v_{XC}(\mathbf{r},t)}{\delta\rho(\mathbf{r}',t')} \rho_1(\mathbf{r}',t') d\mathbf{r}', \tag{86}$$

where the exchange-correlation kernel is introduced as

$$f_{XC}(\mathbf{r}t,\mathbf{r}'t') = \frac{\delta v_{XC}(\mathbf{r},t)}{\delta\rho(\mathbf{r}',t')}. \tag{87}$$

The f_{XC} is a very complex quantity and the exact form of it is unknown and has to be approximated. Many approximate f_{XC} can be found in literature. The simplest one is the so-called "Adiabatic LDA (ALDA) kernel" .[132] The term adiabatic derives from the assumption that the electron density of the system readjusts instantaneously to a variation in the external field, thus reducing the kernel dependency only to local density and time.

2.12 Density functional perturbation theory

In general, when a perturbation field is applied to a system at equilibrium, many interesting properties (response functions) of the system that is coupled to the perturbation field, change accordingly. Response functions are second, third, or higher order derivatives of the total energy with respect to applied perturbation fields. For example, polarizabilities, NMR chemical shifts and IR-spectra are second order properties *i.e.* can be computed from second order derivatives. Within the concept of density functional perturbation theory (DFPT), the properties of the electronic structure are computed via variational principle. [133–136] The formulation of this discussion closely follows the Ref.[136].

The standard perturbation theory starts by the identification of a scaling parameter, $\lambda << 1$, characterizing the change in the unperturbed Hamiltonian $\hat{H}_0$ of the system due to the perturbation Hamiltonian $\hat{H}_1$. Then, we can define the total Hamiltonian of the system according to

$$\hat{H} = \hat{H}_0 + \lambda\hat{H}_1. \tag{88}$$

Consequently, such a perturbation to the system will change the energies and wave functions of the system, which can be written in a power series in λ as:

$$E = E^{(0)} + \lambda E^{(1)} + \lambda^2 E^{(2)} + ... + \lambda^n E^{(n)}, \tag{89}$$

and

$$|\psi\rangle = |\psi^{(0)}\rangle + \lambda|\psi^{(1)}\rangle + \lambda^2|\psi^{(2)}\rangle + ... + \lambda^n|\psi^{(n)}\rangle. \tag{90}$$

Here, the assumption is that the perturbation is sufficiently small, *i.e.* in low orders of λ (in the linear response regime). Thus, the response of any property represented by an observable X can be obtained by a perturbative expansion around its unperturbed value X^0 as:[136]

$$X^{(n)} = \frac{1}{n!}\frac{d^n X}{d\lambda^n}. \tag{91}$$

In the usual formulation of DFPT, X can be energy E, density $\rho(\mathbf{r})$, or the Kohn-Sham orbitals ψ_i. Accordingly, the total electronic energy $E^{tot}[\psi_i]$ of the system under a weak perturbation is redefined as

$$E^{tot}[\psi_i] = E_{KS}[\psi_i] + \lambda E_{KS}^{pert}[\psi_i], \tag{92}$$

where $E_{KS}[\psi_i]$, and $E_{KS}^{pert}[\psi_i]$ are the unperturbed Kohn-Sham energy, and the linearized perturbation energy term, respectively. Eq. 92 can be solved with the standard ground state variational approach. Minimizing the E^{tot} expression for a small perturbation parameter λ is possible by the *finite-difference* approach. However, this method shows dependencies on the choice of the λ. Instead, the alternative way is an analytical separation of the different orders of the perturbation and their explicit calculation via DFPT. In order to do this, the total Kohn-Sham energy in the presence of the small perturbation is minimized with respect to the Kohn-Sham wave functions. This reformulation of the perturbation theory in terms of variations of wave functions is known as the Sternheimer linear response.[137] This follows from the fact that in an expansion:

$$E_{KS}^{tot} = E_{KS}^{tot}[\psi_i^{(0)} + \lambda\psi_i^{(1)} + ...] = E^{(0)} + \lambda E^{(1)} + \lambda^2 E^{(2)} + ... \tag{93}$$

It should be noted here that the linear order energy term vanishes in Eq. 93 due to the stationarity of the $\psi_i^{(0)}$. Therefore, the first non-vanishing term is the second order energy $E^{(2)}$. This yields the following stationarity condition:

$$\frac{\delta E^{tot}}{\delta\psi_i^{(1)}} = 0. \tag{94}$$

A variational expression to the second order energy term $E^{(2)}$ can be obtained with respect to the $\psi_i^{(1)}$ under the constraint, which is the orthonormality of the total states $\langle\psi_i^{(1)}|\psi_{i'}^{(0)}\rangle = 0$ for all occupied states i and all i'. This results in the following expression for the second order energy term:

$$\begin{aligned} E^{(2)} &= \sum_i \left[\langle\psi_i^{(1)}|\hat{H}_{KS}^{(0)} - \epsilon_i^0|\psi_{i'}^{(1)}\rangle\right] + \frac{1}{2}\iint d^3r\, d^3r' f_{HXC}(\mathbf{r},\mathbf{r}')\rho^{(1)}(\mathbf{r})\rho^{(1)}(\mathbf{r}') \\ &+ \sum_i \left[\langle\psi_i^{(1)}|\frac{\delta E^{pert}}{\delta\langle\psi_i^{(0)}|} + \frac{\delta E^{pert}}{\delta|\psi_{i'}^{(0)}\rangle}|\psi_i^{(1)}\rangle\right], \end{aligned} \tag{95}$$

where f_{HXC} is the Hartree-exchange-correlation kernel defined as

$$f_{HXC}(\mathbf{r},\mathbf{r}') = \frac{\delta(E_H + E_{XC})}{\delta\rho(\mathbf{r})\delta\rho(\mathbf{r}')}. \tag{96}$$

Eq. 95 indicates that the second order derivatives of the total energy can completely determined by the first order derivatives of the wave function. By rearranging Eq. 95 and Eq. 93, we obtain the Sternheimer equation[137], which can be also written in terms of the projector operator $\mathbf{P}_e = \sum_i \mathbf{1} - |\psi_i^0\rangle\langle\psi_i^0|$:

$$-\mathbf{P}_e(\hat{H}^0_{KS} - \epsilon_i^{(0)})\mathbf{P}_e|\psi_i^{(1)}\rangle = \mathbf{P}_e\left[\int d^3r' f(\mathbf{r},\mathbf{r}')\rho^{(1)}(\mathbf{r}')|\psi_i^{(0)}\rangle + \frac{\delta E^{pert}_{KS}}{\delta\langle\psi_i^{(0)}|}\right]. \tag{97}$$

Since the second order energy term $E^{(2)}$ is calculated via a variational scheme, Eq. 97 can be solved self-consistently. With this result, it is possible to calculate the response properties of various perturbations such as nuclear displacements or electronic, and magnetic fields.

2.12.1 Basic theory of magnetic resonance

Nuclear magnetic resonance spectroscopy (NMR) is a commonly used experimental tool to analyze various structural and dynamic properties of systems.[138,139]

The NMR chemical shifts depend on the local chemical environment of the nuclei and are therefore intrinsically connected to the local electronic structure. The Hamiltonian describing the interaction between the magnetic moment $\boldsymbol{\mu}_I$ with a static magnetic field $\mathbf{B}^0$ given by

$$\hat{\mathbf{H}} = -\boldsymbol{\mu}_I \cdot \mathbf{B}^0. \tag{98}$$

Then, the eigenvalues of Eq. 98 in SI units can be written as

$$E = -\gamma m\hbar B^0, \tag{99}$$

with the gyromagnetic ratio γ. The total magnetic field $\mathbf{B}^{tot}(\mathbf{r})$ is given by

$$\mathbf{B}^{tot}(\mathbf{r}) = \mathbf{B}^0 + \mathbf{B}^{ind}(\mathbf{r})\,, \tag{100}$$

where $\mathbf{B}^0$ and $\mathbf{B}^{ind}(\mathbf{r})$ are the external field and the corresponding induced field modifying the total field acting on the nuclei, respectively.

The external magnetic field does not appear directly in the electronic Hamiltonian, but instead, its representation by the magnetic vector potential $\mathbf{A}(\mathbf{r})$ via $\mathbf{B}^0(\mathbf{r}) = \nabla \times \mathbf{A}(\mathbf{r})$. To include its presence into the electronic Hamiltonian, the usual momentum operator $\hat{\mathbf{p}}$ has to be replaced by the canonical momentum

$$\hat{\pi} = \hat{\mathbf{p}} - q/c\mathbf{A}(\mathbf{r}), \tag{101}$$

where q is the charge, and, c the speed of light. Thus, we can define the first-order perturbation Hamiltonian as

$$\hat{\mathscr{H}}_1 = -\hat{\mathbf{p}} \cdot \mathbf{A}(\mathbf{r}). \tag{102}$$

Accordingly, this yields the total Hamilton as

$$\begin{aligned}\hat{\mathscr{H}} &= \frac{1}{2}(\hat{\mathbf{p}} - \frac{q}{c}\mathbf{A}(\mathbf{r}))^2 + v(\mathbf{r}) \\ &= \frac{1}{2}\hat{\mathbf{p}}^2 - \frac{q}{2c}(\hat{\mathbf{p}}\cdot\mathbf{A}(\mathbf{r}) + \mathbf{A}(\mathbf{r})\cdot\hat{\mathbf{p}}) + v(\mathbf{r}) + \frac{q^2}{2c^2}A^2. \end{aligned} \tag{103}$$

In Eq. 103, the magnetic vector potential $\mathbf{A}(\mathbf{r})$ of a homogeneous magnetic field is then given by

$$\mathbf{A}(\mathbf{r}) = -\frac{1}{2}\mathbf{r}\times\mathbf{B}^0, \tag{104}$$

and found to be commuting with the usual momentum operator $\hat{\mathbf{p}}$. This is a particular choice of gauge, the so-called "classical Coulomb gauge", to simplify the derivation, and it should normally not affect the values of observable quantities. However, this is only guaranteed in the limit of using a complete basis set, which will be discussed later on.

Back on the derivation, by adding this first order perturbation into Eq. 97 the Sternheimer equation is obtained:

$$-\mathbf{P}_e(\hat{H}^0_{KS} - \epsilon_i^{(0)})\mathbf{P}_e|\psi_i^{(1)}\rangle = \mathbf{P}_e\mathbf{r}\times\mathbf{p}|\psi_i^{(0)}\rangle. \tag{105}$$

Note that, the perturbation parameter here is the homogeneous external magnetic field. Therefore, three different perturbations for all directions are needed. Furthermore, the calculation of the perturbed Kohn-Sham states is simplified due to the nature of this particular perturbation *i.e.* $\mathbf{r}\times\mathbf{p}$ is a Hermitian conjugate and purely imaginary.[140] So one finds that the linear order components of the density response terms must vanish analytically, thus no self-consistent solution is required. As a consequence, it is possible to calculate the induced electronic flow

$$\mathbf{j}(\mathbf{r}) = \frac{1}{2}\sum_i f_i\left[\psi_i^{(1)*}\nabla\psi_i^{(0)} + \psi_i^{(0)*}\nabla\psi_i^{(1)}\right](\mathbf{r}) + \rho(\mathbf{r})\mathbf{A}(\mathbf{r}). \tag{106}$$

The induced magnetic field at the nuclei can be obtained according to the law of Biot-Savard as

$$\mathbf{B}^{ind}(\mathbf{r}) = \frac{1}{c}\int d^3r'\frac{\mathbf{r}'-\mathbf{r}}{|\mathbf{r}'-\mathbf{r}|^3}\times\mathbf{j}(\mathbf{r}'). \tag{107}$$

The nuclear shielding tensor for a nuclei at $\mathbf{R}_n$ is defined by

$$\sigma_{ij}(\mathbf{R}_n) = -\frac{\partial B_i^{ind}(\mathbf{R}_n)}{\partial B_j^0}. \tag{108}$$

Normally, a molecule can orient in many directions with respect to the external magnetic field. Therefore, only the isotropic part of the chemical shielding tensor is considered in this work, which can be calculated by averaging the trace of the corresponding shielding tensor as

$$\sigma_{iso} = \frac{1}{3}Tr(\sigma). \tag{109}$$

The gauge origin problem

The main problem calculating the nuclear shielding tensor within the concept of density functional perturbation theory, is the so-called gauge origin problem. As seen from Eq. 104, the magnetic field is represented by a vector field $\mathbf{B}(\mathbf{r}) = \nabla \times \mathbf{A}(\mathbf{r})$. This vector potential is not unique, since we may choose its position in the gauge origin freely, and derive the magnetic field accordingly. A general gauge transformation of the vector potential can be defined as

$$\mathbf{A}(\mathbf{r}) \rightarrow \mathbf{A'}(\mathbf{r}) = \mathbf{A}(\mathbf{r}) + \nabla\psi(\mathbf{r}), \tag{110}$$

where $\psi(\mathbf{r})$ is an arbitrary scalar function. In principle, this choice of gauge origin should not change the magnetic filed, and thus, this degree of freedom is called gauge invariance. For example, one can choose the particular gauge transformation associated with an arbitrary shift from $\mathbf{r}$ to $\mathbf{r} + \mathbf{R}_i$. For such a transformation, the scalar function can be defined as

$$\Theta(\mathbf{r}) = \frac{1}{2}\mathbf{B} \times \mathbf{r} \cdot \mathbf{R}_o. \tag{111}$$

As seen in Eq. 111, the gauge transformation only changes the origin of the coordinate system, therefore the magnetic field cannot depend on that. However, the gauge invariance is found to be lost in the numerical calculations of the induced current $\mathbf{J}(\mathbf{r})$, based on atomic orbitals. This problem originates from using a finite basis set or non-local pseudopotentials to represent the molecular orbitals. A trivial solution to this problem would be using a very large basis sets in order to minimize this error. Unfortunately, working with a large basis set is not always an option due to impracticable computational costs. Several approaches have been developed to tackle this problem in literature. One of the oldest method is to employ "gauge-including atomic orbitals"(GIAOs) [141] as a basis set which incorporates the positions of each nuclei into the gauge origin for all orbitals. Another very popular method is the ïndividual gauge for localized orbitals"(IGLO) [142], where the center of charge of the molecular orbitals is chosen as a gauge origin. Alternatively, the "continuous set of gauge transformations"(CSGT) method [143] defines a gauge which is dependent on the position where the induced current would be calculated.

2.12.2 Basic theory of infrared spectroscopy

Another spectroscopic tool in the determination of dynamical properties of complex systems involves absorption of infrared radiation with frequencies between 4000 and 400 cm^{-1}.[144] Many important properties of the dynamics of molecular system in particular in aqueous solution can be probed from mid-infrared (IR) spectra.

As discussed previously, within the linear response theory, the IR spectrum can be defined by the autocorrelation functions of the dipole moments, whose Fourier transform is related to the product of absorption coefficients, *i.e.* the IR spectrum as:[145]

$$\alpha(\omega)n(\omega) = F(\omega)\int_{-\infty}^{\infty} dt\langle\mu(0)|\mu(t)\rangle e^{-i\omega t}\,, \tag{112}$$

where $F(\omega)$) is sometimes called the harmonic quantum correction factor, which ensures the correct symmetry, and μ is the total dipole moment of the molecular system.[146] The total dipole moment is decomposed into nuclear and electronic parts according to

$$\mu = \mu^{nuclei} + \mu^{elec}. \tag{113}$$

In the Born-Oppenheimer picture, the nuclei is considered as a classical particle, so the nuclear contribution can be calculated from the particle positions. However, the electronic dipole moment requires a subtle treatment, and is available in any electronic structure calculation. Generally, the electronic dipole moment is computed via the localized Wannier functions which are produced by a unitary transformation of the Kohn-Sham orbitals.[147–149] Thus, when the center of Wannier orbitals are assigned to the individual molecules, the molecular dipole moment can be calculated via Eq. 112. There is extensive literature about the protocol of computation of IR absorption, and can be found in Refs.[150–152]

3 Overview over the published papers

3.1 Water mediated proton transfer processes

From a computational perspective, the main goal was to give an atomistic understanding of picosecond time evolution of hydrogen bonding interactions and proton dissociation mechanisms in aqueous solutions. We performed numerical simulations in order to elucidate the relationships between local hydrogen bonding structure and picosecond protonation dynamics, and spectroscopic observables. Proton dissociation reactions are regarded as a very complex chemical reaction due to the involvement of bond-breaking and bond-forming processes.[45,153–161] These phenomenons require an accurate description of the picosecond time evolution of hydrogen bonding interactions at ambient conditions. Hence, *ab initio* molecular dynamics simulations are best-suited to address the challenges associated to the underlying mechanisms and the time scales of these aqueous proton transport mechanisms.

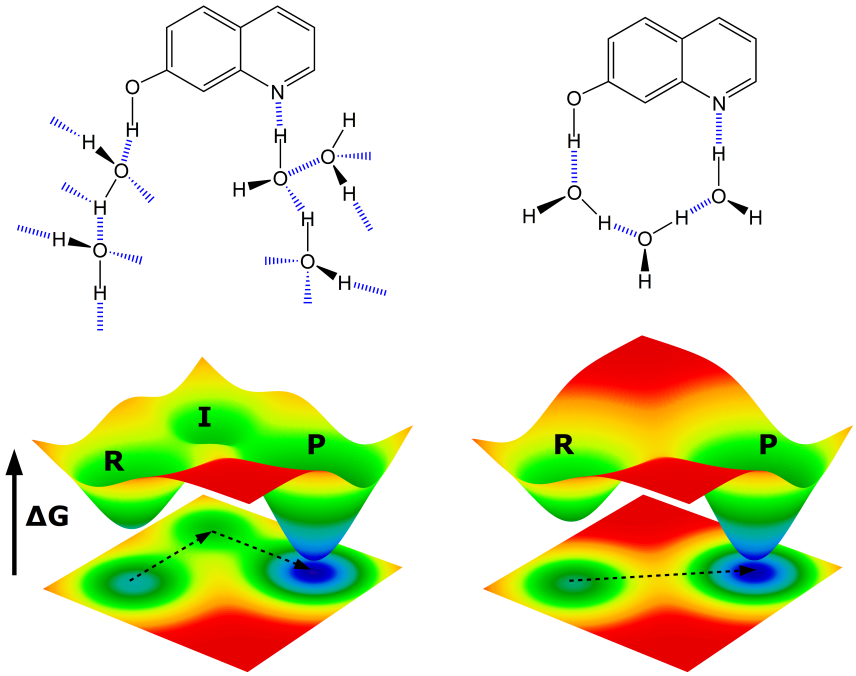

Figure 4: Possible solute-solvent interactions between 7HQ and water molecules. Independent water molecules hydrating donor/acceptor sites are on the left side while the water wire bridging the donor/accpetor sites is on the right side. A correlation between the microscopic solvation configurations and reaction profiles is illustrated in order to discriminate *concerted* (without a stable intermediate, on the right side) and sequential proton transfer mechanisms (on the left side).[35]

In this part of the project, we focused on investigating proton dissociation processes initiated by electronic excitation of a photoacid/-base resulting in an increase of its

acidic and base properties.[36,162] In particular, we studied a bifunctional chromophore, 7-Hydroxyquinoline (7HQ), which has a well-defined location of proton donating (acid) and proton accepting (base) groups, between which proton transfer (PT) would occur.[34] Firstly, we focused on understanding intramolecular electronic charge rearrangements of 7HQ, which is triggered by optical excitation and also by intermolecular interactions with the solvent. In particular, the solvent effect on the nature of the excited state PT was of interest.[34] We performed a series of structure optimizations and transition state calculations of the 7HQ molecule with a water wire of three explicit molecules, complemented by an additional implicit solvation scheme. Here, water wire can be understood as a specific solvent switch having the ability of efficiently assisting proton transfer reactions by connecting acid and base groups. We elucidated the energy profile of the reaction paths of the commonly argued PT mechanisms, which occur via release of a proton from the 7HQ to a water wire and eventually the back-donation of the proton to the nitrogen site of 7HQ. In particular, we have been able to probe *concerted*, *i.e.* without stable intermediates, proton transfer reactions between acid/base terminals via water wires.

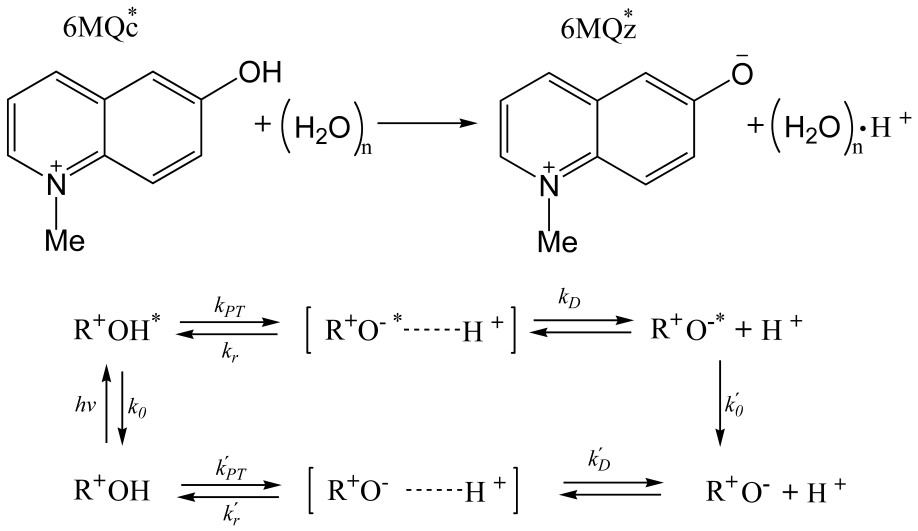

Figure 5: Excited state proton transfer and relaxation processes of excited N-methyl-6-hydroxyquinolinium species.[43]

On the other hand, the discrimination of the different topologies of solvation around the photosensitive chromophores requires an explicit solvation description with an accurate quantum mechanical treatment. In order to provide more realistic solvation conditions, the focus was on characterization of the picosecond time evolution of complex hydrogen-bonding interactions between the chromophore and the surrounding water at ambient conditions.[35] This work can be viewed as a continuation of the previous work on 7HQ with a short water wire.[34] Therefore, we performed *ab initio* molecular dynamics simulations of a specific set of HQ derivatives as probe molecules by means of their photoinduced acid/base functionalities. We analyzed this aspect by determining the time evolution of the water wires between polar sites of the probe molecules. In particular, formation of water wires with an optimal configuration can be understood as prior to a

concerted PT process leading to an ultrafast proton transfer on a time scale of femtosecond range (see Figure 4). Therefore, we compared the lifetime of water wires in bulk water and water wires of the same length connecting the donor and acceptor sites of HQs. The analysis showed that the dynamics of bulk water wires substantially differs from the dynamics of water wires connecting the acidic and basic sites. Furthermore, the following correlation was found: the shorter water wire length is the higher is the persistency. This finding then lead us to conclude that the internal hydrophobic interface around the aromatic ring of HQs can stabilize the water wires and in turn the water reorientation dynamics is retarded.

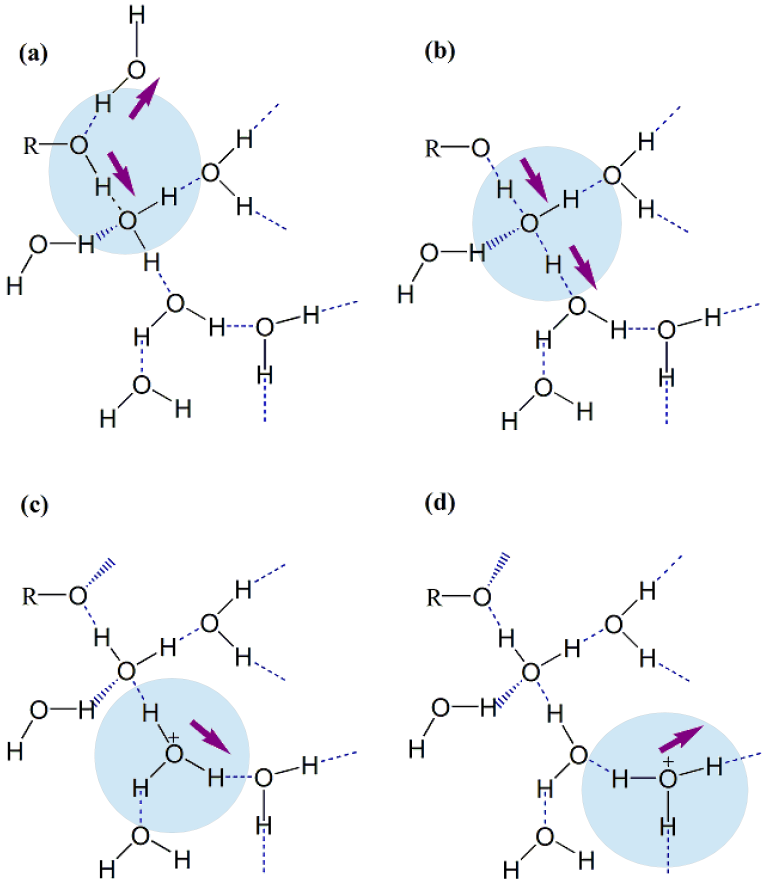

Figure 6: Scheme illustrating the proton transfer mechanisms of 6MQc* in aqueous solution. (a) Formation of contact ion pair and elongation of hydrogen bond between 6MQc-oxygen atom and water molecule; (b) transient structures involving the concerted motion of two protons; (c) and (d) a threefold coordinated water molecule holding the excess proton.[43]

In the final part of this project, we investigated the proton dissociation steps, and structural changes of solvent molecules around the acidic proton triggered by photoexcitation.[43] Here, the aim was to elucidate intramolecular charge rearrangements, and the following proton dissociation mechanisms, the role, coordination, and dynamics of the surrounding water molecules, and how they interplay with the proton dissociation

mechanisms. A suitable molecule for this purpose was the super photoacid N-methyl-6-hydroxyquinolinium cation (6MQc) depicted in Figure 5. After equilibration in the electronic ground state, we put the 6MQc in the triplet state (T_1) for the simulation of the excited-state dynamics, *i.e.* the first excited state (S_1) was approximated with a T_1 surface. With the DFT T_1 description, it was possible to represent the most significant physical intramolecular interactions.

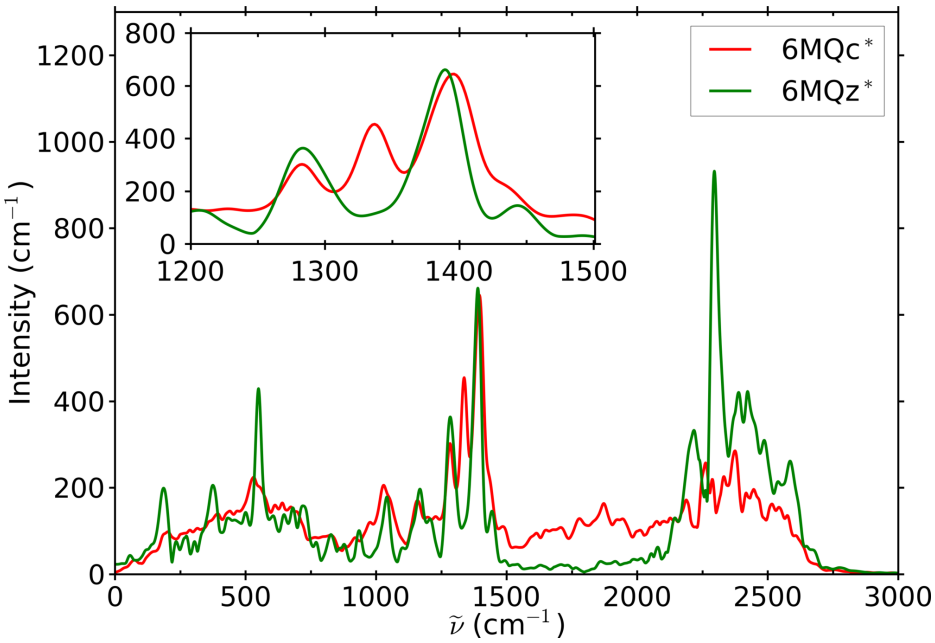

Figure 7: Infrared spectrum of 6MQc* and the final product 6MQz* averaged over *ab initio* trajectories.[43]

In order to elucidate structural alternations of solvent molecules, a consequence of the response of the water molecules to the charge rearrangements of the probe molecule after electronic excitation, we computed several spatial distribution functions before and after the acidic proton is transferred from the 6MQc to a water molecule. These findings showed that the rate-limiting step for the PT to the first solvent molecule is not the initial acid-water barrier, but instead the solvation structure around the first water molecule. We also identified the actual PT mechanisms being either concerted or sequential in the bulk solution. The analysis showed that the concerted PT occurs if the proton accepting water molecule is fourfold coordinated. In contrast, the step-wise PT transfer was found to happen in the case of only threefold coordination (see Figure 6).

The individual steps of the elementary proton transfer process (proton dissociation to the water molecule) result in characteristic fingerprints in the time-resolved infrared absorption frequencies that can be measured via a probe pulse in the femtosecond to picosecond time range. On the theoretical side, the same infrared fingerprints can be computed by means of *ab initio* molecular dynamics simulations. In order to elucidate the effects of the change in the charge distributions of the chromophore, and proton dissociation processes, we calculated IR absorption spectra of the 6MQc in the ground and triplet excited states (see Figure 7). A broad IR absorption line from 1500cm^{-1} to

2000cm^{-1} was identified after excitation and before deprotonation of the acid due to the loose bonding situation of the acidic proton just before dissociation.

3.2 Structural and spectroscopic response to ions

The structural and dynamical properties of aqueous solvation can be investigated in terms of the water's complex hydrogen bonded network. Addition of ions has tremendous effects on the characteristics of the hydrogen bonds. Within this part of the thesis, it was particularly compelling to analyze to what extend the hydrogen bonding network is modified by the presence of either kosmotropic or chaotropic ions at intermediate of 2M concentration.[50] For instance, chaotropic ions weaken the H-bonding network, and therefore facilitate dissolving of unpolar substances, whereas kosmotropic ions have the opposite effect. Influence of solvated ions on the structure and dynamics of liquid water requires a proper representation of the electronic effects such as ion and water polarization. The choice of the computational method therefore is crucial for elucidation of such electronic interactions for correct modeling of ion-water interactions. In these studies, *ab initio* molecular dynamics simulations have been employed due to the inherent advantage of containing all the information about the bonding and polarization fluctuations.

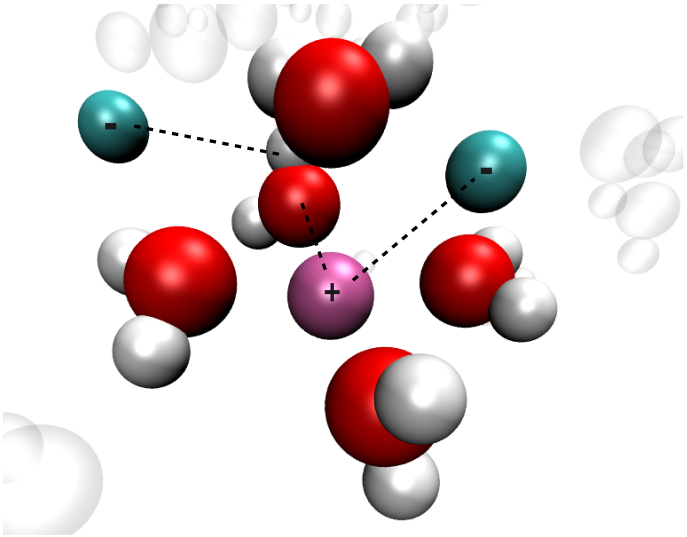

Figure 8: Formation of solvent shared and direct ion pairs.

In this work, a series of divalent ion solutions ($MgCl_2$, $CaCl_2$, MgI_2, and CaI_2) was referenced to provide clear information about structure and dynamics of the ion surrounding by means of *ab initio* molecular dynamics and theoretical and experimental NMR chemical shift measurements. In general terms, ^{1}H NMR chemical spectroscopy is a very sensitive probe of the nature of hydrogen bonds, and used to reveal a deeper understanding of structure-property relationships in terms of subtle changes in the hydrogen bonding network due the hydration phenomena of solvated ions. Therefore, instantaneous ^{1}H NMR chemical shifts from first principle calculations were conducted, and decomposed into contributions from the first solvation shell of the individual ions.

These contributions confirmed the kosmotropic/chaotropic nature of ions on the local hydrogen bond structure. Furthermore, the overall agreement between computed ^{1}H NMR chemical shifts and experimental values was found be fairly good (see Figure 9).

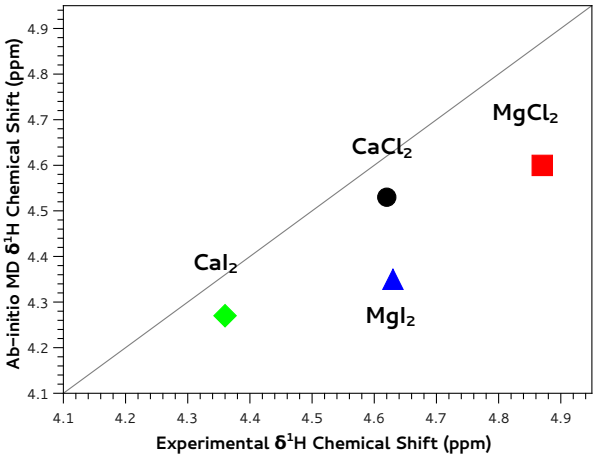

Figure 9: ^{1}H NMR chemical shifts for $CaCl_2$, $MgCl_2$, CaI_2, and MgI_2 at 2M concentration. Calculated NMR shifts are referenced to the H_2O trajectory which in turn is set to the experimental shift of 4.65 ppm. The linear line is meant as a guide to the eye.

Besides the structural aspects, the dynamical changes of hydrogen bonding induced by solvated ions were quantified by suitable autocorrelation functions. These findings showed that the impact of ions on water dynamics depends not only on the size and charge of the ions, but also strongly on the existence and stability of the solvent (water)-shared ion pairs. In particular, the first solvation shells of divalent ions were found to be overlapped by forcing the formation of the water-shared ion pairs at 2M concentration (see Figure 8). The simulations showed that these transient water-shared ion pairs were accompanied by restrictions on the mobility of the shared water molecules.

4 Conclusion

A number of theoretical studies have been performed in this thesis in the framework of aqueous hydrogen bond networks in condensed systems, with a particular focus on proton dissociation reactions on fast timescales and characterization of the kosmotropic/chaotropic nature of ions. By means of *ab initio* molecular dynamics simulations, the equations of motions of all involved atoms are integrated, and structural and dynamical properties as well as spectroscopic features are extracted from the trajectories. The use of quantum chemical calculations for all atomic forces allows the automatic incorporation of all relevant interatomic and intermolecular interactions. The combination of electronic structure theory and explicit molecular dynamics yields a realistic representation of the molecular environment of the hydrogen bond networks and an accurate modeling of ambient conditions.

In the first part of this thesis, the aim was to develop a detailed understanding of the role water plays in proton transfer processes between specific photoacid/-base moieties along the (persistent) extended hydrogen bonded chains (water wires). We chose particular model systems from the hydroxyquinoline family (6- and 7HQ), which contain well-defined locations of hydrogen bond donor and acceptor sites, in which proton transfer reactions can be propagated. The main focus was to discriminate different topologies of solvation *i.e.* "short" and "long" water wires connecting these functional sites. Therefore, the existence and persistence of water wires on the picosecond timescale was characterized in relation to the numbers and lifetimes of the involved hydrogen bonds, and compared with bulk situations. It was found that the lifetime of water wires between the acidic and basic sites of chromophores was different from the bulk water wires. The simulations showed that the persistent (picosecond time scale) water wires with an optimal configuration can be existed at the moment of excitation, and are capable of shifting the nature of the proton transfer processes (concerted/step-wise).

The second question addressed in this thesis was the direct determination of photoinduced proton dissociation processes and the role of accompanied water molecules. A suitable molecule for this purpose was the "super" photoacid N-methyl-6-hydroxyquinolinium cation (6MQc). The first excited state S_1 was approximated with a DFT T_1 surface, which was found to yield a very good accuracy, in particular regarding the hydrogen bond (strength) change around the chromophore. Therefore, the validation of this approximative *ab initio* scheme in turn allowed a considerably better statistical sampling of molecular dynamics trajectories with a reduced computational effort, which was necessary to correctly represent the structural disorder inherent to aqueous solvation. This study confirmed the previous findings on the proton transfer mechanisms in aqueous solutions, and elucidated the details of a fast structural and dynamical response of hydrogen bonded network upon charge rearrangements, triggered by photoexcitation. These intramolecular/intermolecular structural changes were found to be reflected explicitly in time-dependent *ab initio* IR spectra. The computed IR spectra showed a broad absorption line from 1500 to 2000 cm^{-1} by indicating the loose bonding situation of the acidic proton just before its dissociation.

In the final topic, attention was focused on understanding the impact of a specific combinations of cations and anions on the structure and dynamics of the water molecu-

les at intermediate of 2M concentration. A series of divalent ion solutions ($MgCl_2$, $CaCl_2$, MgI_2, and CaI_2) was investigated by means of *ab initio* molecular dynamics simulations, complemented by measurements and corresponding quantum chemical calculations of the ^{1}H NMR. The simulations demonstrated significant structural and dynamical differences in the characteristics of hydrogen bonds in the first solvation shell of ions with respect to the situation in bulk water. The influence of ions on the overall hydrogen bond dynamics was found to be ion-specific, and dependent on the existence and stability of the solvent-shared ion pairs. The simulations showed that these transient water-shared ion pairs were accompanied by restrictions on the mobility of the shared water molecules. Complementary ^{1}H NMR chemical shifts based on *ab initio* trajectories showed a good agreement with experiment.

These studies showed that *ab initio* treatment of aqueous solvation can offer accurate description of hydrogen bonding, formation and cleavage of covalent bonds (proton transfer), local water-ion interactions, and fast conformational changes upon charge rearrangements. The simulations yielded a correlation between structural configurations and spectroscopic parameters complementary to experimental data. The findings open the door for elucidating a variety of more sophisticated biological systems such as ion-induced perturbation on the peptide-peptide interactions. Furthermore, the investigation of proton dissociation mechanisms in presence of ions could yield fundamental insights in biocatalysis and in photosynthesis.

5 Literature

[1] Kühne, T. D. Second Generation Car–Parrinello Molecular Dynamics. *WIREs Comput. Mol. Sci.* **2014**, *4*, 391–406.

[2] Kühne, T. D.; Krack, M.; Mohamed, F. R.; Parrinello, M. Efficient and Accurate Car-Parrinello-like Approach to Born-Oppenheimer Molecular Dynamics. *Phys. Rev. Lett.* **2007**, *98*, 066401.

[3] Kühne, T. D.; Krack, M.; Parrinello, M. Static and Dynamical Properties of Liquid Water from First Principles by a Novel Car–Parrinello-like Approach. *J. Chem. Theory Comput.* **2009**, *5*, 235–241.

[4] Kirchner, B. Theory of Complicated Investigation of Liquids, Solvent Effects with Modern Theoretical Methods. *Phys. Rep.* **2007**, *440*, 1–111.

[5] Kirchner, B.; di Dio, P. J.; Hutter, J. In *Multiscale Molecular Methods in Applied Chemistry*; Kirchner, B., Vrabec, J., Eds.; Springer Berlin Heidelberg, 2012; Chapter Real-world Predictions from Ab Initio Molecular Dynamics Simulations, pp 109–153.

[6] Geissler, P. L.; Dellago, C.; Chandler, D.; Hutter, J.; Parrinello, M. Autoionization in Liquid Water. *Science* **2001**, *291*, 2121–2124.

[7] Vuilleumier, R.; Borgis, D. Proton Conduction: Hopping along Hydrogen Bonds. *Nat. Chem.* **2012**, *4*, 432–433.

[8] VandeVondele, J.; Borstnik, U.; Hutter, J. Linear Scaling Self-consistent Field Calculations with Millions of Atoms in the Condensed Phase. *J. Chem. Theory Comput.* **2012**, *8*, 3565–3573.

[9] Mniszewski, S. M.; Cawkwell, M. J.; Wall, M. E.; Mohd-Yusof, J.; Bock, N.; Germann, T. C.; Niklasson, A. M. N. Efficient Parallel Linear Scaling Construction of the Density Matrix for Born–Oppenheimer Molecular Dynamics. *J. Chem. Theory Comput.* **2015**, *11*, 4644–4654.

[10] Tuckerman, M. E.; Ungar, P. J.; von Rosenvinge, T.; ; Klein, M. L. Ab Initio Molecular Dynamics Simulations. *J. Phys. Chem.* **1996**, *100*, 12878–12887.

[11] Boero, M.; Terakura, K.; Ikeshoji, T.; Liew, C. C.; Parrinello, M. Hydrogen Bonding and Dipole Moment of Water at Supercritical Conditions: A First-Principles Molecular Dynamics Study. *Phys. Rev. Lett.* **2000**, *85*, 3245–3248.

[12] R. Iftimie, P. M.; Tuckerman, M. E. Ab Initio Molecular Dynamics: Concepts, Recent Developments, and Future Trends. *Proc. Natl. Acad. Sci. U.S.A.* **2005**, *102*, 6654–6659.

[13] Hutter, J.; Curioni, A. Car-Parrinello Molecular Dynamics on Massively Parallel Computers. *ChemPhysChem* **2005**, *6*, 1788–1793.

[14] Hutter, J.; Iannuzzi, M.; Schiffmann, F.; VandeVondele, J. CP2K: Atomistic Simulations of Condensed Matter Systems. *WIREs. Comput. Mol. Sci.* **2014**, *4*, 15–25.

[15] Marx, D.; Chandra, A.; Tuckerman, M. E. Aqueous Basic Solutions: Hydroxide Solvation, Structural Diffusion, and Comparison to the Hydrated Proton. *Chem. Rev.* **2010**, *110*, 2174–2216.

[16] Chandra, A.; Tuckerman, M. E.; Marx, D. Condensed Matter: Structure, etc.-Connecting Solvation Shell Structure to Proton Transport Kinetics in Hydrogen-bonded Networks via Population Correlation Functions. *Phys. Rev. Lett.* **2007**, *99*, 145901–146100.

[17] Feig, M. *Modeling Solvent Environments: Applications to Simulations of Biomolecules*; Wiley-VCH, 2010; p 368.

[18] Jimenez, R.; Fleming, G. R.; Kumar, P. V.; Maroncelli, M. Femtosecond Solvation Dynamics of Water. *Nature* **1994**, *369*, 471–473.

[19] Heyden, M.; Sun, J.; Funkner, S.; Mathias, G.; Forbert, H.; Havenith, M.; Marx, D. Dissecting the THz Spectrum of Liquid Water from First Principles via Correlations in Time and Space. *Proc. Natl. Acad. Sci. USA* **2010**, *107*, 12068–12073.

[20] Schir, G.; Fichou, Y.; Gallat, F.-X.; Wood, K.; Gabel, F.; Moulin, M.; Haertlein, M.; Heyden, M.; Colletier, J.-P.; Orecchini, A.; Paciaroni, A.; Wuttke, J.; Tobias, D. J.; Weik, M. Translational Diffusion of Hydration Water Correlates with Functional Motions in Folded and Intrinsically Disordered Proteins. *Nat. Commun.* **2015**, *6*.

[21] Franks, F. *Water: A Matrix of Life*; The Royal Society of Chemistry, Cambridge, 2000.

[22] Tuckerman, M. E.; Marx, D.; Klein, M. L.; Parrinello, M. On the Quantum Nature of the Shared Proton in Hydrogen Bonds. *Science* **1997**, *275*, 817–820.

[23] Chen, B.; Ivanov, I.; Klein, M. L.; Parrinello, M. Hydrogen Bonding in Water. *Phys. Rev. Lett.* **2003**, *91*, 215503.

[24] Kühne, T. D.; Khaliullin, R. Z. Electronic Signature of the Instantaneous Asymmetry in the First Coordination Shell of Liquid Water. *Nat. Commun.* **2013**, *4*.

[25] Kühne, T. D.; Khaliullin, R. Z. Nature of the Asymmetry in the Hydrogen-Bond Networks of Hexagonal Ice and Liquid Water. *J. Am. Chem. Soc.* **2014**, *136*, 3395–3399.

[26] Luzar, A.; Chandler, D. Hydrogen-Bond Kinetics in Liquid Water. *Nature* **1996**, *379*, 55–57.

[27] Luzar, A.; Chandler, D. Effect of Environment on Hydrogen Bond Dynamics in Liquid Water. *Phys. Rev. Lett.* **1996**, *76*, 928–931.

[28] Stirnemann, G.; Wernersson, E.; Jungwirth, P.; Laage, D. Mechanisms of Acceleration and Retardation of Water Dynamics by Ions. *J. Am. Chem. Soc.* **2013**, *135*, 11824–11831.

[29] Cowan, M. L.; Bruner, B. D.; Huse, N.; Dwyer, J. R.; Chugh, B.; Nibbering, E. T. J.; Elsaesser, T.; Miller, R. J. D. Ultrafast Memory Loss and Energy Redistribution in the Hydrogen Bond Network of Liquid H2O. *Nature* **2005**, *434*, 199–202.

[30] Dalko, P. I.; Moisan, L. In the Golden Age of Organocatalysis. *Angew. Chem. Int. Ed.* **2004**, *43*, 5138–5175.

[31] Willow, S. Y.; Salim, M. A.; Kim, K. S.; Hirata, S. Ab Initio Molecular Dynamics of Liquid Water using Embedded-fragment Second-order Many-body Perturbation Theory towards its Accurate Property Prediction. *Nature* **2015**, *5*, 1–15.

[32] Lin, I.-C.; Seitsonen, A. P.; Tavernelli, I.; Rothlisberger, U. Structure and Dynamics of Liquid Water from Ab Initio Molecular Dynamics-Comparison of BLYP, PBE, and revPBE Density Functionals with and without van der Waals Corrections. *J. Chem. Theory Comput.* **2012**, *8*, 3902–3910.

[33] Benoit, M.; Bernasconi, M.; Focher, P.; Parrinello, M. New High-pressure Phase of Ice. *Phys. Rev. Lett.* **1996**, *76*, 2934–2936.

[34] Bekçioğlu, G.; Allolio, C.; Ekimova, M.; Nibbering, E. T. J.; Sebastiani, D. Competition between Excited State Proton and OH- Transport via a Short Water Wire: Solvent Effects Open the Gate. *Phys. Chem. Chem. Phys.* **2014**, *16*, 13047–13051.

[35] Bekçioğlu, G.; Allolio, C.; Sebastiani, D. Water Wires in Aqueous Solutions from First-principles Calculations. *J. Phys. Chem. B* **2015**, *119*, 4053–4060.

[36] Pines, D.; Pines, E. *Hydrogen-Transfer Reactions*; Wiley-VCH, 2007; pp 377–415.

[37] Rini, M.; Magnes, B.-Z.; Pines, E.; Nibbering, E. T. J. Real-time Observation of Bimodal Proton Transfer in Acid-base Pairs in Water. *Science* **2003**, *301*, 349–352.

[38] Cox, M. J.; Timmer, R. L. A.; Bakker, H. J.; Park, S.; Agmon, N. Distance-dependent Proton Transfer along Water Wires Connecting Acid-Base Pairs. *J. Phys. Chem. A* **2009**, *113*, 6599–6606.

[39] Garczarek, F.; Gerwert, K. Functional Waters in Intraprotein Proton Transfer Monitored by FTIR Difference Spectroscopy. *Nature* **2006**, *439*, 109–112.

[40] Heim, R.; Cubitt, A.; Tsien, R. Improved Green Fluorescence. *Nature* **1995**, *373*, 663–664.

[41] Cui, Q.; Karplus, M. Is "Proton Wire"Concerted or Step-wise? A Model Study of Proton Transfers in Carbonic Anhydrase. *J. Phys. Chem. B* **2003**, *107*, 1071–1078.

[42] Schumaker, M. F.; Pomés, R.; Roux, B. A Combined Molecular Dynamics and Diffusion Model of Single Proton Conduction through Gramicidin. *Biophys. J.* **2000**, *79*, 2840–2857.

[43] Bekçioğlu, G.; Hoffmann, F.; Sebastiani, D. Solvation-dependent Latency of Photoacid Dissociation and Transient IR Signatures of Protonation Dynamics. *J. Phys. Chem. A* **2015**, *119*, 9244–9251.

[44] Headrick, J. M.; Diken, E. G.; Walters, R. S.; Hammer, N. I.; Christie, R. A.; Cui, J.; Myshakin, E. M.; Duncan, M. A.; Johnson, M. A.; Jordan, K. D. Spectral Signatures of Hydrated Proton Vibrations in Water Clusters. *Science* **2005**, *308*, 1765.

[45] de Grotthuss, C. J. T. Sur la décomposition de l'eau et des corps qu'elle tient en dissolution á l'aide de l'électricité galvanique. *Ann. Chim.* **1806**, *58*, 54–73.

[46] Agmon, N. The Grotthuss Mechanism. *Chem. Phys. Lett.* **1995**, *244*, 456–462.

[47] Izvekov, S.; Voth, G. A. Ab Initio Molecular-dynamics Simulation of Aqueous Proton Solvation and Transport Revisited. *J. Chem. Phys.* **2005**, *123*, 44505.

[48] Berkelbach, T. C.; Lee, H.-S.; Tuckerman, M. E. Concerted Hydrogen-Bond Dynamics in the Transport Mechanism of the Hydrated Proton: A First-Principles Molecular Dynamics Study. *Phys. Rev. Lett.* **2009**, *103*, 238302.

[49] Luduena, G. A.; Kühne, T. D.; Sebastiani, D. Reply to Comment on "Mixed Grotthuss and Vehicle Transport Mechanism in Proton Conducting Polymers from Ab initio Molecular Dynamics Simulations". *Chem. Mater.* **2011**, *23*, 3379–3380.

[50] Bekçioğlu-Neff, G.; Allolio, C.; Desmukh, Y. S.; Hansen, M. R.; Sebastiani, D. Dynamical Dimension to the Hofmeister Series: Insights from First-principles Simulations. *ChemPhysChem* **2016**, *17*, 1166–1173.

[51] Tielrooij, K. J.; Garcia-Araez, N.; Bonn, M.; Bakker, H. J. Cooperativity in Ion Hydration. *Science* **2010**, *328*, 1006–1009.

[52] Omta, A.; Kropman, M.; Woutersen, S.; Bakker, H. Influence of Ions on the Hydrogen-bond Structure in Liquid Water. *J. Chem. Phys.* **2003**, *119*, 12457–12461.

[53] Boero, M.; Terakura, K.; Tateno, M. Catalytic Role of Metal Ion in the Selection of Competing Reaction Paths: A First Principles Molecular Dynamics Study of the Enzymatic Reaction in Ribozyme. *J. Am. Chem. Soc.* **2002**, *124*, 8949–8957.

[54] Fedor, M. J.; Williamson, J. R. The Catalytic Diversity of RNAs. *Nat. Rev. Mol. Cell Biol* **2005**, *399*, 399–412.

[55] Hofmeister, F. Zur Lehre von der Wirkung der Salze. *Arch. Exp. Pathol. Pharmakol.* **1888**, *24*, 247–260.

[56] Lo Nostro, P.; Ninham, B. W. Hofmeister Phenomena: An Update on Ion Specificity in Biology. *Chem. Rev.* **2012**, *112*, 2286–2322.

[57] Limbach, H. H. NMR Spectroscopy of Hydrogen-bonded Systems. *Magn. Res. Chem.* **2001**, *39*, 1–2.

[58] Pfrommer, B.; Mauri, F.; Louie, S. NMR Chemical Shifts of Ice and Liquid Water: The Effects of Condensation. *J. Am. Chem. Soc.* **2000**, *122*, 123–129.

[59] Elgabarty, H.; Khaliullin, R. Z.; Kühne, T. D. Covalency of Hydrogen Bonds in Liquid Water Can Be Probed by Proton Nuclear Magnetic Resonance Experiments. *Nat. Commun.* **2015**, *6*.

[60] Rapaport, D. C. *The Art of Molecular Dynamics Simulation*; Cambridge university press, 2004.

[61] Tuckerman, M. *Statistical Mechanics: Theory and Molecular Simulation*; Oxford University Press, 2010; p 720.

[62] Verlet, L. Computer Experiments on Classical Fluids. I. Thermodynamical Properties of Lennard-Jones Molecules. *Phys. Rev.* **1967**, *159*, 98.

[63] Swope, W. C.; Andersen, H. C.; Berens, P. H.; Wilson, K. R. A Computer Simulation Method for the Calculation of Equilibrium Constants for the Formation of Physical Clusters of Molecules: Application to Small Water Clusters. *J. Chem. Phys.* **1982**, *76*, 637.

[64] Nosé, S. A Molecular Dynamics Method for Simulations in the Canonical Ensemble. *Mol. Phys.* **1984**, *52*, 255–268.

[65] Nosé, S. A Unified Formulation of the Constant Temperature Molecular Dynamics methods. *J. Chem. Phys.* **1984**, *81*, 511.

[66] Hoover, W. Canonical Dynamics: Equilibrium Phase-space Distributions. *Phys. Rev. A* **1985**, *31*, 1695–1697.

[67] Martyna, G. J.; Klein, M. L.; Tuckerman, M. Nosé–Hoover Chains: The Canonical Ensemble via Continuous Dynamics. *J. Chem. Phys.* **1992**, *97*, 2635.

[68] Lennard-Jones, J. E. On the Determination of Molecular Fields-II. From the Equation of State of a Gas. *Proc. R. Soc. A* **1924**, *106*, 463–477.

[69] Vanommeslaeghe, K.; Mackerell, A. D. Automation of the CHARMM General Force Field (CGenFF) I: Bond Perception and Atom Typing. *J. Chem. Inf. Model.* **2012**, *52*, 3144–3154.

[70] MacKerell, A. D. et al. All-atom Empirical Potential for Molecular Modeling and Dynamics Studies of Proteins. *J. Phys. Chem. B* **1998**, *102*, 3586–3616.

[71] Ewald, P. P. Die Berechnung optischer und elektrostatischer Gitterpotentiale. *Ann. Phys.* **1921**, *369*, 253–287.

[72] Marx, D.; Hutter, J. *Ab Initio Molecular Dynamics: Basic Theory and Advance Methods*; Cambridge University Press, 2009.

[73] Car, R.; Parrinello, M. Unified Approach for Molecular Dynamics and Density-Functional Theory. *Phys. Rev. Lett.* **1985**, *55*, 2471–2474.

[74] Payne, M. C.; Teter, M. P.; Allan, D. C.; Arias, T. A.; Joannopoulos, J. D. Iterative Minimization Techniques for *Ab Initio* Total-energy Calculations: Molecular Dynamics and Conjugate Gradients. *Rev. Mod. Phys.* **1992**, *64*, 1045–1097.

[75] Tuckerman, M. E. Ab Initio Molecular Dynamics: Basic Concepts, Current Trends and Novel Applications. *J. Phys. Condens. Matter* **2002**, *14*, R1297.

[76] Feynman, R. P. Forces in Molecules. *Phys. Rev.* **1939**, *56*, 340–343.

[77] Hellmann, H. *Einführung in die Quantenchemie*; Deuticke, Leipzig, 1937.

[78] Gross, E. K. U.; Runge, E. *Many-particle Theory*; Germany: Teubner, 1986.

[79] Schrödinger, E. Quantizierung als Eigenwertproblem (Erste Mitteilung). *Ann. der Physik* **1926**, *79*, 361–376.

[80] Born, M.; Oppenheimer, R. Zur Quantentheorie der Molekeln. *Annalen der Physik* **1927**, *389*, 457–484.

[81] Hartree, D. R. *Proc. R. Soc. London* **1928**, *A113*, 621.

[82] Fock, V. Z. Näherungsmethode zur Lösung des quantenmechanischen Mehrkörperaproblems. *Phys.* **1930**, *61*, 126.

[83] Slater, J. C. Note on Hartree's Method. *Phys. Rev.* **1930**, *35*, 210–211.

[84] Slater, J. C. The Virial and Molecular Structure. *J. Chem. Phys.* **1933**, *1*, 687.

[85] Slater, J. C. A Simplification of the Hartree-Fock Method. *Phys. Rev.* **1951**, *81*, 385–390.

[86] Bene, J. E. D.; Ditchfield, R.; Pople, J. A. Self–Consistent Molecular Orbital Methods. X. Molecular Orbital Studies of Excited States with Minimal and Extended Basis Sets. *J. Chem. Phys.* **1971**, *55*, 2236–2241.

[87] Møller, C.; Plesset, M. S. Note on an Approximation Treatment for Many-Electron Systems. *Phys. Rev.* **1934**, *46*, 618–622.

[88] Andersson, K.; Malmqvist, P.; Roos, B. O. Second-order Perturbation Theory with a Complete Active Space Self-consistent Field Reference Function. *J. Chem. Phys.* **1992**, *96*, 1218–1226.

[89] Hohenberg, P.; Kohn, W. Inhomogeneous Electron Gas. *Phys. Rev.* **1964**, *136*, 1B864–B871.

[90] Hohenberg, P.; Kohn, W. Self-consistent Equations Including Exchange and Correlation Effects. *Defense Technical Information Center* **1965**,

[91] Kohn, W.; Sham, L. J. Self-Consistent Equations Including Exchange and Correlation Effects. *Phys. Rev.* **1965**, *140*, A1133–A1138.

[92] Parr, R. G. In *Horizons of Quantum Chemistry: Proceedings of the Third International Congress of Quantum Chemistry Held at Kyoto, Japan, October 29 - November 3, 1979*; Fukui, K., Pullman, B., Eds.; Springer Netherlands: Dordrecht, 1980; Chapter Density Functional Theory of Atoms and Molecules, pp 5–15.

[93] Dreizler, R. M.; Gross, E. K. U. *Density Functional Theory: An Approximation to the Quantum Many-body Problems*; Springer-Verlag: Berlin, 1990; p 302.

[94] Gross, E. K. U., Dreizler, R. M., Eds. *Density Functional Theory*.

[95] Levy, M. Universal Variational Functionals of Electron Densities, First-order Density Matrices, and Natural Spin-orbitals and Solution of the V-representability Problem. *Proc. Natl. Acad. Sci. U.S.A.* **1979**, *76*, 6062–6065.

[96] Lieb, E. H. Density Functionals for Coulomb Systems. *Int. Jour. Quant. Chem.* **1983**, *24*, 243–277.

[97] Koch, W.; Holthausen, M. C. *A Chemist's Guide to Density Functional Theory*; Wiley-VCH, 2000; p 294.

[98] Perdew, J. P.; Schmidt, K. Jacob's Ladder of Density Functional Approximations for the Exchange-correlation Energy. *AIP Conf. Proc.* **2001**, *577*, 1–20.

[99] Dirac, P. A. M. Note on Exchange Phenomena in the Thomas Atom. *Proc. Cambridge Phil. Roy. Soc.* **1930**, *26*, 376–385.

[100] Parr, R. G. Derivation of a Local Formula for Electron-electron Repulsion Energy. *J. Phys. Chem.* **1988**, *92*, 3060–3061.

[101] Sawada, K. Correlation Energy of an Electron Gas at High Density. *Phys. Rev.* **1957**, *106*, 372–383.

[102] Carr, W. J.; Maradudin, A. A. Ground-State Energy of a High-Density Electron Gas. *Phys. Rev.* **1964**, *133*, A371–A374.

[103] Perdew, J. P.; Wang, Y. Accurate and Simple Analytic Representation of the Electron-gas Correlation Energy. *Phys. Rev. B* **1992**, *45*, 13244–13249.

[104] Ceperley, D. M.; Alder, B. J. Ground State of the Electron Gas by a Stochastic Method. *Phys. Rev. Lett.* **1980**, *45*, 566–569.

[105] Langreth, D. C.; Perdew, J. P. Theory of Nonuniform Electronic Systems. I. Analysis of the Gradient Approximation and a Generalization that Works. *Phys. Rev. B* **1980**, *21*, 5469–5493.

[106] Perdew, J. P.; Burke, K.; Ernzerhof, M. Generalized Gradient Approximation Made Simple. *Phys. Rev. Lett.* **1996**, *77*, 3865–3868.

[107] Becke, A. D. Density-functional Exchange-energy Approximation with Correct Asymptotic Behavior. *Phys. Rev. A* **1988**, *38*, 3098–3100.

[108] Lee, C.; Yang, W.; Parr, R. G. Development of the Colle-Salvetti Correlation-energy Formula into a Functional of the Electron Density. *Phys. Rev. B* **1988**, *37*, 785–789.

[109] Perdew, J. P.; Ernzerhof, M.; Burke, K. Rationale for Mixing Exact Exchange with Density Functional Approximations. *J. Chem. Phys.* **1996**, *105*, 9982–9985.

[110] Becke, A. D. Density-functional Thermochemistry. III. The Role of Exact Exchange. *J. Chem. Phys.* **1993**, *98*, 5648–5652.

[111] Vosko, S. H.; Wilk, L.; Nusair, M. Accurate Spin-dependent Electron Liquid Correlation Energies for Local Spin Density Calculations: A Critical Analysis. *Can. J. Phys.* **1980**, *58*, 1200–1211.

[112] Adamo, C.; Barone, V. Toward Reliable Density Functional Methods without Adjustable Parameters: The PBE0 Model. *J. Chem. Phys.* **1999**, *110*, 6158–6170.

[113] Szabo, A.; Ostlund, N. S. *Modern Quantum Chemistry*; McGraw-Hill: New York, 1989.

[114] Pulay, P. Convergence Acceleration of Iterative Sequences. The Case of SCF Iteration. *Chem. Phys. Lett.* **1980**, *73*, 393 – 398.

[115] Bloch, F. Über die Quantenmechanik der Elektronen in Kristallgittern. *Z. Phys.* **1928**, *52*, 555–600.

[116] Slater, J. C.; Koster, G. F. Simplified LCAO Method for the Periodic Potential Problem. *Phys. Rev.* **1954**, *94*, 1498–1524.

[117] Roothaan, C. C. J. New Developments in Molecular Orbital Theory. *Rev. Mod. Phys.* **1951**, *23*, 69–89.

[118] Hall, G. G. The Molecular Orbital Theory of Chemical Valency. VIII. A Method of Calculating Ionization Potentials. *Proc. R. Soc. A* **1951**, *205*, 541–552.

[119] Bloch, F. Über die Quantenmechanik der Elektronen in Kristallgittern. *Z. Phys.* **1929**, *52*, 555–600.

[120] Hellmann, H. A New Approximation Method in the Problem of Many Electrons. *J. Chem. Phys.* **1935**, *3*, 61–61.

[121] Marx, D.; Hutter, J. *Ab Initio Molecular Dynamics: Basic Theory and Advanced Methods*; Cambridge University Press, 2009; p 1669.

[122] Hamann, D. R.; Schlüter, M.; Chiang, C. Norm-Conserving Pseudopotentials. *Phys. Rev. Lett.* **1979**, *43*, 1494–1497.

[123] Goedecker, S.; Teter, M.; Hutter, J. Separable Dual-space Gaussian Pseudopotentials. *Phys. Rev. B* **1996**, *54*, 1703–1710.

[124] Hartwigsen, C.; Gœdecker, S.; Hutter, J. Relativistic Separable Dual-space Gaussian Pseudopotentials from H to Rn. *Phys. Rev. B* **1998**, *58*, 3641.

[125] VandeVondele, J.; Krack, M.; Mohamed, F.; Parrinello, M.; Chassaing, T.; Hutter, J. Quickstep: Fast and Accurate Density Functional Calculations using a Mixed Gaussian and Plane Waves Approach. *Comput. Phys. Commun.* **2005**, *167*, 103–128.

[126] Lippert, G.; Hutter, J.; Parrinello, M. A Hybrid Gaussian and Plane Wave Density Functional Scheme. *Mol. Phys.* **1997**, *92*, 477–488.

[127] Lippert, G.; Hutter, J.; Parrinello, M. The Gaussian and Augmented-plane-wave Density Functional Method for Ab Initio Molecular Dynamics Simulations. *Theor. Chem. Acc.* **1999**, *103*, 124–140.

[128] Chawla, S.; Voth, G. A. Exact Exchange in Ab Initio Molecular Dynamics: An Efficient Plane-wave Based Algorithm. *J. Chem. Phys.* **1998**, *108*, 4697–4700.

[129] Runge, E.; Gross, E. K. U. Density-Functional Theory for Time-Dependent Systems. *Phys. Rev. Lett.* **1984**, *52*, 997–1000.

[130] Marques, M. A. L.; Gross, E. K. U. Time-dependent Density Functional Theory. *Annu. Rev. Phys. Chem.* **2004**, *55*, 427–455.

[131] Putrino, A.; Sebastiani, D.; Parrinello, M. Generalized Variational Density Functional Perturbation Theory. *J. Chem. Phys.* **2000**, *113*, 7102–7109.

[132] Gross, E. K. U.; Kohn, W. Local Density-functional Theory of Frequency-dependent Linear Response. *Phys. Rev. Lett.* **1985**, *55*, 2850–2852.

[133] Gonze, X. Perturbation Expansion of Variational-Principles at Arbitrary Order. *Phys. Rev. A* **1995**, *52*, 1086–1095.

[134] Gonze, X. Adiabatic Density-functional Perturbation Theory. *Phys. Rev. A* **1995**, *52*, 1096–1114.

[135] Baroni, S.; De Gironcoli, S.; Del Corso, A.; Giannozzi, P. Phonons and Related Crystal Properties from Density-Functional Perturbation Theory. *Theory. Rev. Mod. Phys.* **2001**, *73*, 515.

[136] Watermann, T.; Scherrer, A.; Sebastiani, D. In *Many-Electron Approaches in Physics, Chemistry and Mathematics: A Multidisciplinary View*; Bach, V., Delle Site, L., Eds.; Springer International Publishing: Cham, 2014; Chapter Linear Response Methods in Quantum Chemistry, pp 97–110.

[137] Sternheimer, R. M. Electronic Polarizabilities of Ions from the Hartree-Fock Wave Functions. *Phys. Rev.* **1954**, *96*, 951–968.

[138] Limbach, H.-H.; Tolstoy, P. M.; Perez-Hernandez, N.; Guo, J.; Shenderovich, I. G.; Denisov, G. S. OHO Hydrogen Bond Geometries and NMR Chemical Shifts: From Equilibrium Structures to Geometric H/D Isotope Effects, with Applications for Water, Protonated Water, and Compressed Ice. *Isr. J. Chem.* **2009**, *49*, 199–216.

[139] Sebastiani, D. Ab-initio Calculation of Nuclear Magnetic Resonance Parameters in Condensed Phases. *Mod. Phys. Lett. B* **2003**, *17*, 1301–1319.

[140] Sebastiani, D.; Parrinello, M. A New ab-Initio Approach for NMR Chemical Shifts in Periodic Systems. *J. Phys. Chem.* **2001**, *105*, 1951–1958.

[141] Ditchfield, R. Gauge Including Atomic Orbitals. *J. Chem. Phys.* **1972**, *56*, 5688–5691.

[142] Kutzelnigg, W. Individual Gauges for Localized Orbitals. *Isr. J. Chem.* **1980**, *19*, 193.

[143] Keith, A.; Bader, R. F. W. Calculation of Magnetic Response Properties Using a Continuous Set of Gauge Transformations.

[144] Bakker, H. J.; Skinner, J. L. Vibrational Spectroscopy as a Probe of Structure and Dynamics in Liquid Water. *Chem. Rev.* **2010**, *110*, 1498–1517.

[145] Gordon, R. G. Correlation Functions for Molecular Motion. *Adv. Magn. Res.* **1968**, *3*, 1–42.

[146] Ramírez, R.; López-Ciudad, T.; Kumar P., P.; Marx, D. Quantum Corrections to Classical Time-correlation Functions: Hydrogen Bonding and Anharmonic Floppy Modes. *J. Chem. Phys.* **2004**, *121*, 3973–3983.

[147] Marzari, N.; Vanderbilt, D. Maximally Localized Generalized Wannier Functions for Composite Energy Bands. *Phys. Rev. B* **1997**, *56*, 12847–12865.

[148] Silvestrelli, P. L.; Parrinello, M. Water Molecule Dipole in the Gas and in the Liquid Phase. *Phys. Rev. Lett.* **1997**, *82*, 3308–3311.

[149] Silvestrelli, P. L.; Parrinello, M. Structural, Electronic, and Bonding Properties of Liquid Water from First Principles. *J. Chem. Phys.* **1999**, *111*, 3572–3580.

[150] Silvestrelli, P. L.; Bernasconi, M.; Parrinello, M. Ab Initio Infrared Spectrum of Liquid Water. *Chem. Phys. Lett.* **1997**, *277*, 478–482.

[151] King-Smith, R. D.; Vanderbilt, D. Theory of Polarization of Crystalline Solids. *Phys. Rev. B* **1993**, *47*, 1651–1654.

[152] Thomas, M.; Brehm, M.; Fligg, R.; Vohringer, P.; Kirchner, B. Computing Vibrational Spectra from Ab Initio Molecular Dynamics. *Phys. Chem. Chem. Phys.* **2013**, *15*, 6608–6622.

[153] Eigen, M. Proton Transfer, Acid-base Catalysis and Enzymatic Hydrolysis. *Angew. Chem.* **1964**, *3*, 1–19.

[154] Zundel, G. Hydrogen Bonds with Large Proton Polarizability and Proton Transfer Processes in Electrochemistry and Biology. *Adv. Chem. Phys.* **2000**, *111*, 1–217.

[155] Tuckerman, M. E.; Marx, D.; Parrinello, M. The Nature and Transport Mechanism of Hydrated Hydroxide in Aqueous Solution. *Nature* **2002**, *417*, 925.

[156] Morrone, J. A.; Tuckerman, M. E. Ab Initio Molecular Dynamics Study of Proton Mobility in Liquid Methanol. *J. Chem. Phys.* **2002**, *117*, 4403–4413.

[157] Marx, D.; Tuckerman, M. E.; Hutter, J.; Parrinello, M. The Nature of the Hydrated Excess Proton in Water. *Nature* **1999**, *397*, 601.

[158] Chen, H.; Voth, G. A.; Agmon, N. The Kinetics of Proton Migration in Liquid Water. *J. Phys. Chem. B* **2010**, *114*, 333–339.

[159] Ma, Z.; Tuckerman, M. E. On the Connection between Proton Transport, Structural Diffusion, and Reorientation of the Hydrated Hydroxide Ion as a Function of Temperature. *Chem. Phys. Lett.* **2011**, *511*, 177–182.

[160] Geissler, P. L.; Dellagoa, C.; Chandler, D.; Hutter, J.; ; Parrinello, M. Autoionization in Liquid Water. *Science* **2001**, *291*, 2121–2124.

[161] Geissler, P. L.; Dellago, C.; Chandler, D.; Hutter, J.; Parrinello, M. Ab Initio Analysis of Proton Transfer Dynamics in (H2O)3H+. *Chem. Phys. Lett.* **2000**, *321*, 225–230.

[162] Tolbert, L. M.; Haubricht, J. E. Photoexcited Proton Transfer from Enhanced Photoacids. *J. Am. Chem. Soc.* **1994**, *116*, 10593–10600.

A Abstract/Kurzzusammenfassung

Abstract

This thesis addresses the computational modeling of the fast molecular dynamics of aqueous hydrogen bond networks in condensed systems at ambient temperatures, with a particular focus on spectroscopic fingerprints of proton dynamics on short timescales (femtosecond to picoseconds) and of hydration phenomena of solvated ions. Both phenomena are highly relevant in the context of biophysical systems such as proteins and their water channels which can serve as ion transporters. Within this thesis, specific benchmark molecules provide a well-defined model environment which allow a calculation of quasi quantitative structure-property-relationships. By means of *ab initio* molecular dynamics simulations, structural and dynamical phenomena as well as spectroscopic features are extracted from the trajectories at ambient conditions.

In the first part of this thesis, a specific set of bifunctional chromophores (hydroxyquinoline derivatives) is investigated in aqueous solution, which contains a specific acid/base functionality which can be triggered by photoexcitation. The main focus is characterization of the (persistent) extended hydrogen bonded chains of water molecules along which the proton exchange is supposed to occur. The existence and persistence of different lengths of water wires on the picosecond timescale is elucidated in relation to the lifetimes of the involved hydrogen bonds, and compared with bulk situations. The simulations show that the dynamics of bulk water wires substantially differs from the dynamics of water wires connecting the acidic and basic sites of the chromophores. Furthermore, proton dissociation mechanisms in aqueous solution are examined with initiation by electronic excitation of a super photoacid N-methyl-6-hydroxyquinolinium cation. The details of fast electronic rearrangements of the chromophore, and the following proton dissociation steps upon excitation are investigated in a complex hydrogen bonded network. The early stages in proton dissociation are found to be accompanied by rearrangements in local hydrogen bonding in the vicinity of the acidic proton, and characterized by a broad absorption line in the computed IR spectra.

In the final study, aqueous solvation of a series of divalent ions is investigated in order to characterize the ion-specific effects (kosmotropic/chaotropic features). The simulations show significant structural and dynamical differences in the characteristics of hydrogen bonds in the first solvation shell of ions with respect to the situation in bulk water. The good overall agreement between the computed ^{1}H NMR chemical shifts and the experimental values confirm the kosmotropic/chaotropic nature of ions on the local solvent structure.

The questions and challenges addressed in this thesis can contribute significantly to atomistic understanding of the proton dissociation processes involved, and impact of ions on the local hydrogen bonded network. The findings demonstrate a fully consistent first-principles treatment in which *ab initio* molecular dynamics simulations can complement spectroscopic observables leading to direct comparison of theory and experiment.

Kurzzusammenfassung

In der vorliegenden kumulativen Dissertation werden einige Studien über die schnelle Dynamik von Wasserstoffbrücken-Netzwerken in kondensierten wässrigen Umgebungen vorgestellt. Dabei werden vor allem spektroskopische Signaturen der Protonendynamik auf der Femto- und Pikosekundenskala betrachtet, und komplementär hierzu auch strukturelle und dynamische Eigenschaften der Hydrathülle einer Reihe von Salzionen. Beide Phänomene sind von erheblicher Relevanz im biophysikalischen Kontext, wo vergleichbare Vorgänge in Wasserkanälen von Proteinen stattfinden, in denen oft Ionen transportiert werden können. Im Rahmen dieser Dissertation liegt der Fokus vor allem auf Modellsystemen, die eine definierte Struktur des Wasserstoffbrücken-Netzwerks erzeugen können. Auf methodischer Seite finden vor allem die Ab-initio-Molekulardynamik-Simulationen Anwendung, mit denen normale Umgebungsbedingungen mit recht guter Genauigkeit simuliert werden können.

Im ersten Teil der Arbeit werden bifunktionale Chromophore betrachtet, die eine photogetriggerte Säure-Base-Funktionalität besitzen. Mit Hilfe der hierdurch wohldefinierten Protonen-Donor- und Akzeptor-Geometrie können Lebensdauer und Protonenleitungs-Fähigkeiten von Molekülketten aus Wassermolekülen untersucht werden. Es zeigt sich, dass diese sogenannten Wasser-Drähte (aus Wasserstoffbrücken) eine deutlich veränderte Struktur und Dynamik besitzen, wenn sie statt in der homogenen Wasserphase an den vordefinierten Säure/Base-Gruppen beginnen und enden. Mit Hilfe von Molekulardynamik-Simulationen wird anschliessend gezeigt, wie der Protonentransfer nach Photoanregung des Chromophors abläuft, und wie die Solvathülle um das saure Proton auf dessen Bewegung reagiert. Die Dynamik findet in diesem Fall auf einer Zeitskala von wenigen Pikosekunden statt, und kann experimentell mit zeitaufgelöster IR-Spektroskopie erfasst werden. Durch die in der vorliegenden Arbeit vorgestellten Simulationen können die entsprechenden Messergebnisse nun auch quantitativ interpretiert werden.

Im letzten Teil der Arbeit liegt der Fokus auf der Solvatisierung von Salzionen, die jeweils entweder kosmotrope (strukturbildende) oder chaotrope (strukturreduzierende) Funktion im wässrigen Wasserstoffbrückennetzwerk haben. Die Simulationen werden durch den Vergleich zwischen berechneten und gemessenen Protonen-NMR chemischen Verschiebungen validiert.

Hauptziel der vorliegenden Dissertation ist die Verbesserung des quantitativen Verständnisses der Pikosekunden-Dynamik von Wasserstoffbrückennetzwerken in der wässrigen Phase in biophysikalisch relevanten Situationen, mit besonderem Fokus auf dem Einfluss von äusseren Störungen wie die Protonierungsdynamik und gelöste Ionen.

B Publications

Below is a list of the scientific publications that constitute this cumulative dissertation with detailed descriptions of the individual responsibilities and contributions of the respective authors;* the reprints of these articles can be found on the following pages.

[P1] Bekçioğlu G., Allolio C., Ekimova M., Nibbering E., and Sebastiani D.
Competition between Excited State Protons and OH^- Transport via a Short Water Wire: Solvent Effects Open the Gate;
Phys. Chem. Chem. Phys. **2014**, 16, 13047-13051

For this publication, I prepared the computational setup of the solvated chromophore. In addition, I performed the analysis of the numerical results and wrote the manuscript. C. Allolio contributed to evaluation of the findings. Experimental data was provided by M. Ekimova (Postdoc fellow) who was working under the supervision of E. Nibbering. D. Sebastiani acted as the supervisor the project, he coordinated the work and contributed to the redaction of the manuscript. This paper corresponds to Section 3.1.

[P2] Bekçioğlu G., Allolio C., and Sebastiani D.
Water Wires in Aqueous Solutions from First-Principles Calculations;
J. Phys. Chem. B **2015**, 119, 4053-4060

In this project, I prepared the setup of the solvated chromophores and performed all numerical molecular dynamics simulations. In addition, I performed the analysis of the numerical results and wrote the manuscript. C. Allolio contributed to analysis of the trajectories. D. Sebastiani acted as the supervisor the project, he coordinated the work and contributed to the redaction of the manuscript. This paper corresponds to Section 3.1.

[P3] Bekçioğlu G., Hoffmann F., and Sebastiani D.
Solvation-Dependent Latency of Photoacid Dissociation and Transient IR Signatures of Protonation Dynamics;
J. Phys. Chem. A **2015**, 119, 9244-9251

In this project, I prepared the computational setup of the molecular systems and performed major part of the numerical quantum chemical calculations. F. Hoffmann computed IR spectra from the trajectories, and contributed to their analysis and interpretation of the numerical data. I summarized the results and wrote the major part of the manuscript. D. Sebastiani acted as the supervisor the project, he coordinated the work and contributed to the redaction of the manuscript. This paper corresponds to Section 3.1.

*Please note that the candidate's name changed from Bekçioğlu to Bekçioğlu-Neff; to emphasize, the candidate's name is underlined in the listing of the authors.

[P4] Bekçioğlu-Neff G., Allolio C., Desmukh Y. S., Hansen M. R., and Sebastiani D.
Dynamical Dimension to the Hofmeister Series: Insights from First-Principles Simulations;
ChemPhysChem **2016**, 17, 1166-1173

In this project, I prepared the setup of the solvated ions and performed a major part of the numerical molecular dynamics simulations. Some of the molecular dynamics simulations were conducted by C. Allolio. In addition, I analyzed the trajectories and evaluated the results, and wrote the manuscript. Experimental NMR data was provided by Y. S. Deshmukh, in collaboration with M. R. Hansen. D. Sebastiani acted as the supervisor the project, he coordinated the work and contributed to the redaction of the manuscript. This paper corresponds to Section 3.2.

Competition between Excited State Protons and OH^- Transport via a Short Water Wire: Solvent Effects Open the Gate

Bekçioğlu G., Allolio C., Ekimova M., Nibbering E. T. J., and Sebastiani D.

Phys. Chem. Chem. Phys. **2014**, 16, 13047-13051.

DOI: http://dx.doi.org/10.1039/C4CP00970C

This article is not available in the online version.

This article is not available in the online version.

This article is not available in the online version.

This article is not available in the online version.

This article is not available in the online version.

This article is not available in the online version.

Water Wires in Aqueous Solutions from First-Principles Calculations

Bekçioğlu G., Allolio C., and Sebastiani D.

J. Phys. Chem. B **2015**, 119, 4053-4060.

DOI: http://dx.doi.org/10.1021/jp5121417

THE JOURNAL OF PHYSICAL CHEMISTRY B

Article

pubs.acs.org/JPCB

Water Wires in Aqueous Solutions from First-Principles Calculations

Gül Bekçioğlu,[†,‡] Christoph Allolio,[‡,§] and Daniel Sebastiani*[,‡]

[†]Physics Department, Freie Universität Berlin, Arnimallee 14, 14195 Berlin, Germany

[‡]Institut für Chemie, Martin-Luther-Universität Halle-Wittenberg, Von-Danckelmann-Platz 4, 06120 Halle (Saale), Germany

[§]Institute of Organic Chemistry and Biochemistry, Academy of Sciences of the Czech Republic, Flemingovo nám 2, CZ-16610 Prague 6, Czech Republic

Supporting Information

ABSTRACT: We elucidate the concept of water wires in aqueous solutions in view of their structural and dynamical properties by means of first-principles molecular dynamics simulations. We employ a specific set of hydroxyquinoline derivatives (heteroaromatic fluorescent dyes) as probe molecules that provide a well-defined initial and final coordinate for possible water wires by means of their photoacid and photobase functionalities. Besides the geometric structure of the hydrogen bond network connecting these functional sites, we focus on the dependence of the length of the resulting water wire on the initial/final coordinates determined by the chromophore. Special attention is devoted to the persistence of the wires on the picosecond time scale and their capability of shifting the nature of the proton transfer process from a concerted to a stepwise mechanism. Our results shed light on the long debate on whether water wires represent characteristic structural motifs or transient phenomena.

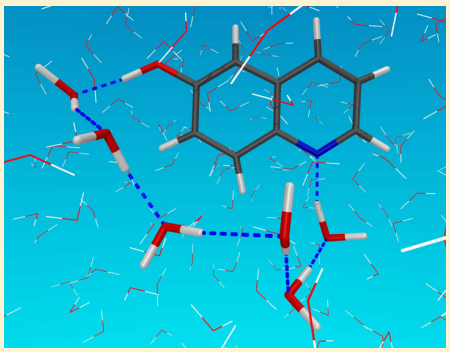

1. INTRODUCTION

A protic solvent such as water often plays a crucial role in proton transfer reactions due to its ability to form an extended hydrogen bonded network.[1−8] The specific interaction of the hydrogen bond network of water with solvated compounds influences the whole reaction path by stabilizing the reaction intermediates and products via lowering of reaction barriers. In this regard, there is an ongoing debate on the ability of water to form a persistent hydrogen bonded chain (i.e., a water wire) through which the transport of a proton can occur. Water wires have been postulated in a number of studies dealing with proton transport in biological systems,[9−11] including the proton pump protein bacteriorhodopsin,[12] green fluorescent protein,[13,14] carbonic anhydrase,[15] and gramicidin A.[16] It remains debatable whether such water wires also exist for proton transfer in *bulk* water, i.e., without strong outer confinement.

Organic fluorescent bifunctional chromophores have a wide range of applications as molecular probes in various areas.[17−20] In this regard, bifunctional heteroaromatic molecules, hydroxyquinolines (HQs) and its derivatives, have been extensively studied due to their fundamental and practical features.[21−32] Two members of this family, 6- and 7HQ probe molecules, provide both proton donor and acceptor groups at well-defined positions, to which a water wire may be engaged (see Figure 1). Such a well-defined proton transfer pathway is difficult to observe directly inside a protein. Therefore, HQs can be seen as as a model system to observe the properties of hydrogen bonded wires. HQs exhibit large changes in acidity/pK_a properties upon electronic excitation. Photoacidity/-basicity is the result of intramolecular changes in the electronic structure

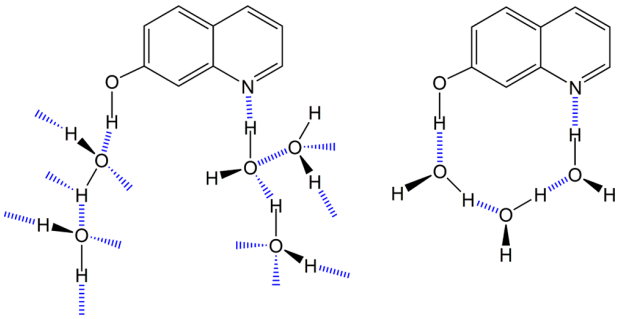

Figure 1. Possible solute−solvent interactions between 7HQ and water molecules. Independent water molecules hydrating donor/acceptor sites are on the left side, while the water wire engaging the donor/accpetor sites is on the right side.

compared to the situations in the electronic ground state. The excited states of HQ and its derivatives have been examined in different solvents both experimentally and computationally by several groups including our group.[33−40] In the previous computational studies on 6- and 7HQ, most simulations start with a predefined arrangement of an isolated cluster of H-bonded solvent molecules, and then perform ab initio calculations of reaction barriers for proton/hydroxide ion transfer in the excited state. In these situations, the predefined H-bonded network represents a well-defined pathway for proton

Received: December 5, 2014
Revised: February 17, 2015
Published: February 25, 2015

DOI: 10.1021/jp5121417
J. Phys. Chem. B 2015, 119, 4053−4060

transport, and the pathway obtained upon photoexcitation necessarily follows this trajectory. On the experimental side, HQs in solution have been studied with transient electronic spectroscopy with time-resolved fluorescence measurements.[21−29,41] These experiments showed that fluorescence generated by the photoexcitation of 7HQ in water and methanol solutions reveals two rise components, concluding that the solute exists in the solution in two distinct states of solvation depicted in Figure 1.[29,42−44] These results suggest two corresponding processes:

- first a fast process which is accompanied by the intrinsic proton transfer through a solvent wire with an optimal configuration existing already at the moment of excitation
- a slow process starting from solvent reorganization to form a solvent wire with optimal configuration, which accordingly undergoes proton transfer rapidly

Although in the experiments no explicit evidence for water wires mediating proton transfer has been found, the possibility of the presence of such wires is often assumed as a characteristic motif of the hydrogen bond network, and used as a basis for the understanding of protonation dynamics pathways. Therefore, detailed information on the ground state solvation is required in the first place, prior to the excited state proton transfer reactions.[45] Recently, the ground state proton transfer dynamics of 7HQ has been studied by Jang and co-workers with configurational optimization in a hydrogen bonded alcohol wire.[46]

In the present paper, we elucidate the relationships between local hydrogen bonding structure and picosecond time-resolved fluorescence experiments. We investigate the ground state aqueous solvation of 6- and 7HQ by means of first-principles molecular dynamics simulations in the condensed phase. Being complementary to experiment, ab initio molecular dynamics can elucidate the microscopic details of the aqueous solvation dynamics in terms of correlation between microscopic configurations and spectroscopic parameters. In particular, we deal mainly with the microscopic details of the water configurations in terms of local structural motifs such as water wires between the polar sites of the probe molecules. We aim to understand the water reorganization to form water wires with optimal configuration that takes place prior to the excited state proton transfer process. Consequently, we hope to support the interpretation of experimental results in model systems, in view of transferring this knowledge to more complex biomolecular systems which exhibit similar processes, e.g., ion channel proteins.

1.1. Computational Details. The molecular dynamics were staged in a cubic, periodic box with a side length of about 21.58 Å with 6HQ·340 H_2O and a side length of 21.45 Å with 7HQ·341 H_2O at a density of d = 1.0 g/cm^3. The solvation boxes are thermostated first for 12 ps, using a Nosé−Hoover thermostat with a time constant of 50 fs at a temperature of 350 K and then continued 18 ps of a run with a time constant of 600 fs for ground state for both systems. With the increase in temperature, we hope to counter overstructuring effects, found in water simulations at lower temperature.[47] In addition, we used the DFT-D2 dispersion corrections[48] to account for dispersion effects.

For all calculations, we used the GPW[49] scheme as implemented in the CP2K[50] software package. The BLYP functional was used with a TZVP valence basis set,[51] Goedecker[52] potentials, and a 350 Ry plane-wave cutoff. We used restricted Kohn−Sham DFT and a time step of 0.5 fs for the ground state calculations. The total length of ab initio trajectories used was 110 ps.

All DFT based static electronic structure calculations were carried out by using the Gaussian 09 program.[53] The conventional DFT calculations using the hybrid exchange-correlation functional B3LYP[54] were perfomed in the gas phase and in the presence of the CPCM model.[55] The basis set was TZVP for these calculations.

1.2. Hydrogen Bond Definition. We define a hydrogen bond by a combined criterion involving the oxygen−oxygen distance and the O−H−O angle between water molecules. Our choice was $r_{OO} < 3.5$ Å, $(O_2; O_1; H_1) < \pi/6$, which is a common definition.[56] In addition to that, 2.45 Å is used as the sole criterion for the nitrogen−hydrogen bond (see the Supporting Information).

2. RESULTS AND DISCUSSION

2.1. Conformation of Aqueous Solvated 6- and 7-Hydroxyquinolines. Two spatial arrangements available to HQs, shown in Figure 2 by rotation of the hydroxyl group

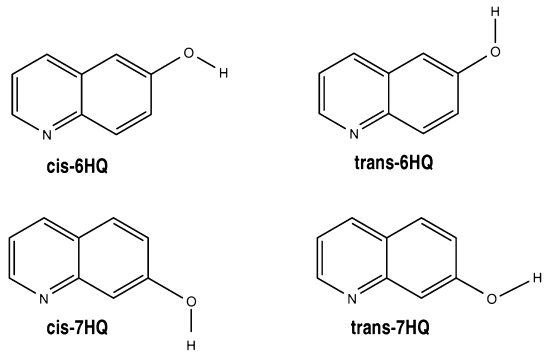

Figure 2. Structures of 6- and 7HQs with their rotational conformations of the hydroxyl group.

with respect to the nitrogen atom, are called cis and trans conformations, in which the hydroxyl O−H bond points down and up, respectively. We confirmed the coexistence of cis and trans conformers of 6- and 7HQs in their ground state by means of first-principles calculations. The full structure optimization calculations were performed in the vacuum and aqueous solution without any symmetry constraint. Solvation effects were captured by the conductor polarized continuum model.

The trans-7HQ is found to be 5.1 and 1.8 kJ mol^{-1} less stable than cis-7HQ in the vacuum and the presence of implicit solvent medium, respectively. In contrast, the trans-6HQ is found to be more stable in energy than cis-6HQ by 1.7 and 1.6 kJ mol^{-1} in the vacuum and presence of implicit solvent, respectively. It should be noticed that, under implicit aqueous solvation, the energy difference between the two rotomers is significantly below k_BT (at $T \sim 300$ K). This indicates that HQs arrange into fast rotational isomerization among the energetically approachable conformations rather than remaining rarely immobilized in a single conformation. Furthermore, in the condensed aqueous solvation of the 6- and 7HQ, cis and trans rotamers are isoenergetic and will therefore be indistinguishable in room temperature experiments.

DOI: 10.1021/jp5121417
J. Phys. Chem. B 2015, 119, 4053−4060

In order to observe the conformational isomerization in an actual molecular dynamics trajectory, we started runs for both 6- and 7HQ in the cis conformation at 350 K. In both cases, we indeed detected the geometric isomerization to the trans conformation within a simulation period of 14 and 6 ps for 6- and 7HQ, respectively.

2.2. Existence of Water Wires. The existence and the stability of the hydrogen bond network that connects the donor and acceptor sites of a photoacid/-base is an ongoing matter of debate.[1−6,57] Figure 3 shows an example of such a water wire

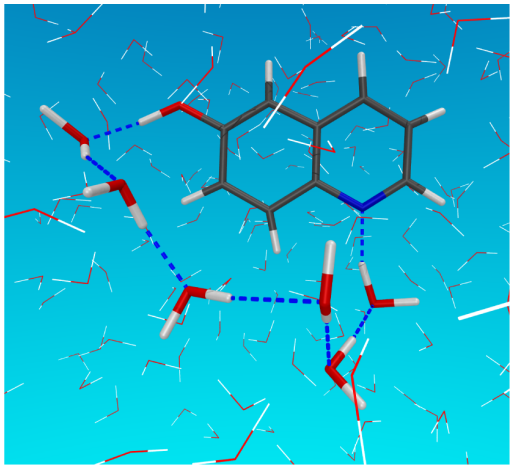

Figure 3. Snapshot from the MD trajectory of cis-6HQ with the water wire between proton donor and acceptor sites.

configuration. In liquid bulk water at ambient temperature, the hydrogen bond network has only a very short lifetime and its autocorrelation function is typically relaxed within a few picoseconds.[58,59] It should be noted here that the latter is certainly also a question of the definition of the time scale at which a water wire is considered stable. Here, we address this aspect by focusing on the existence of a reactive solute−water wire complex at a given moment (at the moment of excitation), and their persistence for a typical duration of a proton exchange reaction. The alternative scenario would be that the proton exchange trajectories mostly involve pathways that had not existed at that time.

We have computed the spatial distribution function (SDF) of water oxygen atoms between the polar sites of the probe molecules from our ab initio MD simulations (see the Supporting Information).[60] SDFs can provide the three-dimensional information on the location of water oxygen atoms, and therefore contain essential details about the spatial positions of water molecules interacting with HQs. These water oxygen atom densities are shown in Figure 4, which shows the most likely positions of water oxygen atoms (red clouds). Parts a and b show results for cis- and trans-7HQ, while parts c and d show the cis- and trans-6HQ, respectively. In general, these maps show that the water oxygen atoms are well localized in the hydrophilic regions of the chromophores, as expected. This indicates a strong structure-inducing effect of the HQ hydroxyl group and nitrogen atom, and water molecules in their immediate vicinity. Further than that, there are additional high-density clouds at specific locations between donor/acceptor sites which illustrate that the structure-enhancing effect clearly goes beyond the directly hydrogen bonding water molecules. The resulting pattern of high-oxygen-density clouds follows a

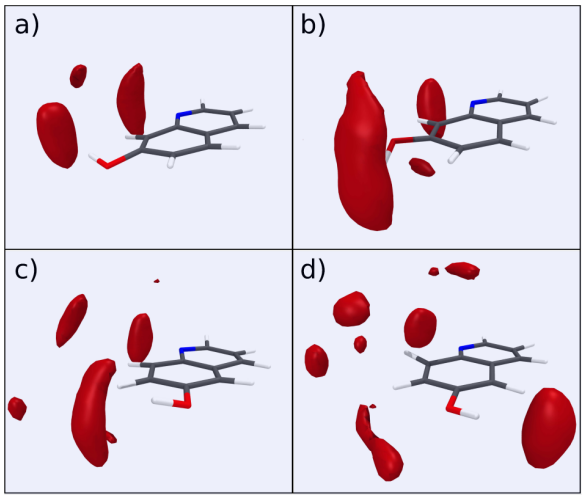

Figure 4. Spatial distribution functions of water oxygen atoms (red surface) around and between the hydroxyl group and nitrogen atom of (a) cis-7HQ, (b) trans-7HQ, (c) cis-6HQ, (d) and trans-6HQ.

specific path between donor/acceptor sites, which represents a consistent signature of a possible connected water wire.

2.3. Hydrogen Bond Network Dynamics. *2.3.1. Persistence of Water Wires.* The concept of water wires intrinsically raises the question of the persistence of an extended H-bond network of water molecules for characteristic time scales, e.g., those on which a proton exchange occurs. We address this aspect by determining the evolution of the hydrogen bonded network between polar sites of the probe molecules. We computed the number of hydrogen bonded water molecules which are connecting directly the nitrogen atom and hydroxyl group of HQs for each snapshot of our ab initio molecular dynamics trajectories (see the Supporting Information).

The occurrence of these water wires of cis- and trans-6- and 7HQs is consolidated in the histograms shown in Figure 5. The histograms thus show the probability of finding water wire consisting of a given number of water molecules connecting the polar sites of the probe molecules. Figure 5 indicates that the chemical variation (6- and 7HQ) and hydroxyl group conformation lead to characteristic changes in the distribution of the water wire pattern. For cis-7HQ, there is a preference toward a typical length of three to four water molecules, while, for the trans-7HQ, on the other hand, a water wire of six molecules represents the dominant motif. This result is consistent with previous combined spectroscopic and total energy calculations of the 7HQ·$(H_2O)_2$ complex,[31] where a water wire of two to three molecules was found to be crucial for the microscopic description of solvation and proton transfer reactions.

A water wire of six molecules is the length for the cis-6HQ. However, it is not as frequent as the one with eight water molecules. For the trans-6HQ, very few water wires composed of 5−7 molecules are observed; the typical length is rather 9−11 waters. Thus, conformational isomerization and chemical variation of the donor/acceptor sites on the probe molecules have a strong effect on the length of the resulting water wires. While a translation of the hydroxyl donor group by one carbon site yields almost a doubling in the length (4 → 8 and 6 → 11), the geometric isomerization results typically in an extension by only two water molecules.

2.3.2. Wires in Bulk Water versus HQ-Terminated Water Wires. Another interesting objective here is to establish an

DOI: 10.1021/jp5121417
J. Phys. Chem. B 2015, 119, 4053−4060

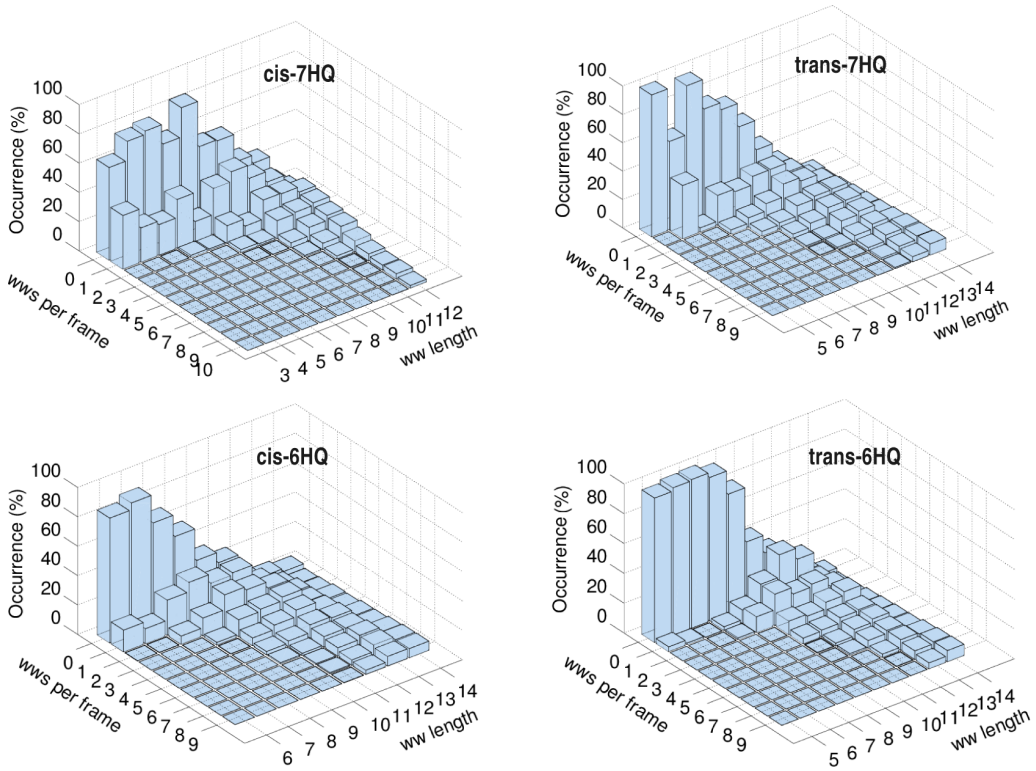

Figure 5. Occurrence of water wires (WWs) terminating at both the hydroxyl group and nitrogen of HQs.

atomistic comparison between lifetimes of water wires in bulk water and water wires of the same length connecting between the donor and acceptor sites of HQs. For such a comparison, we introduce here an autocorrelation function for the water wires as

$$C_{ww}^{k}(t) \equiv \frac{1}{\langle \eta_i^k(t_0) \rangle^2} \langle \eta_i^k(t_0 + t) \cdot \eta_i^k(t_0) \rangle \tag{1}$$

where $\langle ... \rangle$ denotes an average over all water wires of a given length k. $\eta_i^k(t)$ is a water wire population descriptor for a water wire of length k. i is defined as an index to count the number of existing water wires of a given length k in each frame. Specifically, $\eta_i^k(t) = 1$ if a tagged loop-free directed hydrogen bonded path of length k exists at time t and $\eta_i^k(t) = 0$ otherwise. The scalar product reduces to the number of water wires present at time t_0 and t simultaneously. It is important to note here that $C_{ww}^{k}(t)$ is insensitive to temporary interruptions of water wires. We have used the same geometric criteria to define the hydrogen bonds between two water molecules as described in the previous section. In order to compare the water wires in bulk, we have computed water wire autocorrelations according to eq 1. For the bulk fraction of our simulation box, we used a spherical cutoff of 5 Å around the HQs, corresponding to the first peak of the radial distribution function $g_{CO}(r)$ between the carbon atom of the HQs and the oxygen atom of water (see the Supporting Information). Complementary to this, we computed the wires in bulk water with a fixed end-to-end distance cutoff of 5 Å for cis-7HQ.

In Figure 6, we plotted the water wire autocorrelation function as a function of k. We found that the dynamics of bulk water wires substantially differs from the dynamics of water wires connecting the acidic and basic sites of cis-7HQ. Similar observations are met with other HQs which are reported in the Supporting Information. In the bulk, the water wire lifetime decreases linearly with increasing number of water molecules (see the Supporting Information). However, there is no such trend for the water wires connecting the donor and acceptor sites of cis-7HQ. It is well evident in Figure 6 that water wires with length $k = 3$ and $k = 6$ decay much slower and nonexponentially. Note that the water wire length $k = 6$ topology is accompanied by the same water molecules which form the water wire length $k = 3$. This surprising observation indicates that a considerably more stable HB network arrangement is achievable with water of these "magic" lengths.

To verify this interpretation, we have computed the water HB autocorrelation function within the vicinity of the first hydration shell of carbon atoms of HQs (4 Å) and outside of these regions.

$$C_{HB}(t) \equiv \frac{1}{\langle h(t_0) \rangle^2} \langle h(t_0 + t) \cdot h(t_0) \rangle \tag{2}$$

For this autocorrelation function, we used the same HB criterion as before. Again, $h(t)$ is unity when two tagged molecules are hydrogen bonded at time t and is $h(t) = 0$ otherwise. This function $C_{HB}(t)$ represents the conditional probability that a HB remains intact for a time t, given it was intact at time t_0. Again, $C_{HB}(t)$ ignores temporary breaking of HB.

In Figure 7, we found slightly slower decay of $C_{HB}(t)$ in the vicinity of the first hydration shell which indicates the kosmotropic effect of the internal hydrophobic interface around the aromatic ring of HQ, stabilizing the water wires and retarding water reorientation dynamics.[8,10,61] This is consistent with recent work by Laage and co-workers, where it was shown

DOI: 10.1021/jp5121417
J. Phys. Chem. B 2015, 119, 4053−4060

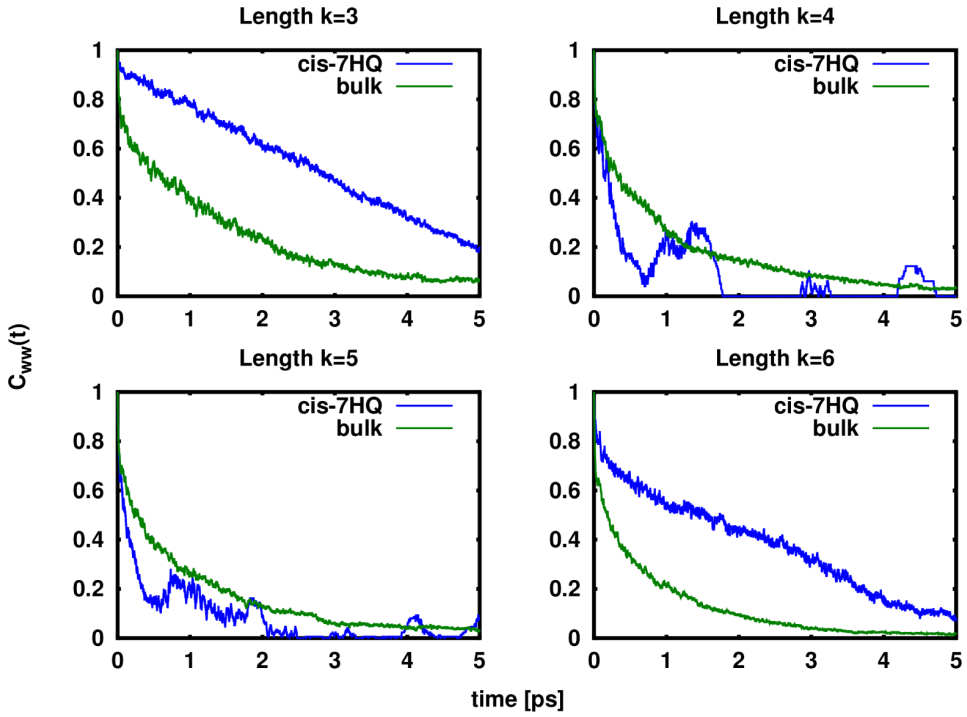

Figure 6. Water wire autocorrelation functions for water wires connecting the active sites of cis-7HQ (blue curve) and wires in bulk (green curve). Decays of the hydrogen bond autocorrelation functions are computed by averaging over 250 and 1000 random starting points for bulk and cis-7HQ water wires, respectively.

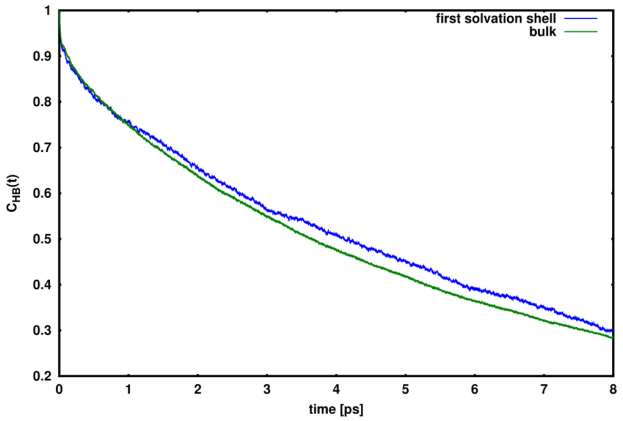

Figure 7. Hydrogen bond autocorrelation functions for hydrogen bonds between water for bulk water molecules (green curve) and within a distance of 4 Å of cis-7HQ (blue curve). Decays of the hydrogen bond autocorrelation functions are computed by averaging over 100 random starting points.

that the HB exchange (water rotation) process slowed down due to the excluded volume effect by the hydrophobic solute.[10,62] Therefore, the short water wires which are formed in the first solvation shell of HQs are more persistent with respect to the longer ones.

2.3.3. Water Wires and Proton Exchange Pathways. The number of water molecules in a water wire between two active sites (here, proton donor and acceptor sites of the photoacid) have a considerable influence on the nature of the proton transfer mechanism. In particular, the proton can in principle follow either a stepwise reaction dynamics or alternatively a concerted transfer mechanism.[63−71] Concerted mechanisms likely occur for smaller proton transport distances, and a change into sequential transfer then is anticipated when the proton transport distance increases. This striking dynamical activity could also be driven partly by the ability of the water wires to undergo collective compressions with the presence of an excess proton.[70,71] In addition to that, oxygen−oxygen separations are also clearly related to the energy barrier for proton transfer. Shortening the oxygen−oxygen distance decreases the energy barrier for proton transfer.

To relate the concerted mechanism to such structural features of water wires, we have calculated the maximum oxygen−oxygen distance for the suitable water wires of length k = 3, ..., 6 of cis-7HQ. Figure 8 shows these short water wire configurations with their maximum oxygen−oxygen distances. We observe a similar phenomenon as that for the hydrogen bond network autocorrelation function: For water wires of "magic" length k = 3 and k = 6, the distribution is somewhat sharper peaked at its maximum of 2.9−3.0 Å. In turn, for k = 4 and k = 5, the long-distance-tails (i.e., where the maximum O−O distance reaches values above 3.0 Å) is more pronounced. This finding supports the hypothesis of an increased stability of water wires of length k = 3 and k = 6, and further an increased likelihood of concerted proton transfer processes. Consequently, these water wires would be more stabilized by the presence of an excess proton allowing the concerted proton transfer event for cis-7HQ.[40]

On the other hand, in the stepwise process, stable H_3O^+ (or OH^-) intermediates will exist at intermediate periods of time (longer than vibrational modes but shorter than the total transfer duration), while the concerted transport reaction is characterized by their absence. On the other hand, it was known in a study of protonated linear chains of water

DOI: 10.1021/jp5121417
J. Phys. Chem. B 2015, 119, 4053−4060

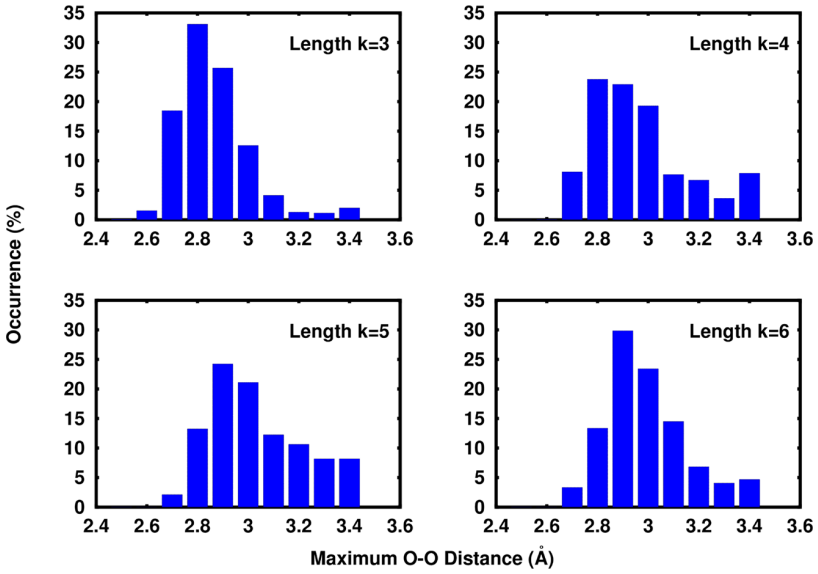

Figure 8. Histogram of the maximum oxygen−oxygen distances along water wires terminating at both the hydroxyl group and nitrogen of cis-7HQ.

molecules that proton transfer along the chain is an extremely fast process, occurring in subpicosecond time scales.[72,73] In such a short linear chain of water molecules, the translocation mechanism of the proton was found to be neither a concerted mechanism nor a result of a single proton hopping along the chain. The translocation process rather involved a series of semicollective motion during which rapid fluctuations of the hydrogen bond lengths along with reorganizations of water molecules are observed.[74−77]

So far, experimental work also could not give a conclusive dependence between the length of a water wire and the nature of the corresponding proton transfer reaction;[29,78,79] only the presence and absence of vibrational signals of intermediates is observable experimentally. Combining our present results with additional previous molecular dynamics simulations[40,63−68] and femtosecond transient IR experiments,[5,78] we can now conclude that a real concerted mechanism for proton conduction along a persistent water wire can only happen for water wires of four molecules and less.[80] Larger chains are interrupted too frequently, allowing only a stepwise mechanism, even if the interruptions are of transient nature.

3. CONCLUSION

In this work, we have elucidated structural and dynamical characteristics of water wires of typical length and time scales of 5−15 Å and 2−4 ps, respectively. The concept of water wires is a controversial matter, partially due to a lack of well-defined quantitative criteria but also due to uncertainties regarding the microscopic understanding of the corresponding relevant molecular motion.

We have addressed this issue by looking at the hydrogen bond network (and its dynamics) between two well-defined geometric sites, which are represented by the hydrogen bond donor and acceptor sites of two specific photoacid/-base chromophores from the hydroxyquinoline family (6- and 7HQ). Both exist in two rotamers, yielding a total of four initial/final coordinates for a water wire. Such photoacids/-bases are of particular interest because transient time-dependent femtosecond IR spectroscopy can provide spectroscopic fingerprints of intermediate conformations during a proton transfer process initiated by electronic excitation. These intermediate structures provide experimental evidence for the existence, persistence, and relevance of water wires between the donor/acceptor sites.

Different topologies of possible protonation pathways are discriminated by their geometric properties, in particular the number of water molecules. Our ab initio molecular dynamic simulations showed that the water wire patterns for the cis conformation are more stable than the trans conformers. We found that cis-7HQ can indeed establish short water wires consisting of three to six molecules, which can accelerate proton exchange reactions by lowering the reaction barrier, favoring a concerted proton transfer reaction. For other HQ derivatives, the length of the water wires is larger (five molecules and more), which would yield a stepwise proton transfer process.

Our molecular dynamics simulations provide a consistent picture of hydrogen bonded chains between well-defined sites of solvated photoacids/-bases. The present study provides elements to reconcile the transient water wire motifs with a detailed atomistic picture of hydrogen bonding in aqueous bulk solutions. Our results provide a sound microscopic basis for the interpretation of femtosecond transient fluorescence and IR experiments in terms of the water wire concept.

■ ASSOCIATED CONTENT

Supporting Information

Computational details and characterization data for the simulations. This material is available free of charge via the Internet at http://pubs.acs.org.

■ AUTHOR INFORMATION

Corresponding Author

*E-mail: daniel.sebastiani@chemie.uni-halle.de.

Notes

The authors declare no competing financial interest.

■ ACKNOWLEDGMENTS

The computing infrastructure was provided by the NIC supercomputers of the Research Centre Jülich. This work was

DOI: 10.1021/jp5121417
J. Phys. Chem. B 2015, 119, 4053−4060

supported by Leibniz Graduate School of Molecular Biophysics Berlin and German Research Foundation (DFG) under grant SE 1008/11-1.

REFERENCES

(1) Hayes, R. L.; Paddison, S. J.; Tuckerman, M. E. Proton Transport in Triflic Acid Hydrates Studied via Path Integral Car-Parrinello Molecular Dynamics. *J. Phys. Chem. B* **2009**, *113*, 16574−16589.

(2) Mohammed, O. F.; Pines, D.; Nibbering, E. T. J.; Pines, E. Base-induced solvent switches in acid-base reactions. *Angew. Chem.* **2007**, *119*, 1480−1483.

(3) Hynes, J. T. Physical chemistry: the peripatetic proton. *Nature* **2007**, *446*, 270−273.

(4) Rini, M.; Magnes, B.-Z.; Pines, E.; Nibbering, E. T. J. Real-time observation of bimodal proton transfer in acid-base pairs in water. *Science* **2003**, *301*, 249−352.

(5) Mohammed, O. F.; Pines, D.; Nibbering, E. T. J.; Pines, E. Base-induced solvent switches in acid-base reactions. *Angew. Chem.* **2007**, *119*, 1480−1483.

(6) Adamczyk, K.; Prémont-Schwarz, M.; Pines, D.; Pines, E.; Nibbering, E. T. J. Real-time observation of carbonic acid formation in aqueous solution. *Science* **2009**, *326*, 1690−1694.

(7) Bodi, A.; Csontos, J.; Kallay, M.; Borkar, S.; Sztaray, B. On the protonation of water. *Chem. Sci.* **2014**, *5*, 3057−3063.

(8) Laage, D.; Hynes, J. T. A Molecular Jump Mechanism of Water Reorientation. *Science* **2006**, *311*, 832−835.

(9) Elgabarty, H.; Schmieder, P.; Sebastiani, D. Unraveling the existence of dynamic water channels in light-harvesting proteins: Alpha-C-phycocyanobilin in vitro. *Chem. Sci.* **2013**, *4*, 755−763.

(10) Raghavender, U. S.; Kantharaju; Aravinda, S.; Shamala, N.; Balaram, P. Hydrophobic Peptide Channels and Encapsulated Water Wires. *J. Am. Chem. Soc.* **2010**, *132*, 1075−1086.

(11) Olschewski, M.; Knop, S.; Lindner, J.; Vöhringer, P. From Single Hydrogen Bonds to Extended Hydrogen-Bond Wires: Low-Dimensional Model Systems for Vibrational Spectroscopy of Associated Liquids. *Angew. Chem., Int. Ed.* **2013**, *52*, 9634−9654.

(12) Garczarek, F.; Gerwert, K. Functional waters in intraprotein proton transfer monitored by FTIR difference spectroscopy. *Nature* **2006**, *439*, 109−112.

(13) Heim, R.; Cubitt, A.; Tsien, R. Improved green fluorescence. *Nature* **1995**, *373*, 663−664.

(14) Chalfie, M.; Tu, Y.; Euskirchen, G.; Ward, W.; Prasher, D. Improved green fluorescence. *Science* **1994**, *263*, 802−805.

(15) Cui, Q.; Karplus, M. Is "proton wire" concerted or step-wise? A model study of proton transfers in carbonic anhydrase. *J. Phys. Chem. B* **2003**, *107*, 1071−1078.

(16) Yu, C.; Cukierman, S.; Pomés, R. Theoretical study of the structure and dynamic fluctuations of dioxolane-linked gramicidin channels. *Biophys. J.* **2003**, *84*, 816−831.

(17) Villabona-Monsalve, J. P.; Islas, R. E.; Rodríguez-Córdoba, W.; Matsika, S.; Peón, J. Ultrafast Excited State Dynamics of Allopurinol, a Modified DNA Base. *J. Phys. Chem. A* **2013**, *117*, 898−904.

(18) Dedecker, P.; de Schryver, F. C.; Hofkens, J. Fluorescent Proteins: Shine on, You Crazy Diamond. *J. Am. Chem. Soc.* **2013**, *135*, 2387−2402.

(19) Dumat, B.; Bordeau, G.; Faurel-Paul, E.; Mahuteau-Betzer, F.; Saettel, N.; Metge, G.; Fiorini-Debuisschert, C.; Charra, F.; Teulade-Fichou, M.-P. DNA Switches on the Two-Photon Efficiency of an Ultrabright Triphenylamine Fluorescent Probe Specific of AT Regions. *J. Am. Chem. Soc.* **2013**, *135*, 12697−12706.

(20) Allolio, C.; Sajadi, M.; Ernsting, N.; Sebastiani, D. An Ab Initio Microscope: Molecular Contributions to the Femtosecond Time-Dependent Fluorescence Shift of a Reichardt-Type Dye. *Angew. Chem., Int. Ed.* **2013**, *52*, 1813−1816.

(21) Kim, T. G.; Topp, M. R. Ultrafast Excited-State Deprotonation and Electron Transfer in Hydroxyquinoline Derivatives. *J. Phys. Chem. A* **2004**, *108*, 10060−10065.

(22) Gould, E.-A.; Popov, A. V.; Tolbert, L. M.; Presiado, I.; Erez, Y.; Huppert, D.; Solntsev, K. M. Excited-state proton transfer in N-methyl-6-hydroxyquinolinium salts: solvent and temperature effects. *Phys. Chem. Chem. Phys.* **2012**, *14*, 8964−8973.

(23) Veiga-Gutiérrez, M.; Brenlla, A.; Carreira Blanco, C.; Fernández, B.; Kovalenko, S. A.; Rodríguez-Prieto, F.; Mosquera, M.; Lustres, J. L. P. Dissociation of a Strong Acid in Neat Solvents: Diffusion Is Observed after Reversible Proton Ejection Inside the Solvent Shell. *J. Phys. Chem. B* **2013**, *117*, 14065−14078.

(24) Bardez, E.; Boutin, P.; Valeur, B. Photoinduced biprotonic transfer in 4-methylumbelliferone. *Chem. Phys. Lett.* **1992**, *191*, 142−148.

(25) Krauter, C. M.; Mohring, J.; Buckup, T.; Pernpointner, M.; Motzkus, M. Ultrafast branching in the excited state of coumarin and umbelliferone. *Phys. Chem. Chem. Phys.* **2013**, *15*, 17846−17861.

(26) Kwon, O.; Lee, Y.; Yoo, B. K.; Jang, D. ExcitedState Triple Proton Transfer of 7Hydroxyquinoline along a HydrogenBonded Alcohol Chain: Vibrationally Assisted Proton Tunneling. *Angew. Chem.* **2006**, *118*, 429−433.

(27) Park, S.-Y.; Lee, Y.-S.; Kwon, O.-H.; Jang, D.-J. Proton transport of water in acid-base reactions of 7-hydroxyquinoline. *Chem. Commun.* **2009**, 926−928.

(28) Park, S.-Y.; Kim, B.; Lee, Y.-S.; Kwon, O.-H.; Jang, D.-J. Triple proton transfer of excited 7-hydroxyquinoline along a hydrogen-bonded water chain in ethers: secondary solvent effect on the reaction rate. *Photochem. Photobiol. Sci.* **2009**, *8*, 1611−1617.

(29) Kwon, O.-H.; Mohammed, O. F. Water-wire catalysis in photoinduced acid-base reactions. *Phys. Chem. Chem. Phys.* **2012**, *14*, 8974−8980.

(30) Bach, A.; Hewel, J.; Leutwyler, S. Hydrogen Bonding and Intermolecular Vibrations of 6-HydroxyquinolineH2O in the S0 and S1 States. *J. Phys. Chem. A* **1998**, *102*, 10476−10485.

(31) Bach, A.; Leutwyler, S. Water-chain clusters: vibronic spectra of 7-hydroxyquinoline$(H_2O)n$, n=1−4. *Chem. Phys. Lett.* **1999**, *299*, 381−388.

(32) Bach, A.; Coussan, S.; Müller, A.; Leutwyler, S. Water-wire clusters: Vibronic spectra of 7-hydroxyquinoline$(H_2O)3$. *J. Chem. Phys.* **2000**, *113*, 9032−9043.

(33) Manca, C.; Tanner, C.; Coussan, S.; Bach, A.; Leutwyler, S. H atom transfer along an ammonia chain: tunneling and mode selectivity in 7-hydroxyquinoline.$(NH_3)3$. *J. Chem. Phys.* **2004**, *121*, 2578−2590.

(34) Tanner, C.; Manca, C.; Leutwyler, S. Exploring excited-state hydrogen atom transfer along an ammonia wire cluster: Competitive reaction paths and vibrational mode selectivity. *J. Chem. Phys.* **2005**, *122*, 204326.

(35) Tanner, C.; Thut, M.; Steinlin, A.; Manca, C.; Leutwyler, S. Excited-state hydrogen-atom transfer along solvent wires: Water molecules stop the transfer. *J. Phys. Chem. A* **2005**, *110*, 1758−1766.

(36) Tanner, C.; Manca, C.; Leutwyler, S. Probing the Threshold to H Atom Transfer Along a Hydrogen-Bonded Ammonia Wire. *Science* **2003**, *302*, 1736−1739.

(37) Liu, Y. H.; Mehata, M. S.; Liu, J. Y. Excited-state proton transfer via hydrogen-bonded acetic acid (AcOH) wire for 6-hydroxyquinoline. *J. Phys. Chem. A* **2011**, *115*, 19−24.

(38) Mehata, M. S. Proton translocation and electronic relaxation along a hydrogen-bonded molecular wire in a 6-hydroxyquinoline/acetic acid complex. *J. Phys. Chem. B* **2008**, *112*, 8383−8386.

(39) Fernández-Ramos, A.; Martínez-Nunez, E.; Vázquez, S. A.; Ríos, M. A.; Estévez, C.; Merchán, M.; Serrano-Andrés, L. Hydrogen transfer vs proton transfer in 7-hydroxy-quinoline.$(NH_3)3$: a CASSCF/CASPT2 study. *J. Phys. Chem. A* **2007**, *111*, 5907−5912.

(40) Bekçioğlu, G.; Allolio, C.; Ekimova, M.; Nibbering, E. T. J.; Sebastiani, D. Competition between excited state proton and OH-transport via a short water wire: solvent effects open the gate. *Phys. Chem. Chem. Phys.* **2014**, *16*, 13047−13051.

(41) Pérez-Lustres, J. L.; Rodriguez-Prieto, F.; Mosquera, M.; Senyushkina, T. A.; Ernsting, N. P.; Kovalenko, S. A. J. *Am. Chem. Soc.* **2007**, *129*, 5408−5418.

DOI: 10.1021/jp5121417
J. Phys. Chem. B 2015, 119, 4053−4060

(42) Konijnenberg, J.; Ekelmans, G. B.; Huizer, A. H.; Varma, C. A. G. O. Mechanism and solvent dependence of the solvent-catalysed pseudo-intramolecular proton transfer of 7-hydroxyquinoline in the first electronically excited singlet state and in the ground state of its tautomer. *J. Chem. Soc., Faraday Trans. 2* **1989**, *85*, 39−51.
(43) Bhattacharya, B.; Samanta, A. Excited-State Proton-Transfer Dynamics of 7-Hydroxyquinoline in Room Temperature Ionic Liquids. *J. Phys. Chem. B* **2008**, *112*, 10101−10106.
(44) Lim, H.; Jeong, H.; Park, S.-Y.; Lee, J. Y.; Jang, D.-J. Excited-state proton-relay dynamics of 7-hydroxyquinoline controlled by solvent reorganization in room temperature ionic liquids. *Phys. Chem. Chem. Phys.* **2012**, *14*, 218−224.
(45) Abou-Zied, O. K.; Husband, J.; Al-Lawatia, N.; Steinbrecher, T. B. Ground state spectroscopy of hydroxyquinolines: evidence for the formation of protonated species in water-rich dioxane-water mixtures. *Phys. Chem. Chem. Phys.* **2014**, *16*, 61−70.
(46) Park, S.-Y.; Lee, Y.-S.; Jang, D.-J. Ground-state proton-transfer dynamics governed by configurational optimization. *Phys. Chem. Chem. Phys.* **2011**, *13*, 3730−3736.
(47) VandeVondele, J.; Mohamed, F.; Krack, M.; Hutter, J.; Sprik, M.; Parrinello, M. The influence of temperature and density functional models in ab initio molecular dynamics simulation of liquid water. *J. Chem. Phys.* **2005**, *122*, 014515.
(48) Grimme, S. Semiempirical GGA-type density functional constructed with a long-range dispersion correction. *J. Comput. Chem.* **2006**, *27*, 1787−1799.
(49) Lippert, G.; Hutter, J.; Parrinello, M. A hybrid Gaussian and plane wave density functional scheme. *Mol. Phys.* **1997**, *92*, 477−487.
(50) Hutter, J.; Iannuzzi, M.; Schiffmann, F.; VandeVondele, J. Computer code CP2K. CP2K.org.
(51) Schäfer, A.; Huber, C.; Ahlrichs, R. Fully optimized contracted Gaussian-basis sets of triple zeta valence quality for atoms Li to Kr. *J. Chem. Phys.* **1994**, *100*, 5829−5835.
(52) Goedecker, S.; Teter, M.; Hutter, J. Separable Dual-Space Gaussian Pseudopotentials. *Phys. Rev. B* **1996**, *54*, 1703−1710.
(53) Frisch, M. J.; Trucks, G. W.; Schlegel, H. B.; Scuseria, G. E.; Robb, M. A.; Cheeseman, J. R.; Scalmani, G.; Barone, V.; Mennucci, B.; Petersson, G. A.; et al. *Gaussian 09*, revision A.02; Gaussian, Inc.: Wallingford, CT, 2009.
(54) Becke, A. D. Density-functional thermochemistry. 3. The role of exact exchange. *J. Chem. Phys.* **1993**, *8*, 5648−5652.
(55) Barone, V.; Cossi, M. Quantum calculation of molecular energies and energy gradients in solution by a conductor solvent model. *J. Phys. Chem. A* **1998**, *102*, 1995−2001.
(56) Luzar, A.; Chandler, D. Effect of Environment on Hydrogen Bond Dynamics in Liquid Water. *Phys. Rev. Lett.* **1996**, *76*, 928−931.
(57) Agmon, N. Elementary steps in excited-state proton transfer. *J. Phys. Chem. A* **2005**, *109*, 13−35.
(58) Schiffmann, C.; Sebastiani, D. Hydrogen bond networks: Structure and dynamics via first-principles spectroscopy. *Phys. Status Solidi B* **2012**, *249*, 368−375.
(59) Allolio, C.; Salas-Illanes, N.; Desmukh, Y. S.; Hansen, M. R.; Sebastiani, D. H-Bonding Competition and Clustering in Aqueous LiI. *J. Phys. Chem. B* **2013**, *117*, 9939−9946.
(60) Brehm, M.; Kirchner, B. TRAVIS - A Free Analyzer and Visualizer for Monte Carlo and Molecular Dynamics Trajectories. *J. Chem. Inf. Model.* **2011**, *51*, 2007−2023.
(61) Laage, D.; Stirnemann, G.; Hynes, J. T. Why Water Reorientation Slows without Iceberg Formation around Hydrophobic Solutes. *J. Phys. Chem. B* **2009**, *113*, 2428−2435.
(62) Laage, D.; Stirnemann, G.; Sterpone, F.; Rey, R.; Hynes, J. T. Reorientation and Allied Dynamics in Water and Aqueous Solutions. *Annu. Rev. Phys. Chem.* **2011**, *62*, 395−416.
(63) de Grotthuss, C. J. T. Sur la décomposition de l'eau et des corps qu'elle tient en dissolution á l'aide de l'électricité galvanique. *Ann. Chim.* **1806**, *58*, 54−73.
(64) Danneel, V. H. Notiz über ionengeschwindigkeiten. *Z. Elektrochem.* **1905**, *11*, 249−252.
(65) Agmon, N. The Grotthuss mechanism. *Chem. Phys. Lett.* **1995**, *244*, 456−462.
(66) Morrone, J. A.; Tuckerman, M. E. Ab initio molecular dynamics study of proton mobility in liquid methanol. *J. Chem. Phys.* **2002**, *117*, 4403−4413.
(67) Izvekov, S.; Voth, G. A. Ab initio molecular-dynamics simulation of aqueous proton solvation and transport revisited. *J. Chem. Phys.* **2005**, *123*, 44505.
(68) Geissler, P.; Dellago, C.; Chandler, D.; Hutter, J.; Parrinello, M. Ab initio analysis of proton transfer dynamics in (H2O)3H+. *Chem. Phys. Lett.* **2000**, *321*, 225−230.
(69) Hassanali, A. A.; Cuny, J.; Ceriotti, M.; Pickard, C. J.; Parrinello, M. The fuzzy quantum proton in the hydrogen chloride hydrates. *J. Am. Chem. Soc.* **2012**, *20*, 8557−8569.
(70) Hassanali, A.; Prakash, M. K.; Eshet, H.; Parrinello, M. On the recombination of hydronium and hydroxide ions in water. *Proc. Natl. Acad. Sci. U.S.A.* **2011**, *108*, 20410−20415.
(71) Hassanali, A.; Giberti, F.; Cuny, J.; Kühne, T. D.; Parrinello, M. Proton transfer through the water gossamer. *Proc. Natl. Acad. Sci. U.S.A.* **2013**, *110*, 13723−13728.
(72) Mei, H. S.; Tuckerman, M. E.; Sagnella, D. E.; Klein, M. L. Quantum Nuclear ab Initio Molecular Dynamics Study of Water Wires. *J. Phys. Chem. B* **1998**, *102*, 10446−10458.
(73) Sadeghi, R. R.; Cheng, H.-P. The dynamics of proton transfer in a water chain. *J. Chem. Phys.* **1999**, *111*, 2086−2094.
(74) Fecko, C. J.; Eaves, J. D.; Loparo, J. J.; Tokmakoff, A.; Geissler, P. L. Ultrafast Hydrogen-Bond Dynamics in the Infrared Spectroscopy of Water. *Science* **2003**, *301*, 1698−1702.
(75) Eaves, J. D.; Loparo, J. J.; Fecko, C. J.; Roberts, S. T.; Tokmakoff, A.; Geissler, P. L. Hydrogen bonds in liquid water are broken only fleetingly. *Proc. Natl. Acad. Sci. U.S.A.* **2005**, *102*, 13019−13022.
(76) Kühne, T. D.; Khaliullin, R. Z. Electronic signature of the instantaneous asymmetry in the first coordination shell of liquid water. *Nat. Commun.* **2013**, *4*, 1450.
(77) Kühne, T. D.; Khaliullin, R. Z. Nature of the Asymmetry in the Hydrogen-Bond Networks of Hexagonal Ice and Liquid Water. *J. Am. Chem. Soc.* **2014**, *136*, 3395−3399.
(78) Mohammed, O. F.; Pines, D.; Dreyer, J.; Pines, E.; Nibbering, E. T. J. Sequential proton transfer through water bridges in acid-base reactions. *Science* **2005**, *310*, 83−86.
(79) Park, S.-Y.; Jang, D.-J. Accumulated Proton-Donating Ability of Solvent Molecules in Proton Transfer. *J. Am. Chem. Soc.* **2010**, *132*, 297−302.
(80) Cox, M. J.; Timmer, R. L. A.; Bakker, H. J.; Park, S.; Agmon, N. Distance-Dependent Proton Transfer along Water Wires Connecting Acid−Base Pairs. *J. Phys. Chem. A* **2009**, *113*, 6599−6606.

DOI: 10.1021/jp5121417
J. Phys. Chem. B 2015, 119, 4053−4060

Solvation-Dependent Latency of Photoacid Dissociation and Transient IR Signatures of Protonation Dynamics

Bekçioğlu G., Hoffmann F., and Sebastiani D.

J. Phys. Chem. A **2015**, 119, 9244-9251.

DOI: http://dx.doi.org/10.1021/acs.jpca.5b05438

THE JOURNAL OF PHYSICAL CHEMISTRY A

Article

pubs.acs.org/JPCA

Solvation-Dependent Latency of Photoacid Dissociation and Transient IR Signatures of Protonation Dynamics

Gül Bekçioğlu,[†,‡] Felix Hoffmann,[‡] and Daniel Sebastiani*[,‡]

[†]Physics Department, Freie Universität Berlin, Arnimallee 14, 14195 Berlin, Germany

[‡]Institut für Chemie, Martin-Luther-Universität Halle-Wittenberg, Von-Danckelmann-Platz 4, 06120 Halle (Saale), Germany

Supporting Information

ABSTRACT: We elucidate the characteristic proton pathways and the transient infrared signatures of intermediate complexes during the first picoseconds of photoinduced protonation dynamics of a photoacid (*N*-methyl-6-hydroxyquinolinium) in aqueous solution from first-principles molecular dynamics simulations. Our results indicate that the typical latency time between photoexcitation and proton dissociation ranges from 1 ps to longer time time scales (∼100 ps). The rate-limiting step for the actual dissociation of the proton into the solvent is the solvation structure of the first accepting water molecule. The nature of the proton pathway in water (stepwise or concerted) is not unique but determined by the coordination number of the accepting water molecules along the hydrogen bond chain. We find a characteristic uncommon infrared mode at ∼1300 cm^{-1} of the transient photobase-Eigen cation complex immediately after photodissociation that we predict to be observable experimentally in time-resolved IR spectroscopy. A broad continuous absorption band from 1500 to 2000 cm^{-1} arises from the acidic proton imminently before dissociation.

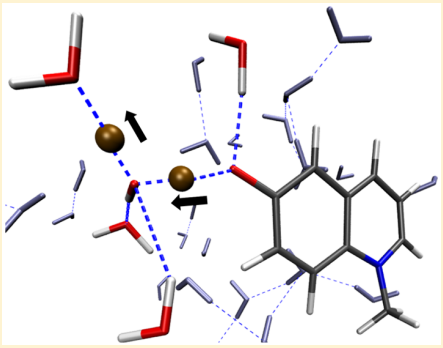

1. INTRODUCTION

Photoinduced proton transfer (PT) in aqueous solutions is of fundamental interest in a large variety of chemical and biological processes such as the storage of energy and radiation-induced damage of DNA.[1−6] In aqueous solution, where the hydrogen bond interactions are very extended, PT can be very complex due to the structural rearrangement of water molecules. Water-mediated photoinduced PT may happen in a concerted or stepwise mechanism from the acid to the base over large distances.[7−14] Central in these mechanisms is the key role of the surrounding solvent shells, which facilitate the PT by fluctuations of the hydrogen bond network or breaking and formation of hydrogen bonds. These fluctuations are also considered to play important roles for the stabilization of reaction products and are involved in the reaction coordinate for proton dissociation mechanisms. However, the number of theoretical and experimental studies investigating these mechanisms have remained moderate.[15]

Ultrafast studies of photoinduced proton dissociation in aqueous solutions have utilized the class of organic molecules called photoacids.[16−23] A suitable molecule for this purpose is the "super" photoacid *N*-methyl-6-hydroxyquinolinium cation (6MQc) depicted in Figure 1. 6MQc exhibits a large p*K* drop from 7.2 in the ground state to −7 in the excited state (6MQc*).[24−29] Pérez-Lustres et al. reported proton dissociation kinetics of 6MQc* in aqueous solution with time-resolved fluorescence studies. It was shown that the excited-state proton dissociation barrier is 2 kJ mol^{-1}.[29] However, the fundamental question of how the intra- and intermolecular factors affect photoacidity and PT rate still remain under debate.[29−32]

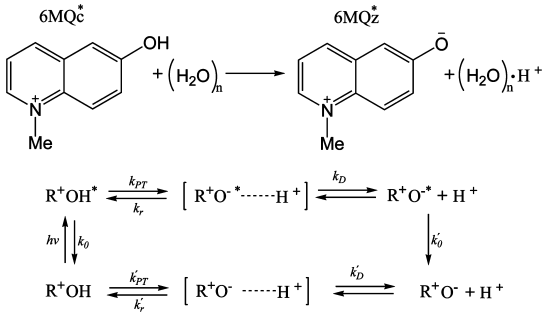

Figure 1. Excited-state PT and relaxation processes of excited 6MQc species.

The seminal work by Eigen and Weller[33−35] has frequently been utilized to discuss acid dissociation reactions and rates. The general kinetic approach, based on this model for acid−base reactions in aqueous solutions, consists of two step process: (a) The acidic proton is transferred from the acid to a solvent molecule after photoexcitation to form a contact ion pair, and (b) subsequently the contact ion pair is separated by diffusion (see Figure 1).[36] However, many details of the PT

Received: June 8, 2015
Revised: August 17, 2015
Published: August 17, 2015

DOI: 10.1021/acs.jpca.5b05438
J. Phys. Chem. A 2015, 119, 9244−9251

from photoacid to water remain elusive, for example, the structure and stability of the contact ion pair formed by the photoacid and the hydrated proton, as well as the hydrogen bonding network around a solvated photosensitive probe molecule.

In the present paper, we are particularly interested in the role water plays in promoting photoinduced acid dissociation and in the hydrogen bonding rearrangements that accompany it. We put the chromophore in the triplet state (T_1) for the simulation of the excited-state dynamics; that is, the first excited state (S_1) was approximated with a T_1 surface. Our T_1 description is motivated by an increased numerical stability and a reduced computational effort compared to a real S_1 calculation. Of course, this protocol represents an approximation of the experimental situation. However, we have extensively benchmarked the validity of this approximation for 6MQc (see Supporting Information) and 6MQz[37] and verified that it correctly represents the most significant physical intramolecular interactions. The central question addressed in this work is the direct determination of elementary dissociation steps that lead to the final product: a fully solvated proton and a deprotonated photoacid. We computed IR spectra to follow the individual steps during the dissociation processes that occur in a time range of femtoseconds to tens of picoseconds.[38]

2. COMPUTATIONAL DETAILS

The molecular dynamics simulations were staged in a cubic, periodic box with a side length of 16.06 Å hosting one 6MQc molecule and 130 H_2O molecules at a density of d = 1.00 g/cm^3. First, we run 20 ps trajectory in NVT ensemble at 350 K. Then, we started five independent ground-state simulations ∼10 ps each in NVE ensemble from the previous simulation. From these NVE trajectories, 16 excited-state trajectories were started. We run these excited-state trajectories for ∼10 ps if no PT occurred and for ∼20 ps if PT occurred. For all calculations, we used GPW[39] scheme as implemented in the CP2K[40] software package. The BLYP[41,42] functional with a TZVP valence basis set, Goedecker[43] potentials, and a 350 Ry plane-wave cutoff was employed. With the increase in temperature we hope to balance overstructuring effects, found in water simulations at lower temperature.[44,45] For the very same reason, we used DFT-D2 dispersion corrections.[46] The simulation temperature of 350 K corresponds to a physical temperature of 300−320 K. For the ground-state simulations, we used restricted Kohn−Sham density functional theory (DFT) and a time step of 1 fs, while for the excited-state simulations, we used unrestricted Kohn−Sham DFT, a multiplicity of 3, and a time step of 1 fs. All protons in the system were given the mass of deuterium to allow us to use 1 fs time step.

All DFT-based static electronic structure and normal mode calculations were performed by using Gaussian 09 program.[47] The conventional DFT and normal mode calculations using hybrid exchange-correlation functional B3LYP[48] and BLYP[41,42] functional were perfomed within the presence of the CPCM model.[49] The basis set was TZVP for these calculations.

To study IR absorptions of the system, the electron density was subjected on the fly to a localization procedure employing maximally localized Wannier functions during the excited-state simulations.[50] Wannier centers can be regarded as centers of charge density of electron pairs in local orbitals and allow therefore for a chemical intuitive interpretation in terms of bonds and lone pairs. Moreover, it is well-known that this approach readily enables the calculation of molecular dipole moments in a condensed-phase system.[51] For instance, the dipole moment of molecule I can be calculated via

$$\mu_I = \mu_I^{\mathrm{el}} + \mu_I^{\mathrm{nuclei}} \tag{1}$$

$$= -2e \sum_{i\in I} \mathbf{r}_i^{\mathrm{Wannier}} + e \sum_{j\in I} n_{j,\mathrm{val}} \cdot \mathbf{r}_j^{\mathrm{nuclei}} \tag{2}$$

with μ_I^{el} and μ_I^{nuclei} designating the electronic and nuclei contribution to the molecular dipole moment. $\mathbf{r}_i^{\mathrm{Wannier}}$ and $\mathbf{r}_j^{\mathrm{nuclei}}$ are the positions of the Wannier centers and the ions, respectively; e denotes the elementary charge, and $n_{j,\mathrm{val}}$ indicates the number of valence electrons of the respective atom at position $\mathbf{r}_j^{\mathrm{nuclei}}$.

This, in turn, allows one to compute the classical dipole autocorrelation function, whose Fourier transform is related to the product of absorption coefficient per unit length and refractive index, that is, the IR spectrum, via

$$\alpha(\omega)n(\omega) = F(\omega) \int_{-\infty}^{\infty} \mathrm{d}t \langle \mu(0)\mu(t)\rangle \mathrm{e}^{-i\omega t} \tag{3}$$

where $F(\omega) = \beta\,\omega^2/6Vc\varepsilon_0$ and μ are the total dipole moment of the simulation box. Note that eq 3 is the classical approximation of the formerly quantum dipole autocorrelation function taking into account the harmonic quantum correction factor.[52]

IR absorptions for 6MQc, 6MQc*, and 6MQz* are calculated based on a spectral decomposition approach utilizing the cross-correlation function of the total dipole moment with the molecular dipole moment of the solute.[38]

Accordingly, eq 3 is modified by replacing the dipole autocorrelation function with the cross-correlation function yielding

$$I_I(\omega) = F(\omega) \int_{-\infty}^{\infty} \mathrm{d}t \langle \mu(0)\mu_I(t)\rangle \mathrm{e}^{-i\omega t} \tag{4}$$

with the molecular dipole moment μ_I, where the index I denotes the set of atoms belonging to 6MQc, 6MQc*, and 6MQz*, respectively. For further analysis of the IR absorptions, we calculated the Fourier transform of the C−O bond autocorrelation function defined as

$$P_{\mathrm{CO}}(\omega) = \int_{-\infty}^{\infty} \mathrm{d}t \langle \dot{d}_{\mathrm{CO}}(0)\dot{d}_{\mathrm{CO}}(t)\rangle \mathrm{e}^{-i\omega t} \tag{5}$$

where $\dot{d}_{\mathrm{CO}}$ is the time-derivative of the C−O bond distance. The resulting peaks should be approximately at positions of the normal modes where this bond vibration contributes, assuming that this vibration is not highly anharmonic. Shifts in $P_{\mathrm{CO}}(\omega)$ can be regarded as a measure of bond strength variations, where a blue shift corresponds to a strengthening and a red shift corresponds to a weakening of the C−O bond.

3. RESULTS

3.1. Aqueous Solvation of 6MQc. Five of 16 trajectories showed successful proton dissociation within 1−2 ps after photoexcitation. To verify the effects of solvent reorganization upon excitation, we computed the radial distribution functions (RDFs) of 6MQc-oxygen and water hydrogen atoms $g(\mathrm{O}_{\mathrm{6MQc}}\text{-}\mathrm{D}_{\mathrm{w}})$, and the acidic 6MQc-hydrogen and water oxygen atoms $g(\mathrm{D}_{\mathrm{6MQc}}\text{-}\mathrm{O}_{\mathrm{w}})$ from the ground- and excited-state trajectories. Our findings are reported in Figure 2. First, we observe a small peak arising at 1.1 Å $g(\mathrm{D}_{\mathrm{6MQc}}\text{-}\mathrm{O}_{\mathrm{w}})$ in the excited state due to the RO···D···OD_2 bond; that is, the proton is partly shared by

DOI: 10.1021/acs.jpca.5b05438
J. Phys. Chem. A 2015, 119, 9244−9251

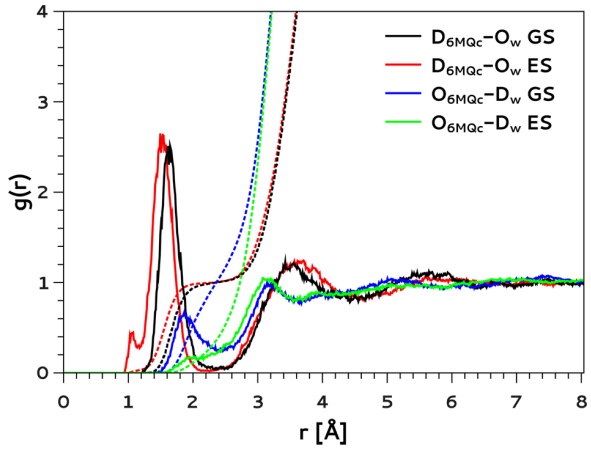

Figure 2. RDFs of 6MQc-hydrogen and water-oxygen atoms (D_{6MQc}-O_w) and 6MQc-oxygen and water-hydrogen atoms the water molecules (O_{6MQc}-D_w) are in the ground (black and blue) and the excited (red and green) states, respectively. The integration number of the distribution functions (dashed lines) is also reported.

the two oxygen atoms constituting the first stage of acid dissociation. The apparent shifts of the first peak and the following minimum at 2.25 Å in the excited state indicate that the ROD···OD_2 bond shortens by 0.2 Å due to the acidic proton becoming more positively charged and more disposed to H-bonding upon excitation. Further, strengthening of H-bonding does not seem to extend beyond the first solvation shell. Instead, one observes an increased order as represented by increase in the coordination number in the second solvation shell. The integration over the peaks at 3.6 Å in the $g(D_{6MQc}$-$O_w)$ corresponds to 8.8 and 9.4 water molecules in the ground and excited state, respectively. On the other hand, $g(O_{6MQc}$-$D_w)$ shows the effect of elongation of the hydrogen bond to the 6MQc*-oxygen due to the charge rearrangements around the lone pairs of the oxygen atom in the excited state (see Supporting Information and Figure 4a). However, this bond reforms as a subsequent solvent stabilization of the product, completing the PT reaction. Similar findings have been already discussed in experimental studies in terms of solvatochromic shifts (a blue shift) in the steady-state fluorescence spectra of undissociated photoacids.[53] Complementary to these findings, we found no obvious structural differences between the contact ion pair geometry for the successful and unsuccessful proton dissociation (see Supporting Information).

Another interesting observation in our simulations is the back-protonation reaction (geminate reaction) following the proton dissociation from 6MQc* after ∼10 ps photodissociation. It was shown by time-resolved fluorescence experiments that the deviation from an exponential fluorescence decay results in the existence of the back-protonation reaction in the excited state.[54] Such a process, in turn, gives rise to a multiexponential time-resolved fluorescence decay, rather than a purely exponential form.

3.2. Proton Dissociation Mechanism. We now augment our analysis by elucidating the intake of protons into the H-bond network to provide a more complete picture of the long-range PT reaction in bulk aqueous solution. This fundamental interest lies at the heart of the microscopic character of the structure and mobility of liquid water. The basic PT reaction can be explained by a von Grotthuss mechanism involving a sequential hopping mechanism of protons to neighboring water molecules.[4−6] However, the actual PT reaction has been discussed to be either concerted or sequential in the bulk solution.[55,56] Although both mechanisms are plausible, concerted proton charge rearrangements occur in an assembly of several water molecules linked by hydrogen bonds for smaller PT distances, and a change into sequential transfer then is anticipated when the PT distance increases. From an atomistic point of view, the question of sequential or concerted PT can be translated into the comparison of typical lifetimes of particular protonation states in relation to the lifetimes of the involved hydrogen bonds.[55]

To verify the relationship between concerted and sequential PT mechanism, we employ, in Figure 3, the RDFs of the proton

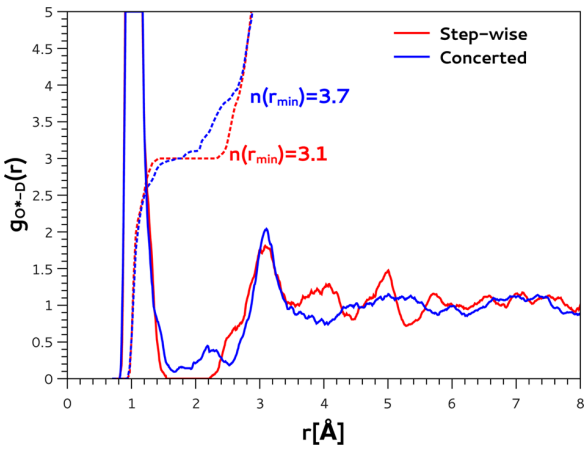

Figure 3. RDF and coordination numbers of a proton acceptor oxygen atom and the hydrogen atom of water molecules (O*-D) corresponding to the concerted mechanism (blue line and dashed line, respectively), and sequential hopping mechanism (red line and dashed line, respectively). The coordination numbers ($n(r_{min})$) are computed by characterizing the minimum of the first solvation shell of $g_{O^*-D}(r)$.

acceptor oxygen atom (denoted O*) and the hydrogen atoms of water molecules. The RDFs ($g_{O^*-D}(r)$) are computed by averaging over 20 fs intervals before a successful PT occurs. We interpret $g_{O^*-D}(r_{min})$ up to the relevant minimum of the first solvation peaks, characterized by a radius r_{min}. Note here that the peaks in $g_{O-D}(r)$ below 2.45 Å are generally considered as an indicator of a H-bond in bulk water. Figure 3 shows that in the case of a stepwise mechanism, there is a broad first peak with a minimum at 1.65 Å due to the strong O−D···O* bond. There is no further contribution from the other first solvation shell water molecules. However, in the case of the concerted mechanism, the O* atom accepts one additional H-bond, which is responsible for the small peak at 2.2 Å. This additional peak, in turn, requires an extension of the coordination radius to r_{min} = 2.45 Å. In this regard, the actual character of the PT reaction depends on how the proton is taken into the H-bonded network: an increase in the coordination number changes the character of the PT event. In particular, when the initial coordination of the acceptor oxygen is ∼fourfold ($n(r_{min})$ = 3.7 in Figure 3), the concerted PT is favored in this mechanism, and the subsequent PT occurs within ∼0.1−0.5 ps. However, if the accepting water molecule is initially only threefold coordinated ($n(r_{min})$ = 3.1 in Figure 3), it will hold the proton for typically ∼1−5 ps, which eventually yields a stepwise migration. Figure 4 illustrates the difference between these

DOI: 10.1021/acs.jpca.5b05438
J. Phys. Chem. A 2015, 119, 9244−9251

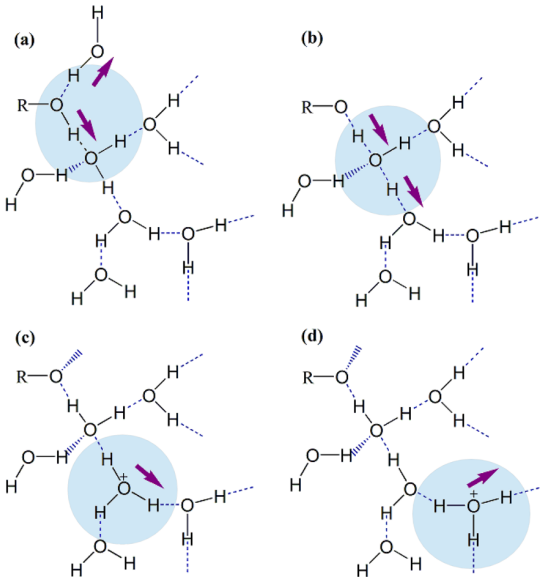

Figure 4. Scheme illustrating the PT mechanisms of 6MQc* in aqueous solution. (a) Formation of contact ion pair and elongation of hydrogen bond between 6MQc-oxygen atom and water molecule; (b) transient structures involving the concerted motion of two protons; (c, d) a threefold coordinated water molecule holding the excess proton.

mechanisms regarding the coordination number. Our findings suggest that the concerted PT occurs when the proton receiving oxygen (O*) accepts a hydrogen bond from another water molecule before PT takes place. In contrast, the stepwise transfer involves a single O−H bond breaking/forming at a time. Our trajectories reveal that 60% of the proton dissociation reactions are concerted and that 40% occur in a stepwise manner. In all cases, the concerted events start from a fourfold coordinated water, and the stepwise process start from a threefold coordinated water.

A similar observation on the nature of the proton pathway in water was also reported by Tuckermann et al.[55] concerning the PT mechanism of the hydrated proton and in the study of Maurer et al.[57] by investigating the ultrafast acid dissociation and acid−base neutralization reactions. Therefore, we conclude that an ultrafast (subps, i.e. concerted) long-distance proton separation from the acid requires an initial fourfold coordination of all involved water molecules.

3.3. Infrared Spectral Shifts. We computed the IR spectra of 6MQc, 6MQc*, and 6MQz* to investigate effects of electronic excitation and proton dissociation on the IR absorptions. The spectra of 6MQc and 6MQc* are presented in Figure 5, corresponding to negative and early positive delay times in transient IR measurements. Figure 5 reveals slight red shifts by ∼30 cm^{-1} of most absorption peaks within 1000 to 1500 cm^{-1} (mainly C−C and C−O stretching) upon electronic excitation (cf. Supporting Information for mode assignment). More precisely, peaks at 1000, 1180, 1355, 1420, and 1510 cm^{-1} in the ground-state spectrum are shifted to 970, 1150, 1330, 1390, and 1480 cm^{-1} in the excited-state spectrum. These red shifts are in line with the fact that C−C bonds in the aromatic rings get lengthened on average, as shown in Figure S7 in the Supporting Information. Conversely, a shortening of C−C bonds perpendicular to the direction of largest extension of 6MQc was observed consistent with findings of Agmon et al., who found a roughly alternating pattern of lengthening and

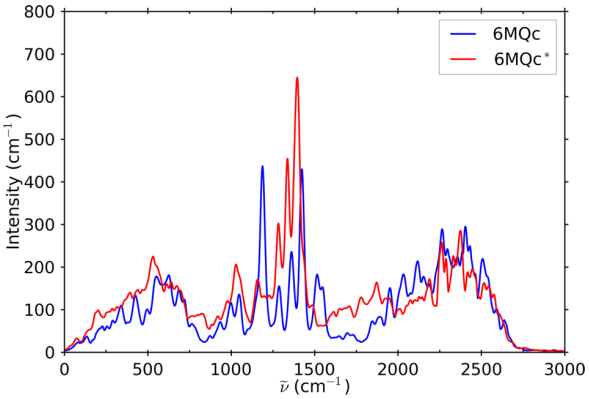

Figure 5. Infrared spectra for 6MQc and 6MQc* averaged over five and 11 trajectories, respectively. The simulation length was 10 ps in each case.

shortening for 2-naphtol upon excitation to S_1.[58] A quantitative comparison of these shifts with transient IR measurements, however, is not directly possible due to the use of the T_1 state in our case.

Further, Figure 5 reveals intensity changes upon electronic excitation at 1180 cm^{-1} and between 1280 and 1400 cm^{-1}, where intensity is decreased in the former and increased in the latter case. In contrast, only minor changes appear in the C−D stretching range ∼2300 to 2700 cm^{-1} and for frequencies below 700 cm^{-1}.

Most interesting, however, the O−D stretching vibration gives rise to a continuous absorption band between 1500 and 2000 cm^{-1} in the excited-state spectrum caused by the flat potential of the O−D···OD_2 hydrogen bond. Additionally, the chromophore O−D bond is drastically weakened in the excited state, whereas the hydrogen bond to the coordinating water is strengthened, as shown in Figure 2. Note here that, in contrast to spectra obtained from molecular dynamics (MD) simulations that allow for a fully anharmonic treatment, this continuous absorption band cannot be obtained from normal mode calculations, even with perturbative corrections to the harmonic frequencies, where it always appears as a localized peak (see Supporting Information).

In Figure 5, the corresponding O−D absorption in the ground state coalesces with the peak between 1800 and 2800 cm^{-1} (mainly C−D vibrations) as suggested by normal mode calculations with explicit water molecules (see Supporting Information). Therefore, the O−D absorption is located at higher frequencies than in the excited-state MD spectrum. The O−D stretching absorption in the normal mode spectrum without consideration of explicit solvent molecules is expectedly red-shifted due to the absence of hydrogen bonds to the solvent.

To attain further evidence that the continuous absorption band between 1500 and 2000 cm^{-1} in the excited-state spectrum is indeed due to the O−D stretching vibration, we computed the IR spectrum for 6MQc* based on dipole moments calculated from atomic Hirshfeld charges,[59] leaving the trajectories unchanged. In Figure 6, it can be seen that the continuous absorption vanishes by setting the partial charge on the acidic hydrogen atom to zero, suggesting that the broad absorption band is dominated by the dynamics of this atom, which is comparably loosely bonded in 6MQc*. However, note here that peak patterns and intensities differ slightly compared

DOI: 10.1021/acs.jpca.5b05438
J. Phys. Chem. A 2015, 119, 9244−9251

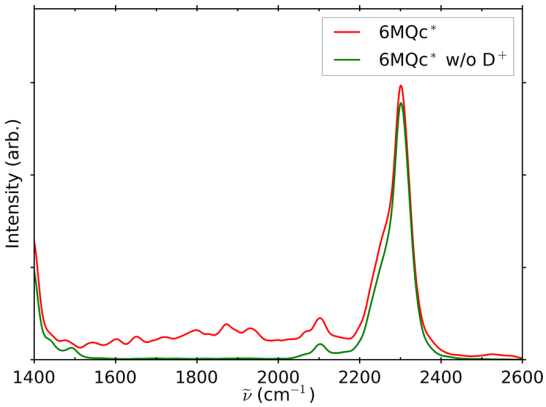

Figure 6. Infrared spectrum between 1400 and 2600 cm^{-1} computed from atomic Hirshfeld charges based on trajectories of 6MQc*. The spectrum labeled 6MQc* refers to the total chromophore, whereas the spectrum 6MQc* without D^+ was obtained by setting the partial charge on the proton to zero.

to Figure 5, since the spectrum based on Hirshfeld charges misses electronic polarization effects and the underlying dipole moments differ compared to the Wannier center approach. Our findings are consistent with previous studies that ascribed absorption band to the motion of the weakly bonded proton in contact ion pairs and hydrated protons of ground-state acids as well as photoacids.[60−62] Moreover, experimental results for the photoacid 8-hydroxy-1,3,6-pyrenetrisulfonic trisodium salt (HPTS) suggest that the amplitude of the continuous absorption peak is largest at the onset of proton dissociation, while the contribution of the hydronium ion, which is not included in our spectral calculations, contributes with a smaller amplitude.[62]

Having discussed the impact of electronic excitation at the onset of proton dissociation, we now focus on the question how the IR absorptions change after the proton is released to a solvating water molecule. Figure 7 shows the spectrum of 6MQc* and 6MQz*, where the inset presents the absorptions between 1200 and 1500 cm^{-1}. The most significant change in IR absorption upon proton dissociation is the depletion of the continuous absorption band between 1500 and 2300 cm^{-1}, providing further evidence that this feature originates from the acidic proton. Moreover, the bands between 1250 and 1550

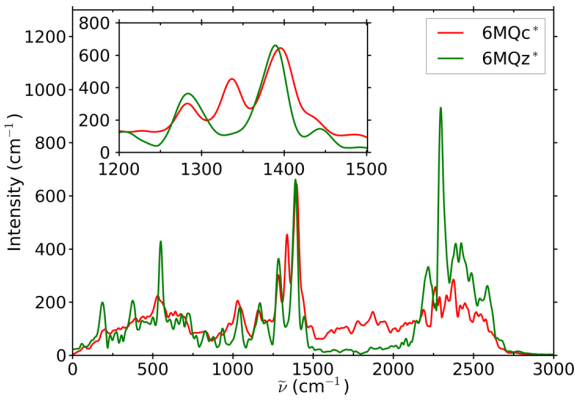

Figure 7. Infrared spectrum of 6MQc* and 6MQz* averaged over 11 and four trajectories, respecticvely. For 6MQz*, spectra were computed only within the time range of complete dissociation.

cm^{-1}, originating mostly from bond stretching vibrations of the ring atoms and the C−O bond, are significantly affected when proton dissociation occurs. In particular, the peak at 1330 cm^{-1} is absent in the spectrum of the dissociated photoacid (cf. inset Figure 7). Notably, this feature is consistent for all single-trajectory spectra of the protonated and deprotonated chromophore, based on which we calculated the average spectra shown in Figure 7. Further, we analyzed this feature by means of normal-mode analysis (see Supporting Information) and found that the variation in peak patterns is due to changes of normal modes dominated by C−C stretching vibrations of the ring atoms, as illustrated in Figures S10 and S12 in the Supporting Information. In the region between 1250 and 1550 cm^{-1}, we observe an altered peak structure in the normal mode spectra due to the absence of the proton. In the MD spectra, the stretching vibrations between 1200 and 1500 cm^{-1} (labeled with D-I in the Supporting Information) are most distinct, and therefore we can regard the vanishing of the absorption at 1330 cm^{-1} as a consequence of these altered stretching modes. Note here that these unique assignments cannot be further resolved in our MD spectra due to the limited sampling time. This observation in turn suggests that the peak pattern around 1330 cm^{-1} might serve as a marker for the protonation state in transient IR experiments. A similar feature has already been discussed in an experimental study of HPTS.[61] Further, we investigated this feature for 6MQz* and 6MQz by means of normal mode calculations (see Supporting Information). We found that the peak pattern around 1330 cm^{-1} differs for 6MQz compared to 6MQz* and therefore regard this marker to be characteristic for the excited 6MQz* only.

In addition, we investigated the effect of the proton dissociation on the C−O bond vibration. To this end, we computed the Fourier transform of the velocity auto-correlation function according to eq 5, which is depicted in Figure 8. We

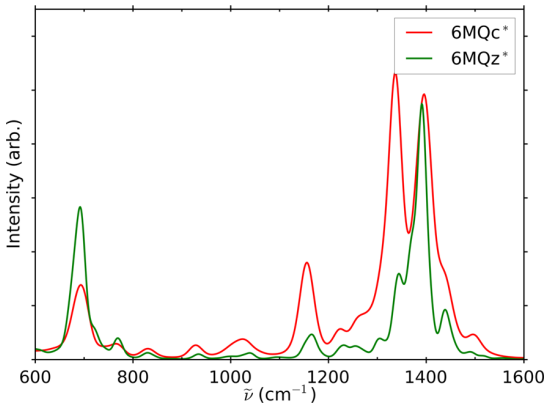

Figure 8. Fourier transform of the C−O bond distance velocity autocorrelation of 6MQc* and 6MQz* averaged over 11 and four trajectories, respectively.

note that the vibrational frequency of the C−O bond cannot easily be extracted from the MD spectrum in Figure 7 due to the superposition of bands caused by other vibrations. In contrast, bands in the power spectrum of the distance auto-correlation function should approximately occur at positions of the respective normal modes, where the C−O bond vibration contributes. A comparison of the power spectra of 6MQc* and 6MQz* in Figure 8 reveals that only slight frequency shifts occur upon proton dissociation. However, the average distance

DOI: 10.1021/acs.jpca.5b05438
J. Phys. Chem. A 2015, 119, 9244−9251

of the C−O bond in the simulations gets shortened by ∼0.05 Å as shown in Figure S7 in the Supporting Information. The fact that this shortening does not lead to a blue shift of the vibrational frequencies as in the normal modes spectra can be explained by the strong hydrogen bonding of water molecules to the partially negatively charged oxygen, which restrict the motions of the C−O moiety (cf. normal mode H at 1413 cm^{-1} for 6MQ* and mode I at 1445 cm^{-1} for 6MQz* in Supporting Information).

Regarding the intensities of the individual (single-trajectory based) power spectra underlying the averaged spectrum in Figure 8, we found strong variations for the two protonation states and for each trajectory suggesting a complex dependency on the actual atomic conformation and hydrogen bonding configuration around the hydroxyl group.

As mentioned before, all presented MD spectra are computed based on simulations of fully deuterated samples. A comparison with experimental data obtained from non-deuterated samples therefore must take into account isotope effects. We investigated absorptions for nondeuterated samples by comparing the normal mode spectra for 6MQc, 6MQc*, and 6MQz* (see Supporting Information) and found blue shifts of absorptions above 2000 cm^{-1} by ∼1000 cm^{-1} in the nondeuterated case. This suggests that C−H stretch and O−H stretch vibrations will be observed at higher frequencies in experimental spectra of nondeuterated samples. We found no overall absorption shift below 2000 cm^{-1} but instead observed a reordering of normal modes resulting in a distinct absorption pattern compared to the deuterated case (cf. Supporting Information). As a consequence, the possible marker at 1300 cm^{-1} indicative of 6MQc* or 6MQz* in the deuterated case will be different for nondeuterated samples. The normal mode spectra in the latter case feature as well an altered but distinct peak pattern upon proton release in the fingerprint region below 2000 cm^{-1}. Therefore, this regime might be suited as a marker region in transient IR measurements of the non-deuterated chromophore similarly as in the deuterated case.

4. CONCLUSION

We have investigated the photoinduced proton dissociation processes from the super photoacid 6MQc in aqueous solution from first-principles MD simulations. Besides the prototypical red-shifting effects of excitation on the intramolecular modes of the solute, we find a broad IR absorption line from 1500 to 2000 cm^{-1} after excitation and before deprotonation of the acid. Our analysis shows that this line is due to the loose bonding situation of the acidic proton just before dissociation. Right afterward, we observe the transient formation of a contact ion pair with a characteristic IR signature of ∼1300 cm^{-1} that we predict to be observable experimentally, provided a sufficient time resolution (femtosecond) is possible.

We also investigated hydrogen bond rearrangements upon electronic excitation and structural differences between the contact ion pair geometries. In these terms, the rate-limiting step for the proton transfer to the first solvent molecule is found not to be the initial acid−water barrier but instead the solvation structure around the first water molecule. Further, we elucidate the nature of the Grotthuss-style dissociation/transport pathway in terms of stepwise mechanism versus concerted motion across multiple water molecules. Our findings indicate that the concerted mechanism is possible if the accepting water molecule is fourfold coordinated. In the case of only threefold coordination, the character of the protonation pathway is rather stepwise.

Our results will support the experimental assignment of transient IR signatures from femtosecond spectroscopy, providing an atomistic interpretation of the underlying short-lived molecular conformations of such photoacids. The findings on the coordination dependence of the nature of the proton pathway illustrate why the long-standing debate on the stepwise versus concerted mechanisms will prevail, as there both mechanisms can coexist for flexible coordination states of the involved water molecules.

■ ASSOCIATED CONTENT

Supporting Information

The Supporting Information is available free of charge on the ACS Publications website at DOI: 10.1021/acs.jpca.5b05438.

Computational details and validation of the ab initio molecular dynamics simulations (computed properties in the S_0, S_1, and T_1 states), as well as the assignment of IR resonances of the compounds. (PDF)

■ AUTHOR INFORMATION

Corresponding Author

*E-mail: daniel.sebastiani@chemie.uni-halle.de.

Notes

The authors declare no competing financial interest.

■ ACKNOWLEDGMENTS

We are grateful to Dr. E. T. J. Nibbering (Max-Born-Institut, Berlin) for useful discussions and suggestions and for reading an early version of the manuscript. Computing infrastructure was provided by the KIT-Hochleistungsrechner of the Steinbuch Centre for Computing. This work was supported by Leibniz Graduate School of Molecular Biophysics Berlin, Kekulé-Stipendium, and German Research Foundation (DFG) under Grant No. SE 1008/11-1.

■ REFERENCES

(1) Bort, G.; Gallavardin, T.; Ogden, D.; Dalko, P. I. From One-Photon to Two-Photon Probes: "Caged" Compounds, Actuators, and Photoswitches. *Angew. Chem., Int. Ed.* **2013**, *52*, 4526−4537.

(2) Bucher, D. B.; Schlueter, A.; Carell, T.; Zinth, W. Watson-Crick Base Pairing Controls Excited-State Decay in Natural DNA. *Angew. Chem., Int. Ed.* **2014**, *53*, 11366−11369.

(3) Conrad, K. S.; Manahan, C. C.; Crane, B. R. Photochemistry of Flavoprotein Light Sensors. *Nat. Chem. Biol.* **2014**, *10*, 801−809.

(4) Morrone, J. A.; Tuckerman, M. E. Ab Initio Molecular Dynamics Study of Proton Mobility in Liquid Methanol. *J. Chem. Phys.* **2002**, *117*, 4403−4413.

(5) Izvekov, S.; Voth, G. A. Ab Initio Molecular-Dynamics Simulation of Aqueous Proton Solvation and Transport Revisited. *J. Chem. Phys.* **2005**, *123*, 044505.

(6) Geissler, P.; Dellago, C.; Chandler, D.; Hutter, J.; Parrinello, M. Ab Initio Analysis of Proton Transfer Dynamics in (H2O)3H+. *Chem. Phys. Lett.* **2000**, *321*, 225−230.

(7) Hassanali, A. A.; Cuny, J.; Ceriotti, M.; Pickard, C. J.; Parrinello, M. The Fuzzy Quantum Proton in the Hydrogen Chloride Hydrates. *J. Am. Chem. Soc.* **2012**, *134*, 8557−8569.

(8) Tuckerman, M. E.; Marx, D.; Klein, M. L.; Parrinello, M. On the Quantum Nature of the Shared Proton in Hydrogen Bonds. *Science* **1997**, *275*, 817−820.

(9) Ludueña, G. A.; Sebastiani, D. Possibility of Coherent Delocalized Nuclear Quantum States of Protons in Li_2NH. *J. Phys. Chem. Lett.* **2010**, *1*, 3214−3218.

DOI: 10.1021/acs.jpca.5b05438
J. Phys. Chem. A 2015, 119, 9244−9251

(10) Ceriotti, M.; Bussi, G.; Parrinello, M. Nuclear Quantum Effects in Solids Using a Colored-Noise Thermostat. *Phys. Rev. Lett.* **2009**, *103*, 030603.
(11) Ceriotti, M.; Miceli, G.; Pietropaolo, A.; Colognesi, D.; Nale, A.; Catti, M.; Bernasconi, M.; Parrinello, M. Nuclear Quantum Effects in Ab Initio Dynamics: Theory and Experiments for Lithium Imide. *Phys. Rev. B: Condens. Matter Mater. Phys.* **2010**, *82*, 174306.
(12) Benoit, M.; Marx, D. The Shapes of Protons in Hydrogen Bonds Depend on the Bond Length. *ChemPhysChem* **2005**, *6*, 1738−1741.
(13) Marx, D.; Benoit, M.; Parrinello, M. Tunnelling and Zero-Point Motion in High-Pressure Ice. *Nature* **1998**, *392*, 258−261.
(14) Tuckerman, M. E.; Marx, D. Heavy-Atom Skeleton Quantization and Proton Tunneling in "Intermediate-Barrier" Hydrogen Bonds. *Phys. Rev. Lett.* **2001**, *86*, 4946−4949.
(15) Leiderman, P.; Genosar, L.; Huppert, D. Excited-State Proton Transfer: Indication of Three Steps in the Dissociation and Recombination Process. *J. Phys. Chem. A* **2005**, *109*, 5965−5977.
(16) Bekçioğlu, G.; Allolio, C.; Ekimova, M.; Nibbering, E. T. J.; Sebastiani, D. Competition between Excited State Proton and OH-Transport via a Short Water Wire: Solvent Effects Open the Gate. *Phys. Chem. Chem. Phys.* **2014**, *16*, 13047−13051.
(17) Bekçioğlu, G.; Allolio, C.; Sebastiani, D. Water Wires in Aqueous Solutions from First-Principles Calculations. *J. Phys. Chem. B* **2015**, *119*, 4053−4060.
(18) Rini, M.; Magnes, B.-Z.; Pines, E.; Nibbering, E. T. J. Real-Time Observation of Bimodal Proton Transfer in Acid-Base Pairs in Water. *Science* **2003**, *301*, 249−352.
(19) Mohammed, O. F.; Pines, D.; Dreyer, J.; Pines, E.; Nibbering, E. T. J. Sequential Proton Transfer Through Water Bridges in Acid-Base Reactions. *Science* **2005**, *310*, 83−86.
(20) Adamczyk, K.; Prémont-Schwarz, M.; Pines, D.; Pines, E.; Nibbering, E. T. J. Real-Time Observation of Carbonic Acid Formation in Aqueous Solution. *Science* **2009**, *326*, 1690−1694.
(21) Allolio, C.; Sajadi, M.; Ernsting, N.; Sebastiani, D. An Ab Initio Microscope: Molecular Contributions to the Femtosecond Time-Dependent Fluorescence Shift of a Reichardt-Type Dye. *Angew. Chem., Int. Ed.* **2013**, *52*, 1813−1816.
(22) Guglielmi, M.; Tavernelli, I.; Rothlisberger, U. On the Proton Transfer Mechanism in Ammonia-Bridged 7-Hydroxyquinoline: A TDDFT Molecular Dynamics Study. *Phys. Chem. Chem. Phys.* **2009**, *11*, 4549−4555.
(23) Xia, S.-H.; Xie, B.-B.; Fang, Q.; Cui, G.; Thiel, W. Excited-State Intramolecular Proton Transfer to Carbon Atoms: Nonadiabatic Surface-Hopping Dynamics Simulations. *Phys. Chem. Chem. Phys.* **2015**, *17*, 9687−9697.
(24) Veiga-Gutiérrez, M.; Brenlla, A.; Carreira Blanco, C.; Fernández, B.; Kovalenko, S. A.; Rodríguez-Prieto, F.; Mosquera, M.; Lustres, J. L. P. Dissociation of a Strong Acid in Neat Solvents: Diffusion is Observed after Reversible Proton Ejection inside the Solvent Shell. *J. Phys. Chem. B* **2013**, *117*, 14065−14078.
(25) Gould, E.-A.; Popov, A. V.; Tolbert, L. M.; Presiado, I.; Erez, Y.; Huppert, D.; Solntsev, K. M. Excited-State Proton Transfer in N-Methyl-6-Hydroxyquinolinium Salts: Solvent and Temperature Effects. *Phys. Chem. Chem. Phys.* **2012**, *14*, 8964−8973.
(26) Popov, A. V.; Gould, E.-A.; Salvitti, M. A.; Hernandez, R.; Solntsev, K. M. Diffusional Effects on the Reversible Excited-State Proton Transfer. From Experiments to Brownian Dynamics Simulations. *Phys. Chem. Chem. Phys.* **2011**, *13*, 14914−14927.
(27) Bardez, E.; Boutin, P.; Valeur, B. Photoinduced Biprotonic Transfer in 4-Methylumbelliferone. *Chem. Phys. Lett.* **1992**, *191*, 142−148.
(28) Bardez, E.; Chatelain, A.; Larrey, B.; Valeur, B. Photoinduced Coupled Proton and Electron Transfers. 1. 6-Hydroxyquinoline. *J. Phys. Chem.* **1994**, *98*, 2357−2366.
(29) Pérez-Lustres, J. L.; Rodriguez-Prieto, F.; Mosquera, M.; Senyushkina, T. A.; Ernsting, N. P.; Kovalenko, S. A. Ultrafast Proton Transfer to Solvent: Molecularity and Intermediates from Solvation- and Diffusion-Controlled Regimes. *J. Am. Chem. Soc.* **2007**, *129*, 5408−5418.
(30) Poizat, O.; Bardez, E.; Buntinx, G.; Alain, V. Picosecond Dynamics of the Photoexcited 6-Methoxyquinoline and 6-Hydroxyquinoline Molecules in Solution. *J. Phys. Chem. A* **2004**, *108*, 1873−1880.
(31) Bardez, E.; Fedorov, A.; Berberan-Santos, M. N.; Martinho, J. M. G. Photoinduced Coupled Proton and Electron Transfers. 2. 7-Hydroxyquinolinium Ion. *J. Phys. Chem. A* **1999**, *103*, 4131−4136.
(32) Kim, T. G.; Topp, M. R. Ultrafast Excited-State Deprotonation and Electron Transfer in Hydroxyquinoline Derivatives. *J. Phys. Chem. A* **2004**, *108*, 10060−10065.
(33) Eigen, M. Proton Transfer, Acid-Base Catalysis and Enzymatic Hydrolysis. *Angew. Chem., Int. Ed. Engl.* **1964**, *3*, 1−19.
(34) Weller, A. Fast Reactions of Excited Molecules. *Prog. React. Kinet.* **1961**, *1*, 187.
(35) Eigen, M.; Kruse, W.; Maeyer, L. D. Über den Zustand des Protons (Hydroniumions) in Wässriger Lösung. *Prog. React. Kinet.* **1964**, *2*, 285.
(36) Thomas, V.; Maurer, P.; Iftimie, R. On the Formation of Proton-Shared and Contact Ion Pair Forms during the Dissociation of Moderately Strong Acids: An Ab Initio Molecular Dynamics Investigation. *J. Phys. Chem. B* **2010**, *114*, 8147−8155.
(37) Allolio, C.; Sebastiani, D. Approaches to the Solvation of the Molecular Probe N-Methyl-6-Quinolone in its Excited State. *Phys. Chem. Chem. Phys.* **2011**, *13*, 16395−16403.
(38) Iftimie, R.; Tuckerman, M. E. Decomposing Total IR Spectra of Aqueous Systems into Solute and Solvent Contributions: A Computational Approach Using Maximally Localized Wannier Orbitals. *J. Chem. Phys.* **2005**, *122*, 214508.
(39) Lippert, G.; Hutter, J.; Parrinello, M. A Hybrid Gaussian and Plane Wave Density Functional Scheme. *Mol. Phys.* **1997**, *92*, 477−487.
(40) Hutter, J.; Iannuzzi, M.; Schiffmann, F.; VandeVondele, J. CP2K: Atomistic Simulations of Condensed Matter Systems. *WIREs. Comput. Mol. Sci.* **2014**, *4*, 15−25.
(41) Becke, A. D. Density-Functional Exchange-Energy Approximation with Correct Asymptotic Behavior. *Phys. Rev. A: At., Mol., Opt. Phys.* **1988**, *38*, 3098.
(42) Lee, C.; Yang, W.; Parr, R. G. Development of the Colle-Salvetti Correlation-Energy Formula into a Functional of the Electron-Density. *Phys. Rev. B: Condens. Matter Mater. Phys.* **1988**, *37*, 785−789.
(43) Goedecker, S.; Teter, M.; Hutter, J. Separable Dual-Space Gaussian Pseudopotentials. *Phys. Rev. B: Condens. Matter Mater. Phys.* **1996**, *54*, 1703−1710.
(44) VandeVondele, J.; Mohamed, F.; Krack, M.; Hutter, J.; Sprik, M.; Parrinello, M. The Influence of Temperature and Density Functional Models in Ab Initio Molecular Dynamics Simulation of Liquid Water. *J. Chem. Phys.* **2005**, *122*, 014515.
(45) Sorenson, J. M.; Hura, G.; Glaeser, R. M.; Head-Gordon, T. What Can X-ray Scattering Tell Us about the Radial Distribution Functions of Water? *J. Chem. Phys.* **2000**, *113*, 9149−9161.
(46) Grimme, S. Semiempirical GGA-Type Density Functional Constructed with a Long-Range Dispersion Correction. *J. Comput. Chem.* **2006**, *27*, 1787−1799.
(47) Frisch, M. J. et al. *Computer code Gaussian 09;* Gaussian, Inc: Wallingford, CT, 2011.
(48) Becke, A. D. Density-Functional Thermochemistry. 3. The Role of Exact Exchange. *J. Chem. Phys.* **1993**, *98*, 5648−5652.
(49) Barone, V.; Cossi, M. Quantum Calculation of Molecular Energies and Energy Gradients in Solution by a Conductor Solvent Model. *J. Phys. Chem. A* **1998**, *102*, 1995−2001.
(50) Silvestrelli, P. L.; Parrinello, M. Water Molecule Dipole in the Gas and in the Liquid Phase. *Phys. Rev. Lett.* **1999**, *82*, 3308.
(51) Thomas, M.; Brehm, M.; Fligg, R.; Vöhringer, P.; Kirchner, B. Computing Vibrational Spectra from Ab Initio Molecular Dynamics. *Phys. Chem. Chem. Phys.* **2013**, *15*, 6608−22.
(52) Ramirez, R.; Lopez-Ciudad, T.; Kumar P, P.; Marx, D. Quantum Corrections to Classical Time-Correlation Functions: Hydrogen Bonding and Anharmonic Floppy Modes. *J. Chem. Phys.* **2004**, *121*, 3973.

DOI: 10.1021/acs.jpca.5b05438
J. Phys. Chem. A 2015, 119, 9244−9251

(53) Agmon, N. Elementary Steps in Excited-State Proton Transfer. *J. Phys. Chem. A* **2005**, *109*, 13−35.
(54) Pines, E.; Huppert, D. Geminate Recombination Proton-Transfer Reactions. *Chem. Phys. Lett.* **1986**, *126*, 88−91.
(55) Berkelbach, T. C.; Lee, H.-S.; Tuckerman, M. E. Concerted Hydrogen-Bond Dynamics in the Transport Mechanism of the Hydrated Proton: A First-Principles Molecular Dynamics Study. *Phys. Rev. Lett.* **2009**, *103*, 238302.
(56) Tuckerman, M. E.; Laasonen, K.; Sprik, M.; Parrinello, M. Ab Initio Molecular Dynamics Simulation of the Solvation and Transport of H3O+ and OH- Ions in Water. *J. Phys. Chem.* **1995**, *99*, 5749−5752.
(57) Maurer, P.; Thomas, V.; Iftimie, R. A Computational Study of Ultrafast Acid Dissociation and Acid-Base Neutralization Reactions. II. The Relationship between the Coordination State of Solvent Molecules and Concerted versus Sequential Acid Dissociation. *J. Chem. Phys.* **2011**, *134*, 094505.
(58) Agmon, N.; Rettig, W.; Groth, C. Electronic Determinants of Photoacidity in Cyanonaphthols. *J. Am. Chem. Soc.* **2002**, *124*, 1089.
(59) Hirshfeld, F. L. Bonded-Atom Fragments for Describing Molecular Charge Densities. *Theor. Chem. Acc.* **1977**, *44*, 129−138.
(60) Iftimie, R.; Tuckerman, M. E. The Molecular Origin of the "Continuous" Infrared Absorption in Aqueous Solutions of Acids: A Computational Approach. *Angew. Chem., Int. Ed.* **2006**, *45*, 1144−7.
(61) Cox, M. J.; Timmer, R. L. A.; Bakker, H. J.; Park, S.; Agmon, N. Distance-Dependent Proton Transfer along Water Wires Connecting Acid-Base Pairs. *J. Phys. Chem. A* **2009**, *113*, 6599−6606.
(62) Siwick, B. J.; Bakker, H. J. On the Role of Water in Intermolecular Proton Transfer Reactions. *J. Am. Chem. Soc.* **2007**, *129*, 13412−13420.

DOI: 10.1021/acs.jpca.5b05438
J. Phys. Chem. A 2015, 119, 9244−9251

Dynamical Dimension to the Hofmeister Series: Insights from First-Principles Simulations

Bekçioğlu-Neff G, Allolio C., Desmukh Y. S., Hansen M. R., and Sebastiani D.

ChemPhysChem **2016**, 17, 1166-1173.

DOI: http://dx.doi.org/10.1002/cphc.201501150

ChemPubSoc Europe

DOI: 10.1002/cphc.201501150

CHEMPHYSCHEM Articles

Dynamical Dimension to the Hofmeister Series: Insights from First-Principles Simulations

Gül Bekçioğlu-Neff,[a, b] Christoph Allolio,[c] Yogesh S. Desmukh,[d, e] Michael Ryan Hansen,[f] and Daniel Sebastiani*[a]

A systematic characterization of the competing kosmotropic and chaotropic effects of a series of divalent salts on the aqueous H-bonding structure by means of first-principles molecular dynamics simulations is presented. The structural properties are quantified by means of experimental and computed ^{1}H NMR chemical shifts, whereby the local environments of cations and anions can be discriminated. Complementary to the well-established structural features, a dynamical aspect is added to the concept of kosmotropes and chaotropes. The H-bond dynamics, quantified in terms of the H-bonding autocorrelation functions, shows a good correlation with the structural kosmotropic and chaotropic modifications, which are commonly referred to as the Hofmeister series. The considerably enhanced (reduced) fluctuations of the H-bonding network in the hydration shells around the anions (cations) are a complementary dynamical dimension to the concept of kosmotropic/chaotropic behavior of solvated ions.

1. Introduction

Solvated ions are of vital importance in many technological and biochemical systems, and they are among the decisive chemical components, since the interaction between ions and water plays a key role in the specific structure and functions of proteins.[1,2] They are involved in a wide range of biological and inorganic processes, such as the aggregation of proteins and nucleic acids,[3,4] enzyme catalysis,[5–9] and numerous cellular signaling processes.[10] Ions can have distinctive abilities to salt out or salt in proteins in aqueous solutions, which is known as the Hofmeister effect.

Classification of the influences of ions on the water H-bond network has been crucial to experimental (ultrafast) IR and NMR spectroscopy, terahertz and neutron scattering, and also theoretical studies.[11–29] Despite their importance, many details of the hydration properties of ions remain elusive on the molecular level. An important question is whether the effect of ions on dynamical properties of H-bonds is limited to their first hydration shell, or whether there are long-range structural and dynamical effects. Recent studies showed the existence of long-range effects on water molecules beyond the first hydration shells in $MgSO_4$ and Na_2SO_4 solutions by using a combination of femtosecond time-resolved IR and dielectric relaxation spectroscopy.[30] On the other hand, earlier studies revealed opposite findings regarding the H-bonding dynamics of water.[31,32] Therefore, such electrolyte solutions combining a kosmotropic cation, that is, one that reinforces the H-bond network, with a chaotropic anion having the opposite effect can be used to determine cooperative effects, which involve a complex interplay between the ions.

Herein, we combined ab initio molecular dynamics (MD) simulations and NMR experiments to study the effect of divalent salts on extended aqueous H-bonded networks. Specifically, we studied aqueous solvated ions of $MgCl_2$, $CaCl_2$, MgI_2, and CaI_2 at an intermediate concentration of 2 M. We elucidated the influence of these specific combinations of cations and anions on the H-bonding dynamics and determined the impact of a given ion on the dynamics of the water molecules in the first hydration shell with respect to the situation in bulk water.

Computational Details

We carried out ab initio MD simulations on five boxes of side length 11.84 Å containing 55 water molecules for pure-water simulation, 53 water molecules and two ion pairs for $CaCl_2$, 52 water

[a] G. Bekçioğlu-Neff, Prof. D. Sebastiani
Institut für Chemie, Martin-Luther-Universität Halle-Wittenberg
Von-Danckelmann-Platz 4, 06120 Halle (Saale) (Germany)
E-mail: daniel.sebastiani@chemie.uni-halle.de

[b] G. Bekçioğlu-Neff
Physics Department, Freie Universität Berlin
Arnimallee 14, 14195 Berlin (Germany)

[c] C. Allolio
Institute of Organic Chemistry and Biochemistry
Academy of Sciences of the Czech Republic
Flemingovo nám 2, 16610 Prague 6 (Czech Republic)

[d] Y. S. Desmukh
Department of Biobased Materials, Maastricht University
P.O. Box 616, 6200MD, Maastricht (The Netherlands)

[e] Y. S. Desmukh
Wavin Technology and Innovation
P.O. Box 173, 8000 AD Zwolle, (The Netherlands)

[f] M. R. Hansen
Institut für Physikalische Chemie
Westfälische Wilhelms-Universität Münster
Corrensstrasse 28/30, Münster (Germany)

Supporting Information for this article can be found under http://dx.doi.org/10.1002/cphc.201501150.

molecules and two ion pairs for $MgCl_2$, 48 water molecules and two ion pairs for CaI_2, and 49 water molecules and two ion pairs for MgI_2. The densities of the boxes were set to 0.99 for pure water, 1.12 for $MgCl_2$, 1.45 for CaI_2, and 1.43 $g\,cm^{-3}$ for MgI_2 according to a polynomial fit from literature values at 25 °C.[33,34] For the particular simulation of $CaCl_2$ solution, we used different experimental reference density[35] of 1.17 $g\,cm^{-3}$ due to the incorrect parameters in our main literature baseline. Firstly, we pre-equilibrated the solutions of $MgCl_2$, CaI_2, and MgI_2 using the DZVP basis set for about 10 ps. Secondly, we ran our ab initio MD simulations of each system in the NVT ensemble for about 40 picoseconds. All systems were thermostated by using a CSVR thermostat[36] with a time constant of 100 fs at a temperature of 350 K. The computational temperature was set to this value to compensate for overstructuring of water at the BLYP-D level of theory.[37] The simulations were performed with deuterated water in 1 fs MD time steps with the initial guess provided by the always-stable predictor–corrector extrapolation method at each MD step.[38,39] Despite this, our nomenclature uses "H" rather than "D" referring to the deuteron.

For all ab initio simulations, we used the GPW[40] scheme with QUICKSTEP module[41] as implemented in the CP2K[42] software package. The BLYP-D[43] dispersion-corrected density functional[44,45] with a triple-ζ augmented basis set for hydrogen and oxygen (TZV2PX), a quadruple-ζ (QZV2P) basis set for the cations, and a DZVP-MOLOPT basis set for the anions,[46] Goedecker[47] potentials, and a 600 Rydberg plane-wave cutoff were employed. In addition, we used the DFT-D2 dispersion corrections[43] to account for dispersion effects.

For the calculations of NMR chemical shifts, we used IGLO-III (Perdew, Burke, and Ernzerhof/Individual Gauge for (each) Localized Molecular Orbital) basis set[48] without pseudopotentials for protons, and DZVP-MOLOPT[46] basis set with GTH[49,47] pseudopotentials for the rest of the atoms. The GAPW[50] method with a 320 Ry cutoff was employed. For each system, the simulated NMR chemical shifts were computed by averaging over 30 snapshots extracted randomly from the last several picoseconds of ab initio MD trajectories. The cumulative NMR spectrum of each system was then computed over more than 2000 instantaneous ^1H chemical shifts.

2. Results and Discussion

2.1. Ion–Water Coordination

We calculated ion–oxygen radial distribution functions (RDFs) of $CaCl_2$, $MgCl_2$, CaI_2, and MgI_2 solutions (Figure 1). The coordination numbers of each ion, obtained as the integrated value of the RDF up to the first minimum, are also included. In agreement with earlier first-principles MD results,[11,25,28,51] Mg^{2+} exhibits a very rigidly structured first hydration shell with six water molecules in an octahedral arrangement, with a highly depleted area between the first and second peaks. In comparison, Ca^{2+} has a more flexible first hydration shell than Mg^{2+} with seven water molecules and a more distant first minimum at 3.25 Å (2.95 Å for Mg^{2+}). Note that, as the positive charge of Ca^{2+} is more diffuse than that of Mg^{2+}, the height of the first peak of $g_{Ca^{2+}-O}(r)$ is lower.

A similar difference is observed for the dynamics of the first hydration shells of cations. No exchange of water molecules

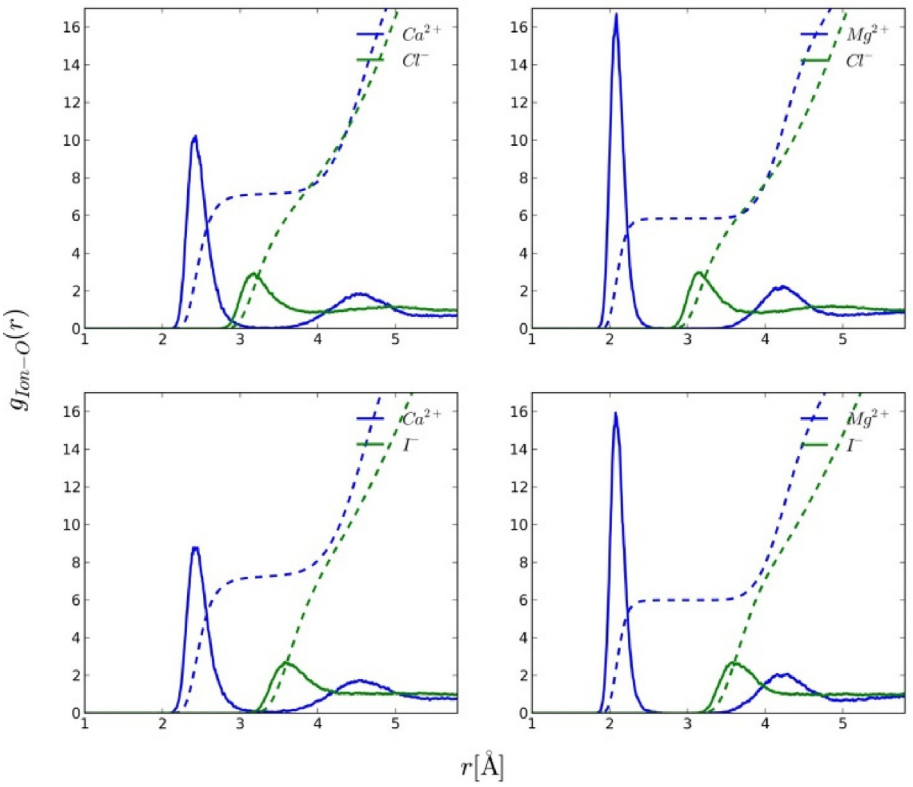

Figure 1. Radial hydration structure of ion–oxygen atom pairs. The $g_{Ion-O}(r)$ functions are shown as solid lines and the coordination numbers $N_{Ion-O}(r)$ as dashed lines.

between the first and the second hydration shells of Mg^{2+} is observed within the simulation time of 40 ps. In contrast, we noticed several exchanges of water molecules between the first and the second hydration shells of Ca^{2+}.

Concerning the solvation structure around the anions, variation of the cation has no noticeable effect on the first hydration shells of Cl^- and I^- at 2 M concentration. As expected, the position of the first hydration minimum is shifted to longer distances as the ionic radius of the anion increases. The first hydration minima were found to be 4.0 and 4.5 Å for Cl^- and I^-, respectively. Unlike the Cl^-–O RDF, there is no peak for a second hydration shell in the I^-–O RDF (see Supporting Information). The incomplete separation of the peaks, in combination with the fact that they are broader and lower, leads to the conclusion that the hydration shell of I^- is rather unstructured and diffuse. On the other hand, the Cl^- ion can apparently fit into the water structure relatively easily without causing major perturbation. These results show good agreement with previous X-ray diffraction and molecular dynamics studies regarding the position of the first peaks in the RDFs.[11,15,17,28,52]

2.2. Water–Water Coordination

A comparison of the O–O RDFs of $CaCl_2$, $MgCl_2$, CaI_2, MgI_2 solutions with that of pure water is shown in Figure 2. The RDFs evidence a chaotropic effect on the water–water H-bond network. The first peaks are lower for all electrolyte solutions except for the MgI_2 solution. The minimum of the first peak is shifted by about 0.2 and 0.4 Å to longer distances in $MgCl_2$/MgI_2 and $CaCl_2$/CaI_2 solutions, respectively. In all solutions, the structure of the second hydration shell, which is well defined in pure water, is strongly suppressed. This reduction of local ordering is of course partially due to the high concentration of ions, but our simulations indicate a surprisingly exclusive dependence on the cation species; replacing I^- with Cl^- makes no virtually difference.

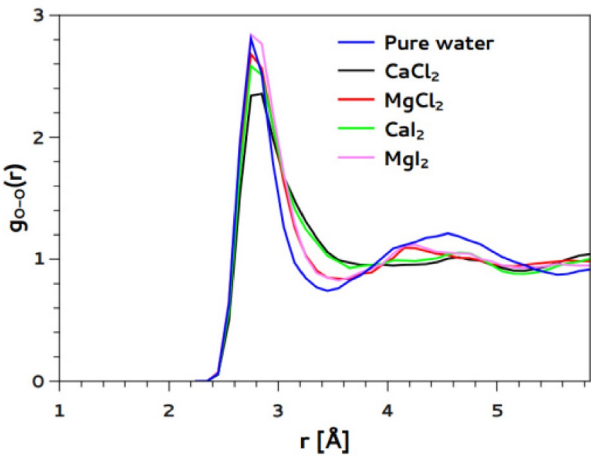

Figure 2. Comparison of the $g_{O\text{-}O}(r)$ radial distribution functions of $CaCl_2$, $MgCl_2$, CaI_2, and MgI_2 with that of pure water.

2.3. Directionality of Ion–Water Interaction

The ion–water RDFs show important structural information, but they ignore the intramolecular structure of water molecules. Therefore, we now augment our analysis by elucidating specific orientational preferences of the water molecules in the first hydration shell of the ions. We describe the orientation by using the angle θ between the bisector vector of a water molecule and the ion–oxygen vector (see Figure 3). The angular distributions of $\cos\theta$ for all ions with their solvating water molecules are shown in Figure 3.

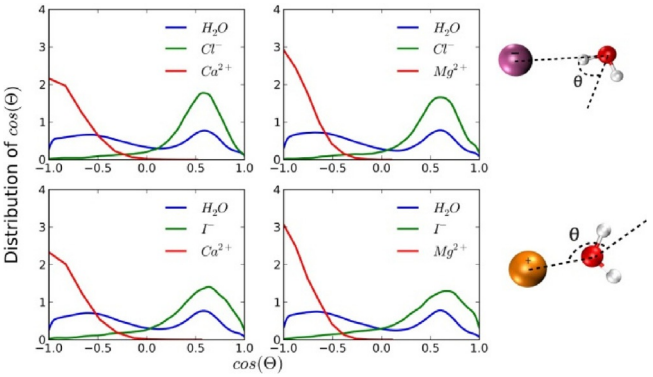

Figure 3. Distribution of $\cos\theta$ for the water molecules in the first hydration shells of Mg^{2+}, Ca^{2+}, Cl^-, and I^- and the water molecules in these systems.

The distributions of the angular orientations of the water molecules around Mg^{2+} and Ca^{2+} ions show a peak located at $\cos\theta = -1$. The narrower angle distributions of the Mg^{2+} ion confirm the expected enhanced structural ordering. The distribution functions for the anions are quite different. For the solutions containing Cl^- ions, the distributions strongly peak around 55°. On the other hand, the peaks for the I^--containing solutions are slightly broader and centered around 50°. These findings demonstrate that anion–water H-bonds are almost linearly aligned.

In the case of water–water angular distribution functions in electrolyte solutions, we observe two peaks, because water molecules act as H-bond donor or acceptor. These angular distributions are nearly identical. Compared to pure water, these angular distribution functions behave slightly differently (see Supporting Information).

2.4. NMR Chemical Shifts

We measured the dependence of (experimental) ^{1}H NMR chemical shifts on salt concentration for $CaCl_2$, $MgCl_2$, CaI_2, MgI_2, $CaBr_2$, and $MgBr_2$ solutions. The trends in chemical shifts can be seen as an indicator for the degree of ordering of the H-bonded network, and thus as a quantification of the respective kosmotropic/chaotropic effects.[53] Figure 4 shows that the ^{1}H NMR chemical shifts of all electrolyte solutions vary linearly with concentration. The variation of the slopes of the change of the ^{1}H NMR chemical shifts reflect the different magnitudes

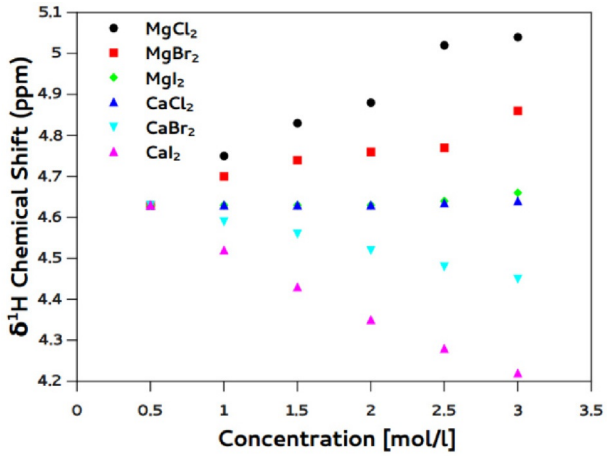

Figure 4. Experimental ^{1}H chemical shifts for different aqueous solutions of divalent cations at concentrations from 1 to 3 mol L^{-1}.

to which the respective ions affect the H-bond strength. The net effect of the salts ranges from strongly kosmotropic ($MgCl_2$) and moderately kosmotropic ($MgBr_2$) through neutral ($CaCl_2$ and MgI_2) to moderately chaotropic ($CaBr_2$) and strongly chaotropic (CaI_2). In line with the common understanding of the Hofmeister series, these findings show that the kosmotropic/chaotropic effects of the individual ions almost exactly cancel for $CaCl_2$ and MgI_2. The chaotropic effect increases from Cl^- to Br^- to I^-, and the kosmotropic strength increases from Ca^{2+} to Mg^{2+}.

We computed ^{1}H NMR chemical shifts from our ab initio simulations. Figure 5 shows a comparison between our calculated ^{1}H NMR chemical shifts and experimental data. In absolute values, the ^{1}H NMR chemical shifts of the 2 M solutions differ only slightly from that of pure water. This reflects partial cancellation of the kosmotropic and chaotropic effects of cations

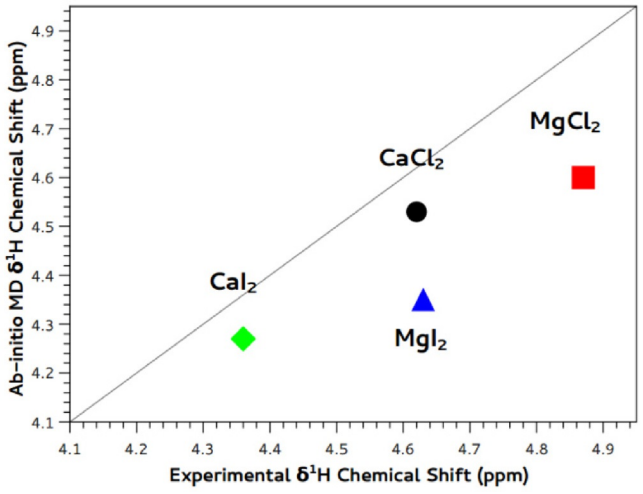

Figure 5. ^{1}H NMR chemical shifts for $CaCl_2$, $MgCl_2$, CaI_2, and MgI_2 at 2 M concentration. Calculated NMR shifts are referenced to the H_2O trajectory which in turn is set to the experimental shift of 4.65 ppm. The linear line is meant as a guide to the eye.

and anions, respectively. Nevertheless, the correlation between ab initio calculations and experimental data is fairly good, with residual deviations on the order of 0.1–0.2 ppm. These differences in turn represent systematic (DFT, finite-size effects) and statistical (length of MD simulations, trajectory sampling frequencies) errors inherent to our approach.

To quantify the individual effects of the cations and anions, we decomposed the ^{1}H NMR chemical shifts into contributions from the first hydration shells of halide and divalent metal ions, as well as the fraction of bulk water molecules in our simulations (Figure 6). The effect on the chemical shielding is more pronounced in the case of I^- than Cl^-. This confirms the more strongly chaotropic character of Cl^- compared to I^-, and the increased kosmotropic character of Ca^{2+} compared to Mg^{2+}. Thus, our findings are a direct microscopic elucidation of the Hofmeister effect in terms of H-bonding.

2.5. Dynamics

Besides the structural aspects, a very important, yet often overlooked, feature induced by solvated ions is the molecular dynamics. On the molecular level, the translational and rotational motion of water molecules is heavily affected by the modified H-bond network. This can cause changes in the behavior of water that are of equal importance to the structural variations. To quantify this effect on the level of the H-bonding network, we introduce an autocorrelation function for the H-bonds [Eq. (1)]:

$$C_{HB}(t) \equiv \frac{1}{\langle h(t_0)\rangle^2}\langle h(t_0+t)\cdot h(t_0)\rangle \qquad (1)$$

where $\langle\ldots\rangle$ denotes an average over all H-bonds[54,55] and $h(t)$ is a vector, the elements $h_i(t)$ of which are the dimension of the number of possible H-bonds. The H-bond vector component $h_i(t)$ is unity if water molecule i is H-bonded to the reference molecule at time t, and is zero otherwise. $C_{HB}(t)$ represents the conditional probability that an H-bond remains intact for a time t, given it was intact at time t_0. In our definition, we ignore transient breaking of a H-bond shorter than a tolerance time of 25 fs. Two water molecules are considered to be H-bonded if the distance between their oxygen atoms is less than 3.5 Å, and the O^2-O^1-H^1 angle is less than $\pi/6$. To examine the characteristics of H-bonds in the vicinity of the ionic species, we separately considered the modifications that operate in the first hydration shells. The boundaries of these shells were defined by the positions of the first minimum of the ion–oxygen RDFs.

Figure 7 shows the lifetime of the inter-water H-bonds in the entire system, and inter-water H-bonds of the water molecules in the first hydration shells of cations (illustrated in the inset of Figure 7) are compared with the lifetime of pure water H-bonds. With the exception of $CaCl_2$, the lifetime of inter-water H-bonds of the water molecules in the first hydration shells of the cations decay more slowly than the lifetime of pure-water H-bonds due to the stabilizing cationic field. As expected, this effect is more visible for the water molecules of

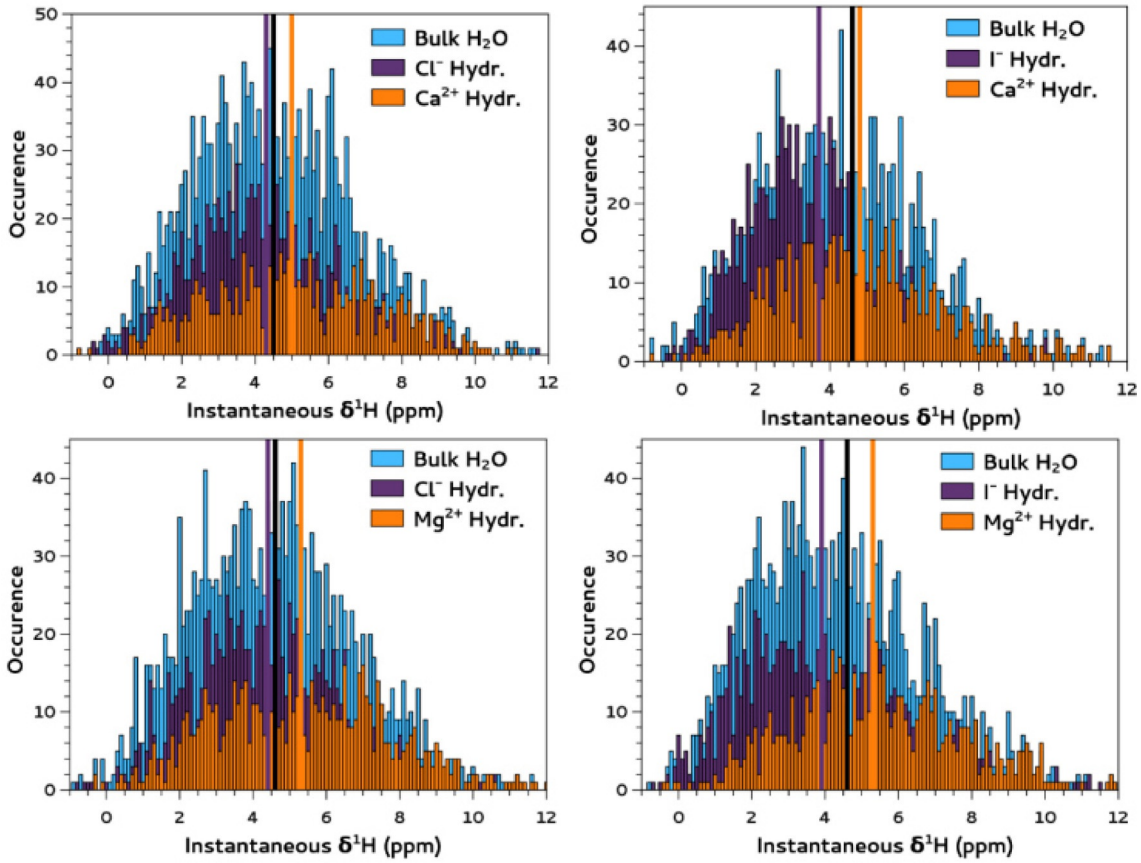

Figure 6. ^{1}H NMR chemical-shift distribution for hydrating water and bulk water in the $CaCl_2$, $MgCl_2$, CaI_2, and MgI_2 solutions. The average for pure water is marked with a black bar, and the chemical-shift average of water molecules of hydration of the cation and anion are marked with the orange and purple bars, respectively. We used cation–oxygen and anion–hydrogen cutoffs from the RDFs.

the first hydration shell of Mg^{2+}. Additionally, the H-bond lifetime decays show a biexponential character, which may reflect slowing down of the H-bond rearrangements around cations.[56] On the other hand, the impact of ions on the overall water H-bond relaxation is ion-specific and does not follow a simple trend. This complexity originates from the existence of solvent-shared ion pairs in which the cation and anion share a fraction of their hydration shells. In 2 M solutions, the overlap of hydration shells can force the formation of various stable and transient water-shared ion pairs. Although the solvent-shared ion pairs were found to be stable on the 3–4 ps timescale, it is impossible to infer their relative stability from the present simulations due to the simulation protocol parameters or system-size dependencies. Nevertheless, our simulations reveal the presence of such relatively stable clusters, especially in the solutions containing the large I^- ion, that is, CaI_2 and MgI_2, in which the mobility of these shared water molecules is restricted. We found the same effect in our previous study of LiI solutions.[57] In this respect, depending on the stability of these clusters, overall water H-bond relaxation can be faster or slower relative to that of pure water. Interestingly, even though the lifetime of the I^-–water H-bond is shorter, the dynamical structure-breaking effect of I^- on the overall H-bond dynamics of water is not as strong as that of Cl^- in all solutions (see Figure 8). This mobility restriction is due to the larger accessible surface of I^- to water molecules compared to Cl^-. Despite its larger size, the I^- ion has only one more water molecule than Cl^- in the first hydration shell (see Supporting Information). Therefore, I^--induced structural changes in the water H-bond network (see Figure 2) increase the presence of water molecules in interstitial positions. As a result, these interstitial water molecules form stronger H-bonds with the water molecules of the first cation hydration shell, which in turn further lowers the overall mobility of water molecules. Such a mechanism is consistent with slowdown of H-bond rearrangements induced by hydrophobic sites of other solutes.[58–61]

We also investigated how the dynamics of the water molecules around anions is affected by the counterions. To this end, we defined the residence-time autocorrelation function $C_{Wres}(t)$ by using Equation (2):

$$C_{Wres}(t) \equiv \frac{1}{\langle w(t_0)\rangle^2}\langle w(t_0+t)\cdot w(t_0)\rangle \qquad (2)$$

where $\langle\ldots\rangle$ denotes an average over all water molecules in the first hydration shell of a given ion. For the vector function $w(t)$, $w_i(t)=1$ if water molecule i is in the first hydration shell of a given ion at time t, and otherwise 0. We again tolerated tem-

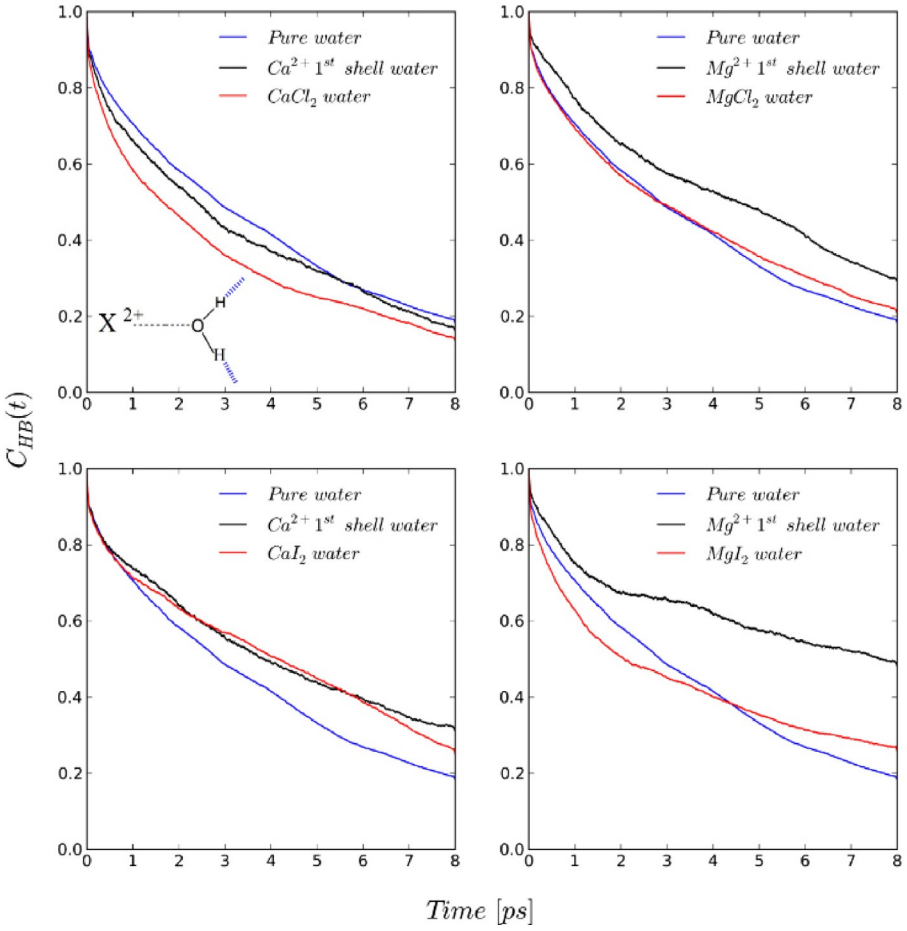

Figure 7. H-bond autocorrelation functions of water molecules in the $CaCl_2$, $MgCl_2$, CaI_2, and MgI_2 solutions, in the first hydration shells of cations, and for pure water.

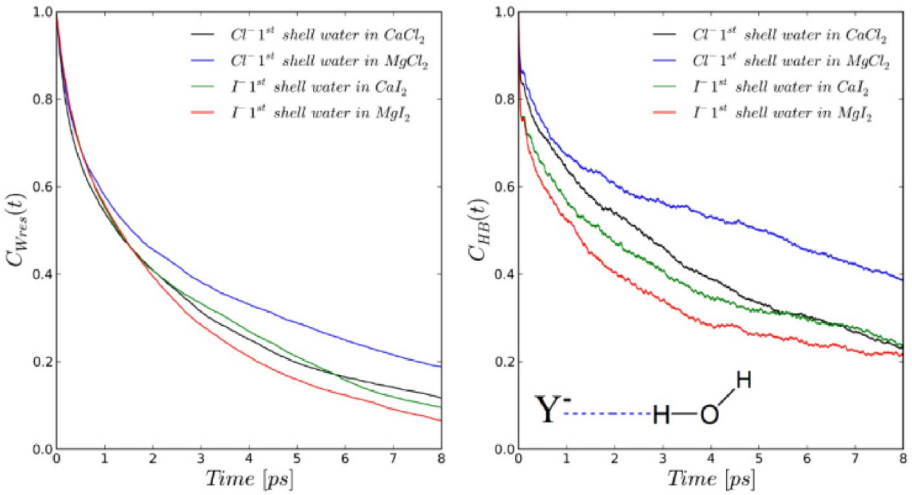

Figure 8. Autocorrelation functions characterizing the water residence time and water–anion H-bond ($Y^-\cdots H_2O$) lifetime in the first hydration shells of Cl^- and I^- ions.

porary escape of a water molecule from the first hydration shell shorter than 25 fs, and the boundaries of the hydration shells were defined by the positions of the first minima of the ion–oxygen RDFs. For the anion–water H-bond, the angular criterion is defined as $\measuredangle$Ion-O^1-$H^1 < \pi/6$. Figure 8 shows the residence-time correlation functions of water molecules around

the first hydration shell of the Cl^- and I^- ions $C_{Wres}(t)$ and anion–water H-bond (depicted in the inset) lifetimes $C_{HB}(t)$. The residence times are consistently shorter than the corresponding H-bond lifetimes for all anions. Clearly, some water molecules around anions do not form an H-bond and can diffuse away from the hydration shell. This dynamical result is consistent with the difference between the average number of H-bonds and coordination numbers (see Supporting Information). In addition, the length of the H-bond lifetime can be again attributed to the existence of solvent-shared ion pairs, which can make water molecules experience very low mobility in the first hydration shells. Note that for the divalent cations it is virtually impossible to determine water residence times from the ab initio molecular dynamics simulations, since the correlation times exceed our simulation time by far.

3. Conclusions

We have characterized the structure and dynamics of the H-bond networks of a series of divalent salt solutions ($MgCl_2$, $CaCl_2$, MgI_2 and CaI_2 at 2 M concentration) by means of first-principles MD simulations, complemented by measurements and corresponding quantum chemical calculations of the ^{1}H NMR chemical shifts. Our calculations provide atomistic insight into the kosmotropic and chaotropic mechanisms. We extend our analysis beyond the structural picture (i.e. the conventional Hofmeister effect) by including dynamical properties of water molecules around the first hydration shell of ions. Our results show that the impact of ions on water dynamics is ion-specific. It depends not only on ionic size and charge, but also strongly on the existence and stability of solvent-shared ion pairs. The dynamical behavior of the first hydration shell of water molecules around Mg^{2+} is significantly slower than that of Ca^{2+} and prevails beyond the first hydration shell. The effect is particularly visible in the presence of I^- ions (as opposed to Cl^- ions), due to the immobilization of water molecules in interstitial sites. Our work explains the conventional concept of the Hofmeister effect by incorporating the additional aspect of molecular dynamics within the H-bond network.

Acknowledgements

Computing infrastructure was provided by the HLRS supercomputers of the Research Centre Stuttgart. This work was supported by the SFB/TRR 102 (project A9).

Keywords: Hofmeister series · hydrogen bonds · ion pairs · molecular dynamics · NMR spectroscopy

[1] D. Paschek, R. Ludwig, *Angew. Chem. Int. Ed.* **2011**, *50*, 352; *Angew. Chem.* **2011**, *123*, 368.
[2] K. B. Rembert, J. Paterová, J. Heyda, C. Hilty, P. Jungwirth, P. S. Cremer, *J. Am. Chem. Soc.* **2012**, *134*, 10039.
[3] M. Shepherd, C. N. Hunter, *Biochem. J.* **2004**, *382*, 1009.
[4] J. P. Glusker, A. K. Katz, C. W. Bock, *Struct. Chem.* **2001**, *12*, 323 – 341.
[5] M. J. Fedor, J. R. Williamson, *Nat. Rev. Mol. Cell Biol.* **2005**, *6*, 399.
[6] M. Boero, M. Tateno, K. Terakura, A. Oshiyama, *J. Chem. Theory Comput.* **2005**, *1*, 925.
[7] M. Boero, K. Terakura, M. Tateno, *J. Am. Chem. Soc.* **2002**, *124*, 8949.
[8] M. Vogt, S. Lahiri, C. G. Hoogstraten, R. D. Britt, V. J. DeRose, *J. Am. Chem. Soc.* **2006**, *128*, 16764.
[9] L. Noodleman, T. Lovell, W.-G. Han, J. Li, F. Himo, *Chem. Rev.* **2004**, *104*, 459.
[10] S. J. Lippard, J. M. Berg, *Curr. Opin. Chem. Biol.* **2000**, *4*, 137.
[11] F. Bruni, S. Imberti, R. Mancinelli, M. A. Ricci, *J. Chem. Phys.* **2012**, *136*, 064520.
[12] G. Licheri, G. Piccaluga, G. Pinna, *J. Chem. Phys.* **1976**, *64*, 2437.
[13] F. Jalilehvand, D. Spängberg, P. Lindqvist-Reis, K. Hermansson, I. Persson, M. Sandström, *J. Am. Chem. Soc.* **2001**, *123*, 431.
[14] T. Megyes, I. Bakó, S. Bálint, T. Grósz, T. Radnai, *J. Mol. Liq.* **2006**, *129*, 63 – 74.
[15] M. M. Probst, T. Radnai, K. Heinzinger, P. Bopp, B. M. Rode, *J. Phys. Chem.* **1985**, *89*, 753.
[16] P. Smirnov, M. Yamagami, H. Wakita, T. Yamaguchi, *J. Mol. Liq.* **1997**, *73 – 74*, 305 – 316.
[17] T. Megyes, T. Grósz, T. Radnai, I. Bakó, G. Pálinkás, *J. Phys. Chem. A* **2004**, *108*, 7261.
[18] L. Bernasconi, E. Jan Baerends, M. Sprik, *J. Phys. Chem. B* **2006**, *110*, 11444.
[19] D. Jiao, C. King, A. Grossfield, T. A. Darden, P. Ren, *J. Phys. Chem. B* **2006**, *110*, 18553.
[20] J. M. Martínez, R. R. Pappalardo, E. Sánchez Marcos, *J. Am. Chem. Soc.* **1999**, *121*, 3175.
[21] K. Waizumi, H. Masuda, N. Fukushima, *Chem. Phys. Lett.* **1993**, *205*, 317 – 323.
[22] C. W. Bock, A. Kaufman, J. P. Glusker, *Inorg. Chem.* **1994**, *33*, 419.
[23] G. D. Markham, J. P. Glusker, C. W. Bock, *J. Phys. Chem. B* **2002**, *106*, 5118.
[24] G. D. Markham, J. P. Glusker, C. L. Bock, M. Trachtman, C. W. Bock, *J. Phys. Chem.* **1996**, *100*, 3488.
[25] A. Tongraar, B. M. Rode, *Chem. Phys. Lett.* **2001**, *346*, 485 – 491.
[26] A. Tongraar, B. M. Rode, *Chem. Phys. Lett.* **2005**, *409*, 304 – 309.
[27] C. Krekeler, L. Delle Site, *J. Phys. Condens. Matter* **2007**, *19*, 192101.
[28] F. C. Lightstone, E. Schwegler, R. Q. Hood, F. Gygi, G. Galli, *Chem. Phys. Lett.* **2001**, *343*, 549 – 555.
[29] F. Hallberg, I. Furó, P. Stilbs, *J. Am. Chem. Soc.* **2009**, *131*, 13900.
[30] K. J. Tielrooij, N. Garcia-Araez, M. Bonn, H. J. Bakker, *Science* **2010**, *328*, 1006.
[31] A. W. Omta, M. F. Kropman, S. Woutersen, H. J. Bakker, *Science* **2003**, *301*, 347.
[32] A. W. Omta, M. F. Kropman, S. Woutersen, H. J. Bakker, *J. Chem. Phys.* **2003**, *119*, 12457.
[33] P. Novotny, O. Sohnel, *J. Chem. Eng. Data* **1988**, *33*, 49.
[34] J. Schmidt, J. VandeVondele, I.-F. Kuo, D. Sebastiani, J. I. Siepmann, J. Hutter, C. J. Mundy, *J. Phys. Chem. B* **2009**, *113*, 11959.
[35] E. W. Washburn, *International Critical Tables of Numerical Data, Physics, Chemistry and Technology*, 1st ed., **2003**, pp. 1926 – 1930.
[36] G. Bussi, D. Donadio, M. Parrinello, *J. Chem. Phys.* **2007**, *126*, 014101.
[37] D. R. Banyai, T. Murakhtina, D. Sebastiani, *Magn. Reson. Chem.* **2010**, *48*, S56 – S60.
[38] J. Kolafa, *J. Comput. Chem.* **2004**, *25*, 335.
[39] T. D. Kühne, M. Krack, F. R. Mohamed, M. Parrinello, *Phys. Rev. Lett.* **2007**, *98*, 066401.
[40] G. Lippert, J. Hutter, M. Parrinello, *Mol. Phys.* **1997**, *92*, 477.
[41] J. VandeVondele, M. Krack, F. Mohamed, M. Parrinello, Th. Chassaing, J. Hutter, *Comput. Phys. Commun.* **2005**, *167*, 103.
[42] J. Hutter, M. Iannuzzi, F. Schiffmann, J. Van de Vondele, *WIREs Comput. Mol. Sci.* **2014**, *4*, 15.
[43] S. Grimme, *J. Comput. Chem.* **2006**, *27*, 1787.
[44] A. D. Becke, *Phys. Rev. A* **1988**, *38*, 3098.
[45] C. Lee, W. Yang, R. G. Parr, *Phys. Rev. B* **1988**, *37*, 785.
[46] J. VandeVondele, J. Hutter, *J. Chem. Phys.* **2007**, *127*, 114105.
[47] S. Goedecker, M. Teter, J. Hutter, *Phys. Rev. B* **1996**, *54*, 1703.
[48] M. Schindler, W. Kutzelnigg, *J. Chem. Phys.* **1982**, *76*, 1919.
[49] C. Hartwigsen, S. Goedecker, J. Hutter, *Phys. Rev. B* **1998**, *58*, 3641.
[50] G. Lippert, J. Hutter, M. Parrinello, *Theor. Chem. Acc.* **1999**, *103*, 124.
[51] C. W. Bock, G. D. Markham, A. K. Katz, J. P. Glusker, *Theor. Chem. Acc.* **2006**, *115*, 100 – 112.

[52] T. Todorova, P. H. Hünenberger, J. Hutter, *J. Chem. Theory Comput.* **2008**, *4*, 779.
[53] H. Elgabarty, R. Z. Khaliullin, T. D. Kühne, *Nat. Commun.* **2015**, *6*, 8318.
[54] A. Luzar, D. Chandler, *Nature* **1996**, *379*, 55 – 57.
[55] A. Luzar, D. Chandler, *Phys. Rev. Lett.* **1996**, *76*, 928.
[56] T. D. Kühne, M. Krack, M. Parrinello, *J. Chem. Theory Comput.* **2009**, *5*, 235.
[57] C. Allolio, N. Salas-Illanes, Y. S. Desmukh, M. R. Hansen, D. Sebastiani, *J. Phys. Chem. B.* **2013**, *117*, 9939.
[58] D. Laage, G. Stirnemann, J. T. Hynes, *J. Phys. Chem. B* **2009**, *113*, 2428.
[59] A. S. Thomas, A. H. Elcock, *J. Am. Chem. Soc.* **2007**, *129*, 14887.
[60] G. Bekçioğlu, C. Allolio, D. Sebastiani, *J. Phys. Chem. B* **2015**, *119*, 4053.
[61] G. Stirnemann, E. Wernersson, P. Jungwirth, D. Laage, *J. Am. Chem. Soc.* **2013**, *135*, 11824.

Manuscript received: December 12, 2015
Accepted Article published: February 11, 2016
Final Article published: February 11, 2016

C Academic curriculum vitae

For reasons of data protection, the curriculum vitae is not included in the online version.

For reasons of data protection, the curriculum vitae is not included in the online version.

D Acknowledgements

I would like to express my sincere gratitude to my advisor Prof. Daniel Sebastiani for his support and guidance with patience, and motivation through the course of the research. I am especially indebted to his friendship and his trust throughout this work. I would like to thank our collaborators Dr. E. Nibbering and Dr. M. Ekimova for their interesting experiments and discussions.

I would like to express my appreciation to all members of Sebastiani research group for their support over the years. I would like to especially acknowledge Christoph, Arne, Tobias, Hossam for their numerous discussions and criticism on related topics. Special thanks go to Felix for his valuable discussions, and friendship through the difficult times. Felix, I think we both have a lot of impact on each other both scientifically, and socially.

I am also thankful to Christel and Richard Neff for their support and care, when I decided to start a new life in Germany.

Most importantly, none of this would have been possible without the love, and patience of my family. To my mother, Arife Hanım, who is the main source of inspiration for my continued education, thank you for providing me with all of your love, joy of life, and support, without which I never would have achieved so much. My sisters Ayşe and Zehra, and my brother Ömer, I thank you all for being my family.

A very special acknowledgement goes to my husband Andreas for cheering me up and standing by me through the good times and bad. After all those interesting and funny experiences in Germany and especially in Turkey, you made me to consider different dimensions of life. Your perspective and understanding in life is so much to me. Without you, I never would have finished successfully.